Charles University

Faculty of Medicine in Hradci Králové

DISSERTATION THESIS

Michal Kuchař **2022**

Charles University
Faculty of Medicine in Hradec Králové

Doctoral Study Programme
Anatomy, Histology and Embryology

Anthropometric-biomechanical description of human pelvis based on the principal stiffness and deformation modes.

Antropometrická-biomechanická charakteristika lidské pánve ve smyslu hlavních tuhostí a deformačních módů.

Mgr. Michal Kuchař

Supervisor: Assoc. Prof. Dáša Slížová MD, Ph.D.
Consultant supervisor: Assoc. Prof. Ing. Petr Henyš, Ph.D.

Hradec Králové, 2022

Author‘s Declaration

Declaration:

I declare hereby that this disseertation thesis is my own original work and that I indicated by references all used information sources. I also agree with depositing my dissertation in the Medical Library of the Charles University, Faculty of Medicine in Hradec Králové and with making use of it for study and educational purpose provided that anyone who will use it for his/her publication or lectures is obliged to refer to or cite my work properly.

I give my consent to availibility of my dissertation’s electronic version in the information system of the Charles University.

Hradec Králové, 2022

Dissertation Acknowledgements

I would like to thank the following people, without whom I would not have been able to complete this thesis and without whom I would not have made it through my PhD studies.

First of all, I would like to express my sincere gratitude to my supervisor, Assoc. Prof. Dáša Slížová MD, Ph.D., for her continuous support, encouragement, and patience throughout this study. To the Assoc. Prof. Ing. Petr Henyš, Ph.D., whose insight and knowledge into the subject matter helped me immensely to understand the technical part of the work. And special thanks to all my colleagues from the anatomical department for all the unconditional support, giving me time to write.

Finally, I would like to thank my family for supporting me during the compilation of this dissertation. You are great.

Table of contents

List of abbreviations

3D	Three dimensional
BMD	Bone Mineral Density
$\overline{BMD}$	Bone Mineral Density (average)
CT	Computer tomography
DE	Density-Elasticity (relationship)
DEXA	Dual Energy X-Ray Absorptiometry
DICOM	Digital Imaging and Communications in Medicine
DSP	Diagnose Sexuelle Probabiliste
E_{cort}	Young's modulus of cortical bone
E_{trab}	Young's modulus of trabecular bone
FE/M/A	Finite Element /Method /Analysis
FEMP-I	Finite Element model (fixed boundary conditions)
FEMP-II	Finite Element model (free boundary conditions)
HU	Hounsfield Unit
MITK-GEM	Medical Imaging Interaction Toolkit
STL	Stereolitography format
TEM	Technical Error of Measurement
TUL	Technical University in Liberec
QCT	Quantitative Computer Tomography
QDMC	Quadratic Discriminant Classification Method
ρ_{app}	Apparent density (bony tissue structural volume per unit)
ρ_{ash}	Ash density (ash mass divided by bulk sample volume)

Summary

Skeleton is a basic supporting system of the human body and a passive substrate for any possible movement, while the shape and mechanical properties of a single bone are given both by the embryological origin and its function. The bone can transfer mechanical load with an optimal amount of energy and this power flow can be documented, either by mechanical testing or by computational modelling. The author decided for the latter and tried to define the main stiffnesses as one of the most important internal modalities to determine overall bone quality.

Stiffness is a widely used biomechanical measure reflecting geometric, topologic and material properties of a given bone. It is defined as a resistance of a bone against deformation in response to an applied force. This thesis aims to study and to describe a characteristic bone stiffness of a CT based virtual models using the spectral decomposition of a stiffness matrix. The characteristic stiffness as a brand-new descriptor of bone tissue will be further correlated with the bone density spatial distribution and matched against a set of chosen anthropometric measurements to test its sex-specificity. Additionally, an automatic system capable of recognizing and generating anthropometric landmarks on a bone will be developed.

The localization of the smallest stiffnesses and their directions has a significant practical output. As bone quality directly influences patients' lives, novel methods for predicting bone mechanics are of high interest in various medical fields. With the proper modelling, one can model the fracture risk (side-falls, car accidents), skeletal adaptation in response to specific loading (implants) or mechanical changes based on different diseases (osteoporosis). Ideally, non-invasively and based on actual patients' examinations.

In this thesis, the author focused on finding these stiffnesses to better understand the complex anatomy and physiology of the human pelvic bone. As the bones are different in size and shape, connected to muscles and neighbouring body parts, all these aspects affect bone stiffness's spatial distribution. Here, the combined anatomical and bio-mechanical input is essential.

Souhrn

Kostra je základní podpůrný systém lidského těla a zároveň pasivní složka pro jakýkoliv možný pohyb. Mechanické vlastnosti i tvar kosti jsou dány jak jejím embryologickým původem, tak její funkcí. Jednotlivé kosti jsou schopny přenášet mechanické zatížení s optimálním množstvím energie a tento tok energie lze dokumentovat pomocí mechanických testů či počítačovým modelováním. Rozhodl jsem se pro druhou z možností a formuloval jsem tuhosti jako jednu z nejdůležitějších vnitřních modalit k určení celkové kvality kostí.

Tuhost jako veličina je široce používaným biomechanickým měřítkem odrážejícím geometrické, topologické a materiálové vlastnosti dané kosti. Je definována jako odpor kosti proti deformaci v reakci na aplikovanou sílu. Cílem disertační práce je studovat a popsat tzv. charakteristickou tuhost kostí pomocí virtuálních modelů založených na snímcích počítačové tomografie a spektrálního rozkladu matice tuhosti. Charakteristická tuhost jako zcela nový deskriptor kostní tkáně bude dále porovnána s lokálním rozložením kostní hustoty i se sadou vybraných antropometrických měření za účelem testování její pohlavní specificity. Pro studium pohlavní rozdílnosti je zároveň nutné vyvinout automatický systém schopný rozpoznat a generovat antropometrické orientační body na kosti.

Lokalizace nejmenších tuhostí a jejich směrů má významný praktický výstup. Vzhledem k tomu, že kvalita kostí přímo ovlivňuje kvalitu života pacienta, jsou nové metody predikce kostní mechaniky velmi zajímavé v různých biomedicínských oborech. Díky této metodice může být v budoucnu možné modelovat riziko zlomenin (boční pády, autonehody), adaptaci skeletu v reakci na specifické zatížení (implantáty) nebo mechanické změny kosti při různých onemocněních (osteoporóza). Vše neinvazivně a na základě vyšetření reálných pacientů.

V této práci se zaměřuji na nalezení těchto tuhostí a prostřednictvím těchto informací se snažím lépe porozumět složité anatomii a fyziologii lidských pánevních kostí. Vzhledem k tvarové složitosti, i pro jejich úzký funkční vztah k okolním strukturám, je nezbytný kombinovaný anatomický a biomechanický přístup.

Introduction

There is a high interest in finding the origin of skeletal fragility, leading to many collaborations between clinicians and anatomists, physicists and engineers. This branching tree of studies in various disciplines clearly shows that there is no simple way to describe bone properties. With ever-developing imaging techniques and increasing knowledge about the drugs mechanism, bone turnover, and macro- and microstructure, the term "bone quality" appeared in the literature [1]. Bone quality is an umbrella expression for various bone characteristics (including [2] or excluding [3-5] the structure mass), which are in total important in determining bone behaviour and potential fracture risk. The complexity of these characteristics led to a proliferation of studies, from nano-structural at the level of collagen structure and mineral crystals to macro-structural describing the whole bone morphology. The methods of assessing bone quality components are similarly numerous, from bone resorption biomarkers, chemical analyses, and scanning electron microscopy to X-ray-based imaging modalities (Fig. 1).

Although the proportional distribution of previously mentioned characteristics on bone structural behaviour is still discussed, it is possible to quantify their joint influence on whole-bone level through various types of mechanical testing. Each experimental set-up depends on whether the structural strength, toughness or stiffness is to be measured. Being by definition related to fractures, bone strength is a preferable choice in most studies. Recently, one can observe an increased number of stiffness oriented studies as a non-destructive and in-vivo applicable method. Moreover, structural stiffness is probably the main adaptive feature of bone, allowing proper response to incoming loads by optimising bone shape and material. As a bone quality directly influences patients' lives, novel methods for predicting bone mechanics are of much interest to clinicians and researchers. We can observe a shift from the traditional mechanical testing to the digital bone, or ‘in silico’ models, where elastic properties are derived from computer tomography (CT) scans. However, the necessary cost comes in general simplifying material behaviour to create a practical computational model. The result strongly depends on the quality of input data, which is limited to the macro-structural level at clinical CT. Current machines still don’t capture the internal bone architectonics properly and often require external calibration to derive bone mineral density (BMD) from attenuation coefficients.

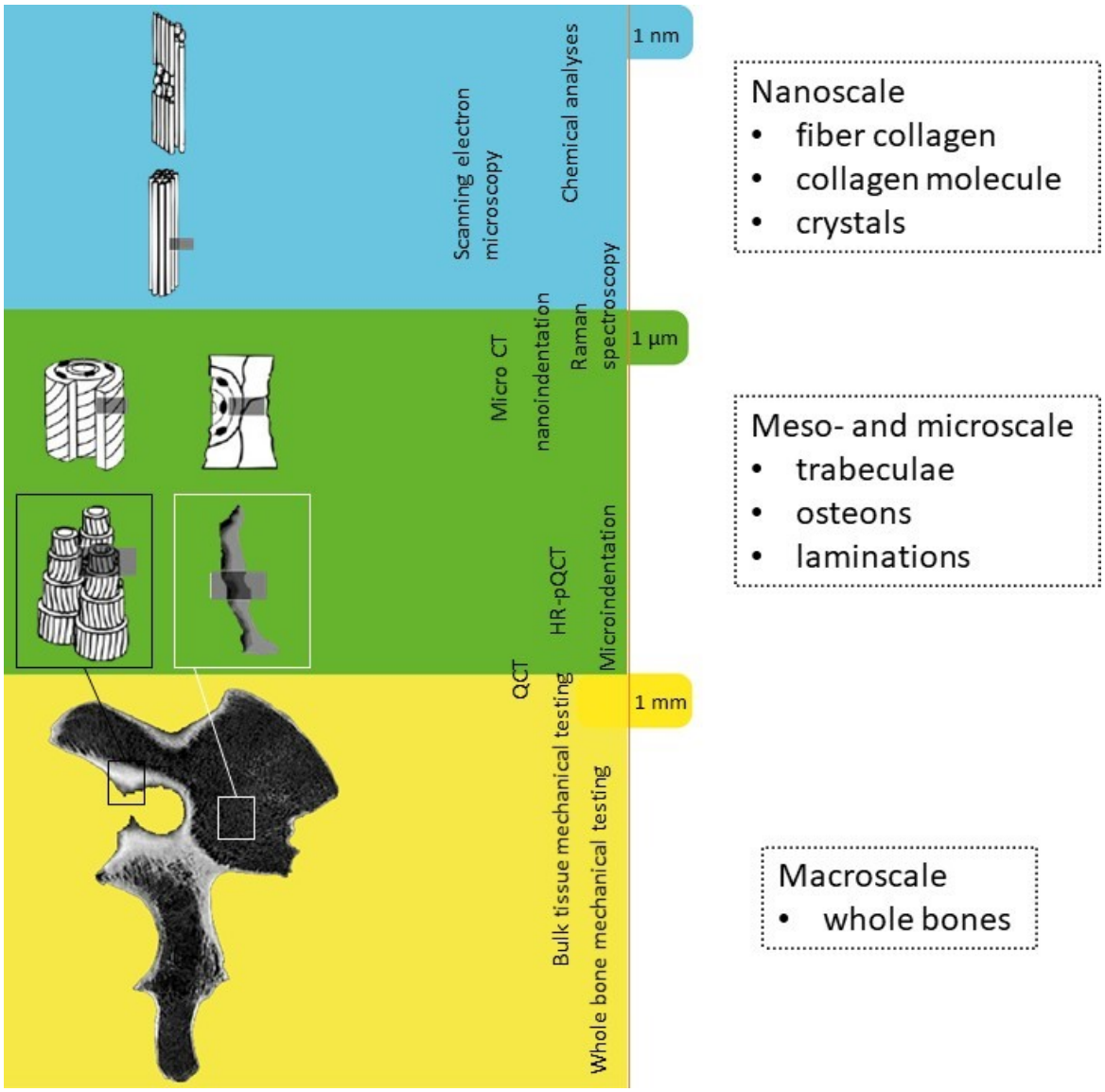

Fig. 1: Bone structural properties at a various scale, with appliable methods.

This study tries to predict the bone behaviour according to its characteristic stiffness. In this process, we had to run a number of intermediate steps. Firstly, a sufficient number of clinical CTs had to be collected, checked for any possible trauma and segmented. Simultaneously, a literature review had to be performed to find a suitable density-elasticity relationship (DE-relationship) of bone tissue to fit our biomechanical models. Secondly, the bone morphology and density distribution had to be quantified to develop a model of virtual stiffness measurement. The final part was to describe our model's population specificity (spatial, temporal and sex distribution). The organization of the work is proposed in Fig. 2.

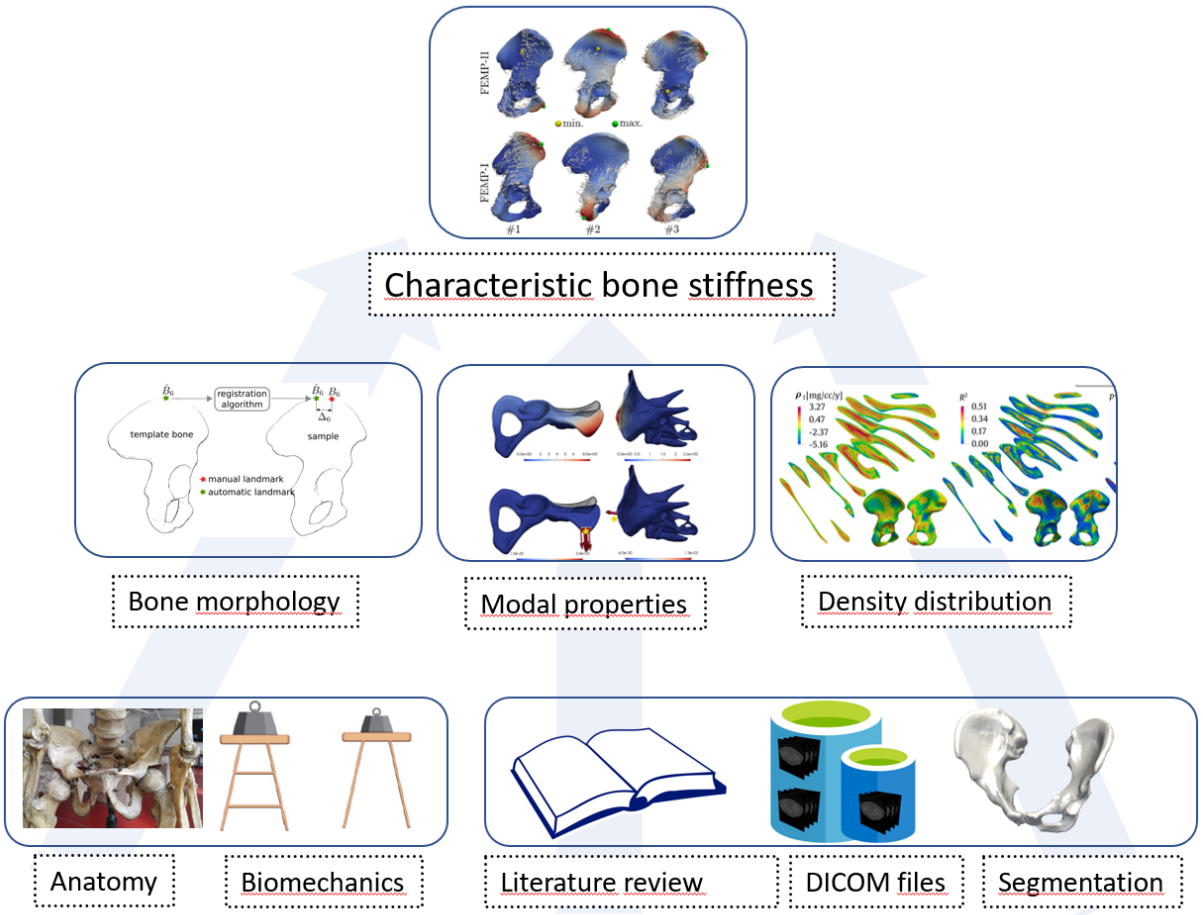

Fig. 2: Study outline. The first step (base of the pyramid) should be an understanding of the bone anatomy and basic biomechanics; to gather and process the appropriate number of patients data; to find a suitable relationship between bone density and elasticity. Second line represents the population-wise definition of bone morphology and density. Further on, the idea of the spectral decomposition of a stiffness matrix is introduced. Finally, the characteristic bone stiffness is derived according to all previous sub-steps, and the method implications are discussed.

Aims and contributions

Study aims

The project aims to study and to describe a characteristic bone stiffness of a CT based virtual models using the spectral decomposition of a stiffness matrix, with the following hypotheses:

We can locate the sites of smallest/highest stiffnesses on human pelvic bone.

There is a correlation between these stiffnesses and shape, sex and age.

We can predict the distribution of stiffnesses in the population.

And the following implications:

The author will improve his expertise in topics of imaging methods and their processing, creation of finite-element models and their interpretation.

Established big database of pelvic bone models can serve both for this thesis purposes and for consequent studies.

A newly formed shape analysis algorithm will considerably speed up the results acquisition, even allowing later correction of input data. The researcher's experience and practice are here not of importance.

The population-specific bone density and stiffness will improve current biomechanical models. Its outcomes could be further applied in many clinical fields, such as orthopedy, traumatology or endocrinology (osteoporosis).

The characteristic stiffness is potentially a strong inter-individual descriptor and could be used in forensic or anthropological studies.

The bone quality directly influences the patient’s health. Hence, novel methods for predicting bone mechanics in-vivo, ideally non-invasively, are of high interest in contemporary trauma, orthopaedics and endocrinology research. The stiffness is a key component for analysing the skeletal or intraskeletal adaptation and changes in response to a given loading. It may also help

to better understand the dynamics of the human pelvis during side falls [6] or alike injury; even the osteoporosis was investigated by analysing the stiffness [7, 8]. The age and sex dependence of stiffness were also shown [9-11]. Although the importance of structural stiffness is known [10, 12, 13], its precise assessment is complicated in in-vitro conditions. It is restricted in many investigated directions, doesn't respect the entire bone geometry and physiology [98-100], and even varies across the studies [14]. Nowadays, one can observe an increased number of in-silico (computer-driven) studies that complement the traditional methods and are capable of clinical use [15, 16]. These digital models are often used in the biomechanics community to analyse bone mechanics in a virtual fashion.

Nevertheless, such computer models should be driven by the clinical patient data according to the so-called digital twin paradigm. Although the digital twin paradigm provides a step toward real clinical applications, the bone mechanics must be precisely known before fully using digital models. As promising as this approach may look, there are still significant limitations that must be solved:

- to standardize a site and a direction of stiffness measurement
- to compare anatomically or structurally different bones
- find a method to be applicable to the most common virtual data (i.e. clinical CT) with common resolution (1x1x1 mm).

The common bio-mechanical methods applied in bone composition modelling use the principles of topological optimization to estimate optimal bone geometry according to the various loads. Here, the idea is the opposite, i.e., to map the bone stiffness on a base of known bone geometry (Fig. 3). From a set of computer tomography scans, the author will create a complex of anatomical elements through either manual or automatic segmentation. Further, use them for computing the characteristic stiffness given by its geometry and internal structure. Once transformed into mathematical models by the finite element method, newly emerged models will define the main stiffnesses and directions. The characteristic stiffness as a brand-new descriptor of bone tissue will be matched against a set of chosen anthropometric measurements to test its sex-specificity. Additionally, an automatic system capable of recognizing and generating anthropometric landmarks on a bone is to be developed as a side result.

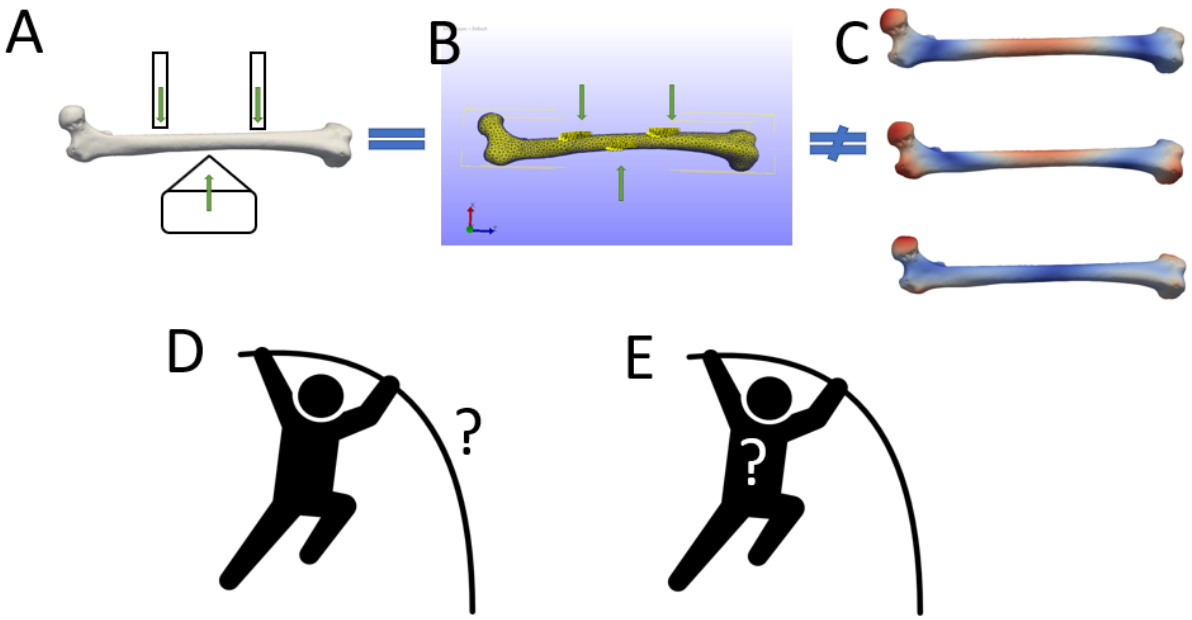

Fig. 3: An explanation of the method novelty. The standard biomechanical 3-point bending test of the long bone (A) can be substituted by FEA simulated virtual measurement, in respect with the original boundary conditions, load magnitude and its direction (B). In our study, characteristic bone stiffness is found independently from the incoming loads, just from known structure morphology and internal structure - even with no boundary conditions defined (C). Both methods describe the structural behaviour with respect to external forces. Traditional approach (D): incoming load is applied to the pole, resulting in its bending. Our approach (E): what type of load should be applied to bend the vault to this typical shape?

Contributions

The dissertation thesis is a part of the continuous collaboration between the Faculty of Medicine in Hradec Králové and the Technical University in Liberec (TUL). We found the synthesis of mathematical and anatomical aspects productive and mutually enriching. The author is the creator of a protocol for collecting CT data from a local hospital database. He segmented pelvic bones from this data collection, performed anatomical analysis, and extracted values of selected tissues for internal calibration of HU units to BMD density. In the next step, the author proposed the idea of using a registration algorithm to automatically analyse the data in the CT database. He demonstrated the advantages of the registration algorithm in [17]. This algorithm became crucial in a further analysis, where the author showed for the first time how bone density

changes regionally as a function of age and sex and outlined several original hypotheses that may explain the complex evolution of density in different regions (see [18]). After analysing BMD density, which is crucial for the determination of bone stiffness, the author came up with the original idea of the existence of a so-called characteristic stiffness that would include both material and structural properties of the bone. In collaboration with asoc. prof. Henyš, who provided the technical calculation of the spectral decomposition of the bone stiffness matrix, they found that the smallest bone stiffness could be found without a costly experiment [19]. In the next step, the author analysed the sensitivity of this stiffness to sex and age and demonstrated for the first time that pelvic bone stiffness is strongly sensitive to age and sex and has excellent predictive capabilities for anthropometric analyses [20]. He concluded the paper with an analysis of the properties of this stiffness, specifically first and second modal stiffness and its associated deformation shapes on a selected femoral bone. In this chapter, he showed that these characteristic deformation modes have the same shape as the deformation under normal movement physiology, thus confirming for the first time that this characteristic stiffness has a deeper meaning and reflects the mechanical design of the bone.

Anatomy

Bone as an organ

The human body comprises more than 200 bones representing the bony skeleton. Regarding its position and function, it is possible to describe the axial skeleton consisting of the bones of the head and trunk and the appendicular skeleton supporting the limbs. Basically, three major forces affect the human body – gravity, the tension of contracted muscles and various external forces causing major or minor deformations. The skeletal system can neutralize most of these forces thanks to its multiple functions. Bones and their connections form a strong scaffold, serve as an anchor point for the muscles (active apparatus) and, through the complex system of levers, allow the change of position of a specific body part, as well as intended locomotion. The absolute power and extent of a movement further depend on the muscle's length and the number and course of its muscle fibres. Many internal organs have their bony covering. The brain is protected by the flat skull bones, spinal cord by the bodies and arches of vertebrae, thoracic chest and pelvis are basically bony capsules for viscera.

Due to their different shapes, we traditionally classify the bones as long, short, and flat bones. The long bones grow mainly in one direction, the flat in two main directions, the short in three directions. Irregular bones include those bones which can present the features of either long, flat or short ones. Pneumatized bones contain a cavity or small cavities filled with air. All types of bones express different mechanical properties given by their shape.

The periosteum covers the surface of the bones. It serves as a dense fibrous capsule mechanically protecting the bone tissue. It covers all the parts of the bone which are not joint surfaces and is firmly connected at sites of tendons or ligament insertions and the margins of the skull flat bones. The periosteum contains many sensory nerve fibres and brings blood and lymph vessels to the bone. Given the osteogenetic function, the periosteum is essential for bone growth or remodelation of a bone after fractures [21].

Postnatally the hematopoietic centre in the liver and spleen lose its importance, and the blood cells are created in the red bone marrow. The red bone marrow filling almost all the cancellous bones will gradually cease and remain functional in long bones epiphyses, in short bones, vertebrae, ribs, sternum, pelvic bones and inside diploe of flat cranial bones. In senile age, the red marrow is present mainly in the vertebral bodies and inside the pelvic bones [22]. While ageing, the reticular tissue of red marrow is permeated by adipocytes changing it to the yellow

bone marrow. The hematopoietic function is therefore lost. However, a new fatty tissue further serves as an important energy source and, potentially, a load distributor [23].

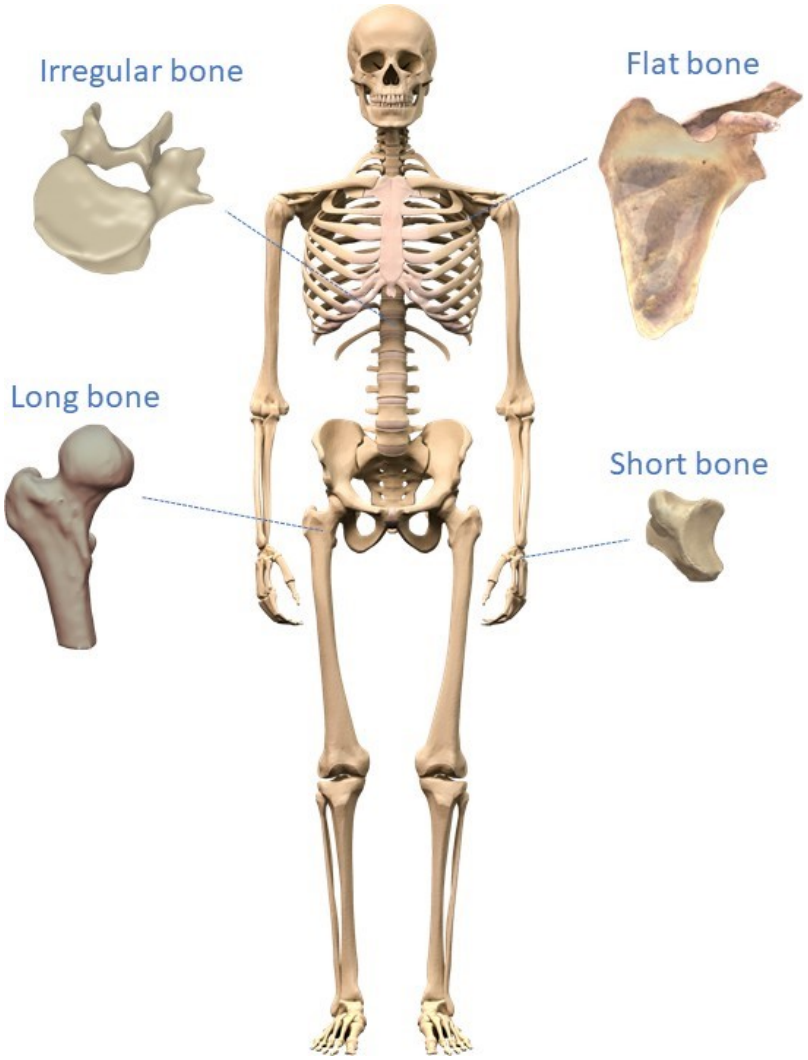

Fig. 4: An example of different bone shapes.

Bone tissue

Bone as a rigid organ is formed by a type of dense connective tissue, bone tissue. Its intercellular space contains the organic part, mineral part and water. The organic phase (approximately 90% type I collagen, 10% noncollagenous proteins and lipids) provides resilience and ductility. The mineral part, the salts, confer hardness and strength. It is composed mainly of highly substituted, poorly carbonated hydroxyapatite. The carbonate content follows the maturation of the bone tissue and growth laterally to be oriented parallel to the collagen fibrils. Due to intensive

metabolic activity, the tissue level of salts can change. The bones serve as mineral storage (primarily for calcium), and the process of bone creation and reabsorption regulates mineral balance in the systemic circulation [24].

Bone architectonics

Osseous tissue is organized at the microstructural level and exhibit a distinct stratification produced by layers of collagenous fibrils. This lamellar bone comprises cortical bone, the outer layer forming the outer circumferential lamellae, the compact bone formed by osteons and loosely organized trabecular bone [25]. In literature, one can find both terms cortical and compact bone for any non-trabecular lamellar bony tissue. Macroscopically, cortical bone forms a solid osseous shell around the bone. This type of bone tissue is stiffer and can resist higher ultimate stress. Contrary to trabecular bone, it is brittle and usually fails while deformed beyond 2 % [26]. Trabecular bone shows a characteristics network of lamellar bone plates and rods. It is weaker than cortical bone but more flexible, and it offers a wide variability in strength and stiffness. Trabecular bone expresses less homogeneity, a lesser degree of parallel orientation and its mechanical properties are strongly influenced by the surrounding bone marrow. Cortex-to-trabecular bone volume ratio is different in short, long and flat bones to withstand different compression forces [27]. The overall localization of lamellae and trabeculae should respect Wolff's law which states that every change in the function of a bone is followed by certain definite changes in its internal architecture and its external conformation [28]. This continuously remodelling system is called bone architectonics (Fig. 5) and is responsible for the biomechanical qualities of the bone.

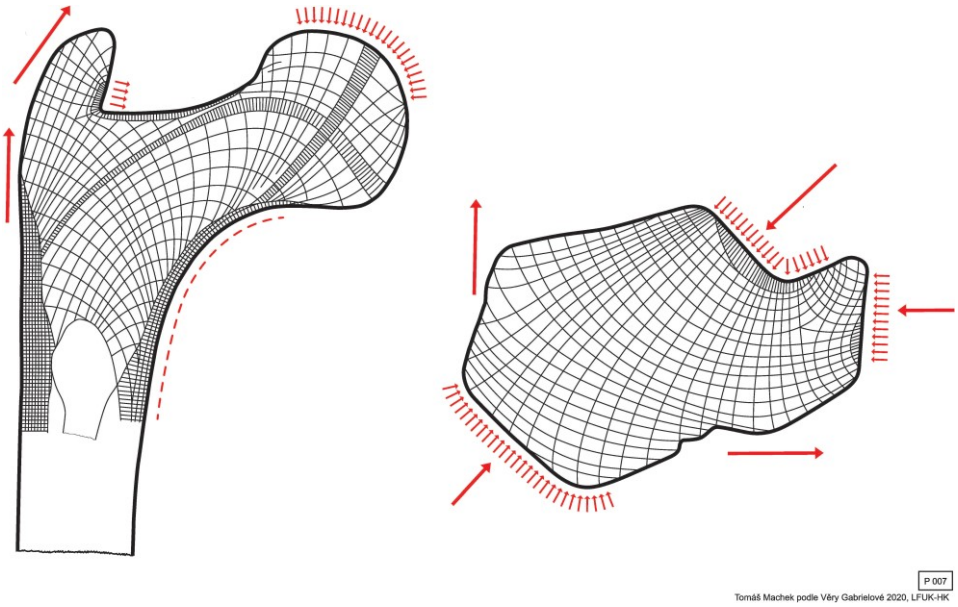

Fig. 5: Bone architecture. The inner architectonics of proximal femur and calcaneus. Picture collection of the Department of Anatomy, Faculty of Medicine in Hradec Králové.

Bone geometry

As the bone develops, a recognisable though a rough version of the specific bone is formed from the mesenchymal cells, further modelled by external forces to adapt to routine mechanical loads functionally [29]. The terminal volume, shape and internal structure will affect the bio-mechanical properties immensely.

In recent history, many authors focused on the impact of either external or internal geometry on bone stiffness and strength. Most common are studies performed on the weight-bearing bones, typically tibiae, based on their cross-sectional geometry. These tubular structures follow relatively simple biomechanical rules, and stiffness is expected to correlate strongly with strength because both measures depend on similar morphological and material properties. Furthermore, the long bone diaphysis is considered as a good model for understanding the basic principles of how the skeletal system coordinately adjusts multiple traits to establish mechanical homeostasis [30]. For bones to be functional, they must maximize their stiffness while also minimizing their mass [31], and it is well known that an increase in bone diameter and thickness of the bony wall will increase overall stiffness and strength [32]. The robustness of the bone, which is the total cross-sectional area relative to length, is a part of this adaptive system to keep the bone strong within some reasonable weight limits. It was found that bone volume, cortical thickness and cross-sectional area predicted almost 80 per cent of bone stiffness, strength and

yield force on murine femora [33]. A broad range in bone robustness is present within and between populations, supposedly established early postnatally in both males and females [34]. Two individuals of similar body sizes can present two different phenotypes of an appendicular skeleton (Fig. 6).

The differences in cross-sectional diameter and cortical thickness correspond to a specific phenotype and can be further adjusted by a continued periosteal apposition and bone resorption. Compared to the robust bones, the slender bones with smaller cross-sectional diameters have proportionally thicker cortices and greater mineralisation with less intracortical porosity. There appears to be a compensatory mechanism in order to maintain normal bone function [34] by construction of a reasonably stiff and strong bone in terms of everyday loads. Under normal conditions, both slender and robust bones perform well. However, the proportionally thick, highly mineralized cortices of the slender bones make them more brittle, while proportionally thin cortices of robust bones possibly make them less tolerant of prolonged endosteal and intracortical remodelling [35]. Given the limited area of the bone surface, there should be a physiological limit within which the bone can be remodelled to get stronger. Jepsen [36] found that the bone cells could not adjust traits like cortical area and tissue modulus to the degree needed to fully compensate for the nonlinear relationship between bone width and whole-bone bending stiffness. His study explains this phenomenon by intrinsic cellular constraints (limited range in tissue modulus) that restrict the degree of compensation.

On the other hand, we cannot oversee the physiological advantage of this constraint as it protects against increased tissue brittleness. To my knowledge, there is no study demonstrating the role of robustness on flat bones. We can, however, anticipate the high importance of individual geometry even on this type of bones.

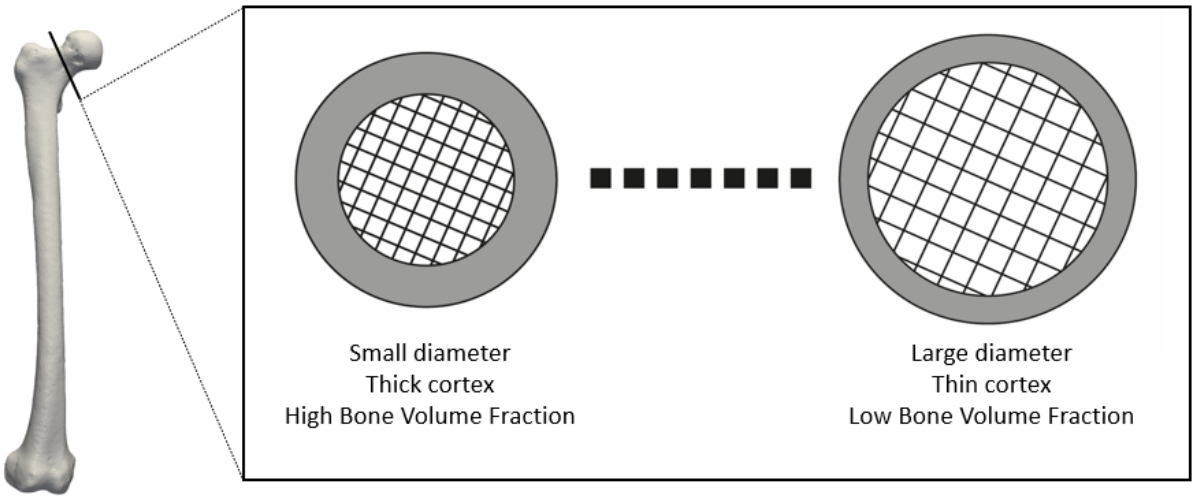

Fig. 6: Bone robusticity. Smaller bones compensate for the lack in size with increased cortical thickness and volume fraction to reach similar functional properties.

Pelvic bone

The human pelvic bone is a paired structure, dorsally articulating with the sacral bone and ventrally connected to its counterpart through the pubic symphysis, forming a cylindrical shaped structure called the pelvis. It arises from the three bony origins - iliac bone, ischial bone and pubic bone.

Iliac bone forms the upper part of the pelvic bone. The body of ilium extends cranially into the wing of ilium with a typical rough margin, iliac crest. Over the inner surface crosses the arcuate line as a boundary between greater and lesser pelvis, the external surface presents a large area for gluteal muscles origin. Two bony projections (iliac spines) are pointing forward, and two projections are pointing backwards. Ischium forms the inferoposterior part of the pelvic bone. It partially forms the obturator foramen as it borders the space by its body and ramus. Inferiorly there is a large bony prominence, ischial tuberosity separated by the lesser sciatic notch from the ischial spine.

The pubic bone is involved in the anterior closure of the obturator foramen, where the superior and inferior ramus merges into the body of pubis. The medial portion of the body presents the symphysial surface to which the cartilaginous pubic symphysis is attached. All the parts meet inside acetabulum, the cavity of the hip joint, where the head of femur is inserted.

The arterial supply comes from the branching of the common iliac artery. The external iliac artery follows the pelvic brim. Some of its branches (deep circumflex iliac, pubic branch of the inferior epigastric artery) nourish part of the iliac wing, most of iliac crest, and pubic rami. The branches of the internal iliac artery (iliolumbar, lateral sacral, superior and inferior gluteal, obturator) complete the nutritional requirements of the pelvic bone. The venous system is similar to the arterial and the blood drains to the tributaries of the common iliac vein. The nerves are of small diameter and arise from the lumbosacral plexus [25].

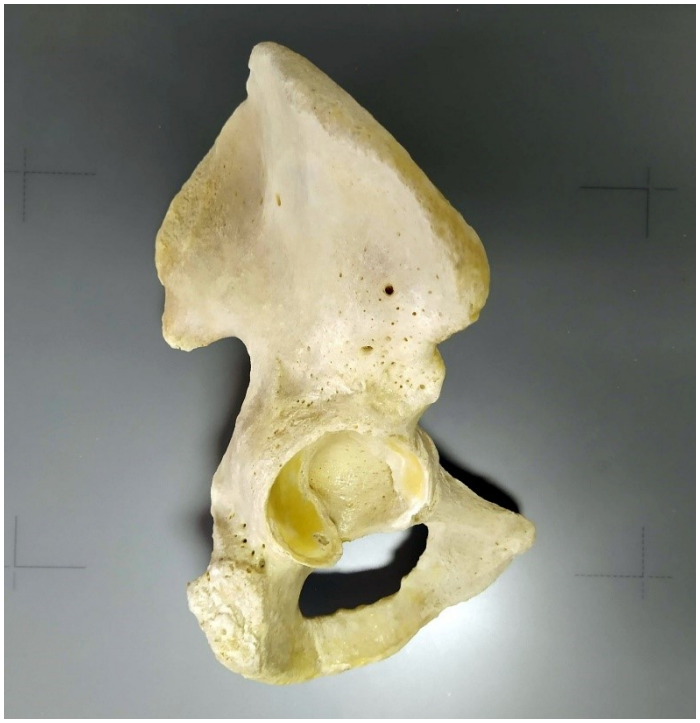

Fig. 7: The right pelvic bone. Anatomical collection of Department of Anatomy, Faculty of Medicine in Hradec Králové.

The later pubic bone starts to develop in cartilage inside the basis of embryologic limb buds in the 6th week of intrauterine development (IU). From the 9th week IU, the first bony tissue appears in the ilium, followed by the ossification centrum in the body of ischium (4th month IU) and by ossification centrum in pubis near the pubis acetabulum (4th – 5th month IU). Postnatally the bone is still not fully ossified and synostosis terminates at the bone periphery between the ages of 15 and 18 years. Strong cartilage in the region of acetabulum (cartilago ypsiloformis), separating ilium, ischium and pubis, ossifies between the ages of 15 and 16 years [37] (Fig. 8).

By the shape, the pelvic bone is a typical flat bone where two diameters are significantly larger than the third one. The trabecular bone is of low density, compact bone is thin on most sites, and because of its construction, the bulk of the load is carried mainly through the cortical bone [38].

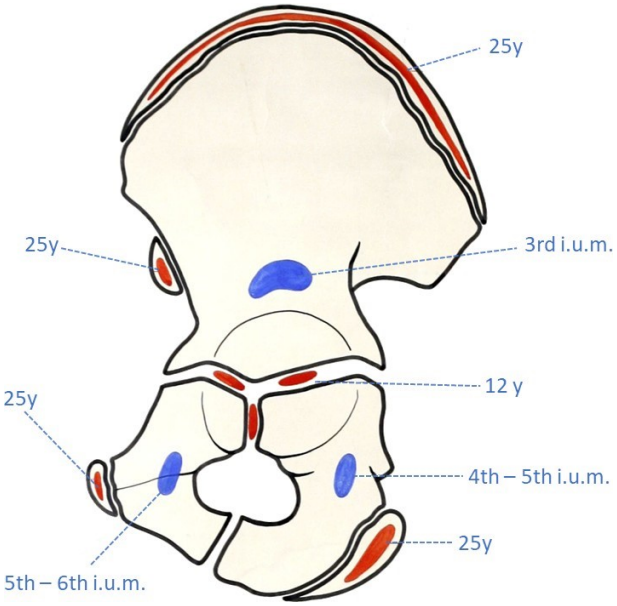

Fig. 8: Ossification of pelvic bone. Picture collection of Department of Anatomy, Faculty of Medicine in Hradec Králové.

Weight distribution and stability of the pelvic ring

The importance of pelvic bones is to hold the weight of the upper half of the body and transmit this pressure to the lower limbs. Whether the weight of the lower limbs is considered approximately 15 per cent of the total weight, the remaining 85 per cent goes through the pelvis. The forces as high as 5,5 times body weight are transferred here during activities such as running and stair climbing [39].

Simultaneously it serves as a point of origin and insertion of about 30 muscles from the different muscle groups, which affect the surface by their tension. The involved muscles are presented in Fig. 11. Moreover, there is a vital role of ligaments, holding the different structures of the pelvic ring together to counter loads. The strongest is the posterior sacroiliac, sacrospinous, sacrotuberous, iliolumbar and pubic ligaments. More advanced models are available to involve the muscle and ligamentous structures, as presented by [40, 41].

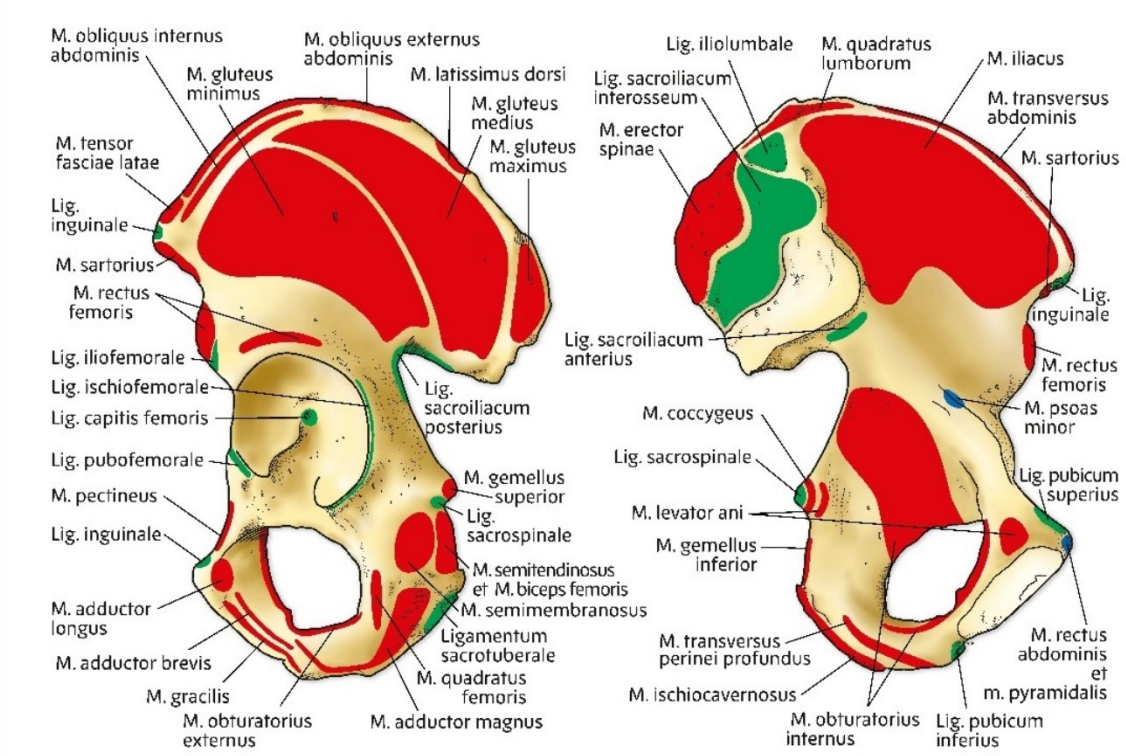

Fig. 11: Pelvic bone. Areas of muscle/ligament origins (red) and insertions (green). Picture collection of Department of Anatomy, Faculty of Medicine in Hradec Králové.

Virtual bone

To describe population-specific bone properties, a large number of specimens is required. One option is to gather a cadaver-based material, which is very convenient for traditional biomechanical testing but challenging to obtain a number sufficient for robust statistical evaluation. As we have been seeing rapid progress in the use and general quality of various imaging techniques in hospitals, the second option, i.e. body scans and derived virtual models, seems more promising.

Anatomically correct representation of the specific bone can be easily obtained from computer tomography scan. The data is acquired by combining a wide fan beam (x-ray tube) and detectors that rotate slowly around the patient. Detectors measure photon attenuation, and these intrinsic differences in X-ray absorption provide contrast in CT images [42, 43]. By setting a threshold value of radiodensity, an operator can segment a specific tissue from a single CT image in the data set. Further, link all the images and create a 3-dimensional virtual object (Fig. 9,10). This approach is well-proven, either for dry bone compatibility [44, 45] or for the contemporary forensic investigations [46-48].

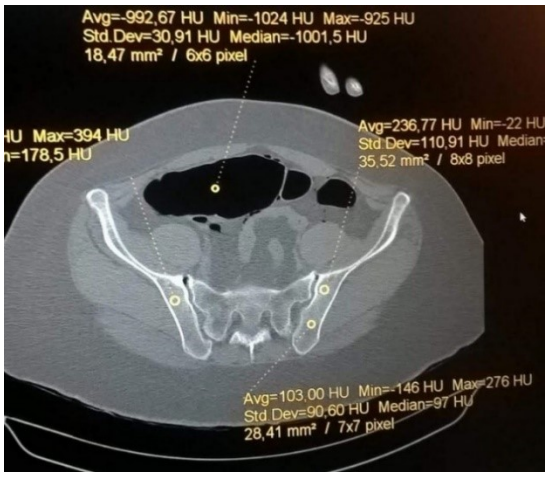

Fig. 9: A clinical CT scan with average HU of selected sites. With permission of the Department of Radiology, Faculty Hospital in Hradec Králové.

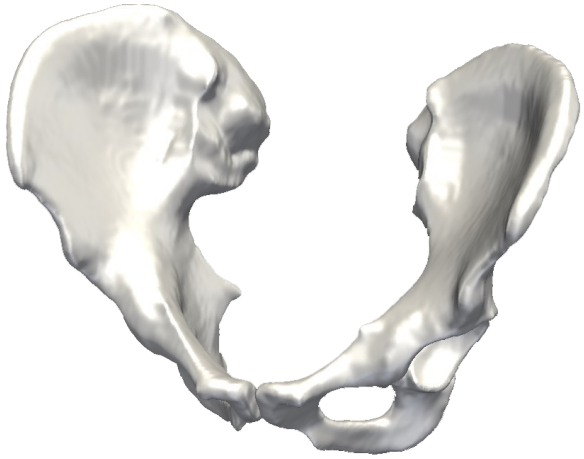

Fig. 10: Pelvic bones model, based on a surface mesh covering the segmentation borders.

Despite its efficient structure, the pelvis can become damaged due to side impact forces so typical for car accidents. Moreover, the tumour or tumour-like lesions (metastases, chondrosarcoma, osteosarcoma), age related problems (osteoporosis, arthritis), infection and non-infectious inflammatory conditions (sarcoid, tuberculosis) or Paget's disease alter the internal bone conditions [49]. The imaging methods can capture both shape and material properties, allowing us either to predict the bone behaviour according both in normal and in diseased bones.

The complexity of pelvic bone in terms of shape, bone tissue distribution and function is unique and present an excellent model to study.

Bone biomechanics

When a structure is subjected to loads, the structure deforms. All the factors influencing the efficacy of bone are understood as its biomechanical properties. Through their analysis, it is possible to describe the capacity of bone overall to support the loads to which it is subjected [50, 51].

Bone stiffness

Bone stiffness is one of the properties defying the overall bone quality. Stiffness contributes to the ability of the bone to resist deformation, thereby making loading possible where the stiffer bone undergoes less deformation than a more compliant one. Many papers present strong evidence between stiffness and strength, which is usually of higher interest in clinical studies because of its closer relation with possible fractures. But so far, a direct measurement of bone strength in situ is not possible, and its estimation is further influenced by sex, age and post-yield displacement [10]. Furthermore, the purpose of bone is not to resist the fracture (except for skull bones). The purpose is to be sufficiently supportive and strong with cells sensitive to deformation and capable of response, leading to direct control of bone stiffness.

It is important to distinguish between the structural (geometrical) and material (mechanical) properties of bone (Fig. 12). Standard compression/bending or tensile tests are traditionally deployed to find bone structural stiffness. Independently on the performed test (axial, bending, or torsional loading), derived structural stiffness is according to its size and shape defined by the slope of the elastic region of the load-displacement curve. The load-deformation curve before the yield point characterises the structural stiffness and the ultimate load of the whole bone defines strength. On the contrary, the material stiffness is independent of specimen geometry and reflects the intrinsic bio-mechanical characteristics of bone tissue.

This simplified summary of bone stiffness (and strength) will get more complicated, considering the structural complexity and hierarchical organization of a human bone and its anisotropic and viscoelastic design. Both stiffness and strength strongly depend on the orientation of macroscopic tissue (trabecular and cortical), material properties (organic and inorganic) and structural properties (geometry and distribution). The bone itself is further modified by neighbouring muscles [52]. Even more, the bones are continuously in the process of either bone formation, regeneration, or degradation due to applied mechanical stress, such as muscular contraction, impact loading, and gravitational forces.

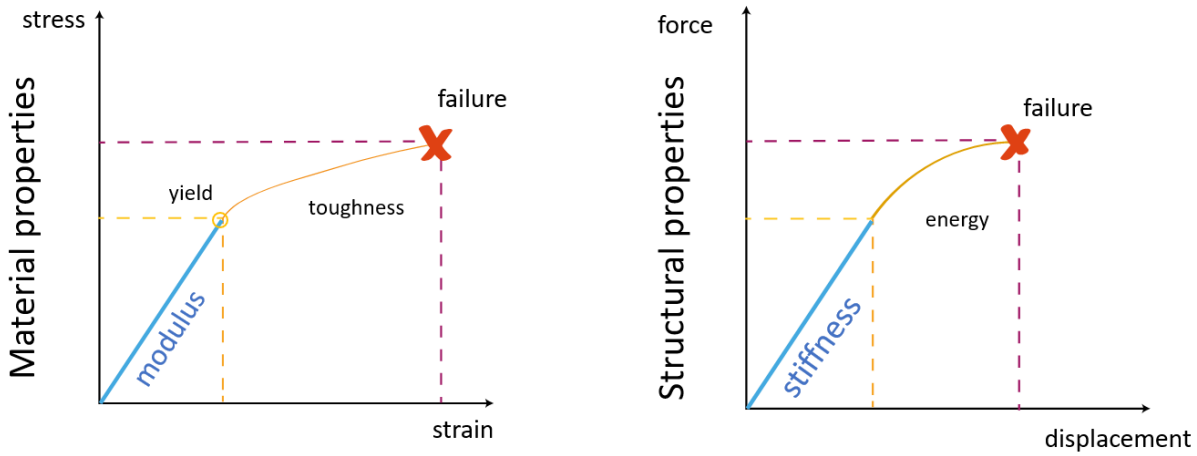

Fig. 12: Material and structural properties. Adopted from Cole et al. [5].

Modulus of elasticity

The modulus of elasticity (Young's modulus) expresses a material stiffness and defines a capacity of an elastic material to be non-permanently deformed. We can demonstrate this intrinsic property by converting the load to stress and deformation to strain. Modulus of elasticity is defined as an initial slope stress-strain curve, where stress is a force applied to the area and strain is the change in length [53, 54]. The larger Young's modulus, the less a material deforms to a given stress, i.e. the stiffer the material. Depending on the body site, physiological and pathological conditions, and methodology related limitations, the average modulus of elasticity of human trabecular bone ranges between 1,2 to 22,3 GPa [55]. The maximum (ultimate) stress is the strength of the bone tissue for given loading conditions. The energy absorbed to failure is the area under the stress-strain curve, known as the toughness [5].

Bone density

Bone tissue is a two-phase porous composite material composed primarily of type 1 collagen and mineralised organic matrix. The ratio of mineral to collagen and degree of porosity affects both bone's strength and stiffness [32, 51] while retaining the ability to regulate mineral ion homeostasis. Term bone density is the product of mineralisation and porosity (prevalence, magnitude and distribution of pores within the bone matrix), expressed as mass per unit of volume [52]. The porosity in human bone varies from about 70 to 80 per cent in cancellous bone sites to 2 to 3 per cent in cortical bone [56]. In human bone, the density value is approximately 1.9 g/cm^3, being slightly lower in cancellous bone and higher in compact bone [51, 57, 58]. Mechanical properties scale with bone mass by a power-law relationship, therefore small changes in mass are followed by significant changes in bone strength.

Although the measurement of bone mineral density (BMD) has been the most widely used technique to estimate bone health for many years, there is no single definition of bone density. Apparent density ($\rho_{app)}$ weights bony tissue structural volume per unit, including bone and marrow space, excluding the bone marrow. Ash density (ρ_{ash}) refers to the portion of bone mineral mass to the bone volume unit. Using the imaging techniques, BMD can be derived from the Gray scale (X-ray), using the dual-energy X-ray absorptiometry (DEXA), from ultrasound or peripheral quantitative CT (pQCT). Measurement of areal bone mineral density by DEXA is considered a method of choice for the clinical diagnosis of osteoporosis and assessment of fracture risk. However, this two-dimensional technique presents several limitations, as it fails to capture the heterogeneity of bone's material composition and, of most importance, the difference between cortical and trabecular compartments. Moreover, it presents low sensitivity to osteoarthritis and degenerative processes artefacts due to local bone density increase.

Bone mineral density is a reliable quantity for determining bone properties. However, caution must be exercised since inaccuracies in BMD, which is proportional to the square of the apparent density, can cause significant errors in predicted bone strength [59].

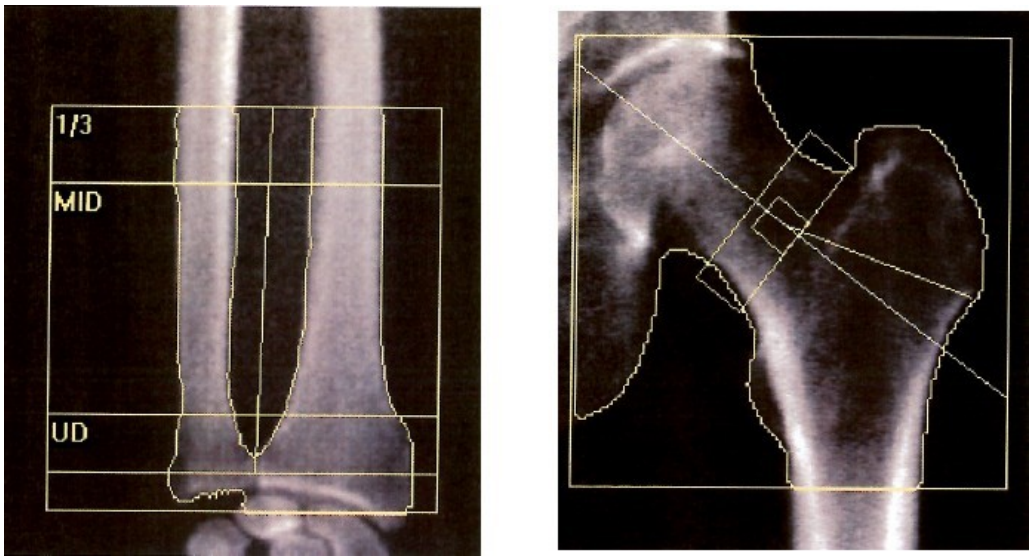

Fig. 13: Densitometry examination. From correspondence with the Department of Clinical Biochemistry and Diagnostics and Osteocenter, Faculty Hospital in Hradec Králové.

Finite element analysis

The finite element method (FEM) was introduced to orthopaedic biomechanics in 1992 by Brekelmans [60] to evaluate stresses in human bones. Based on theories of continuum mechanics, the principle is to reduce a given model to a form solvable by a finite number of numerical operations. The solution is to divide the specific region into small parts called elements, connected at discrete points called nodes [61]. The type, localization, and number of elements affect the results' accuracy [62]. FEM is a unique method that is non-invasive, allows to model complex structures, analyse their mechanical properties and the influence of mechanical forces on given structures. The location, magnitude and direction of an applied force are also measurable [63].

Model warping

Every point of the chosen FE model can be translated using a specified vector array of deformation. The translation follows each point's vector by a given scale factor, while the vectors and scale factors are derived from the dataset properties. This technique can be used to displace point coordinates in an input mesh according to simulated load.

Shape registration

Correct alignment of different subjects' surfaces is crucial to assess the spatial normalization of individual data. Shape normalization is a mathematical tool that compares two or more surfaces with different geometry. It is usually presented as a map between points on one manifold to points on another manifold, which is smooth, differentiable and invertible. As there is generally no isometry between the subjects, the correspondence between surfaces can be found and the amount of stretching needed to fit one surface over another is calculated. This stretching of conformal maps allows us to apply metrics to shapes (Fig. 13).

In clinical praxis, diffeomorphic-based techniques are broadly used in neuroimaging to align the complex and variable cortical brain surfaces [64] but rarely in studies dedicated to bones.

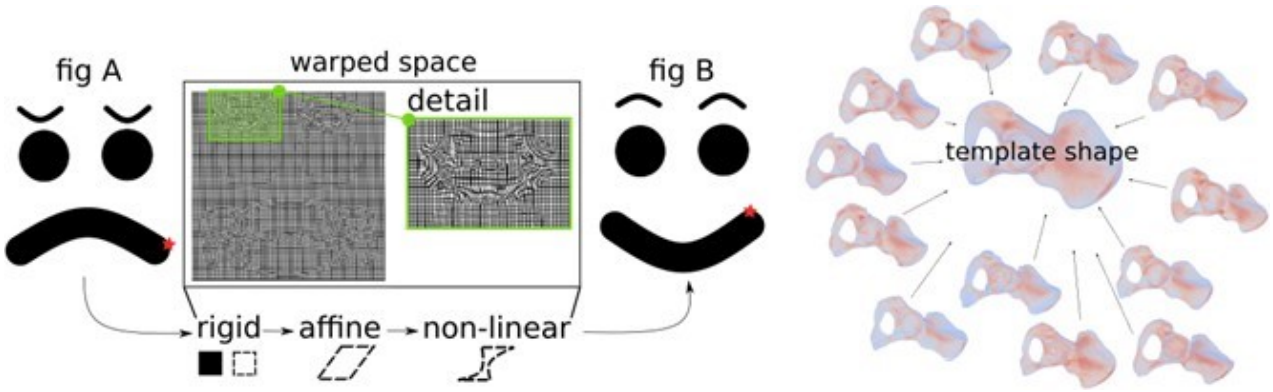

Fig. 14: Shape registration. A continuous change of one shape to another.

Modal analysis

Modal properties help us describe the dynamic behaviour of a given structure, i.e., modal stiffness. It is calculated by solving the eigenvalue problem, mostly with the use of finite element analysis. Its most important property is the eigenfrequency (natural frequency; the eigenvalue in a vibration analysis) and associated eigenvector (the shape of a vibration mode). To solve the problem, we decompose the complicated dynamic movement into the separate modes (eigenmodes), representing separate and independent movements at which all system parts oscillate with the same frequency.

Literature review of density-elasticity relationship

To map calibrated CT based mechanical properties to FE models, it is essential to apply an appropriate relationship between the bone density and its mechanical properties. In other words, we need to connect the (known) BMD derived from the patient's medical records to the (unknown) modulus of elasticity. A newly formed density-elasticity relationship is used to estimate the material stiffness, which will further affect the computations of the structural stiffness.

Setting a study-specific relationship is technically and timely demanding, so the possibility of finding the mathematical equations already introduced in the literature was chosen. There are many relationships used in clinical/biomechanical papers, and for the most accurate modelation, they should be read though and considerably selected.

Density-elasticity relationship

Two major databases were searched through ScienceDirect and Google Scholar, with search terms "density-elasticity relationships", "finite model of pelvis", "pelvic density", "mechanical analysis of pelvic bone", and "pelvic bone mechanics".

Since the DE relationship is to be applied to the CT-based data, studies must meet the following criteria:

The human bones are tested exclusively for the human and animal bones significantly differ [29]. The author explicitly describes the relation between the density and Young´s modulus; the final equation must be compatible with CT scan data.

There are differences between the mechanical properties of the dry bone, even between the bones of different saturation with fluid. Therefore, the specimen must come from the fresh bone [65, 66].

A total of 28 studies and 35 DE relationships passed the review criteria (Tab. 1). The core of the review is a study of Morgan et al. [67], summarizing the methodological discrepancies among relationships proposed in the literature. The most extensive set of specimens was tested by Keller [68], where 496 cubes of human trabecular and cortical bone from the lumbar vertebrae and femurs were analysed. In four studies, the site dependence was ignored, and obtained data were pooled from specimens of several bones [26, 69, 70] or summarized from

partial results [71]. A recent trend is to adopt the subject-specific FE model, so most of the relationships in our review are dedicated to a specific bone. Studies involving the long bones were most prevalent. Eleven reported relationships describe the mechanical properties of the femur [58, 68, 71-80], six stand for tibia [71, 81-85] and one for the ulna [86]. The femur is an obvious choice for mechanical testing as many visits to emergency rooms are associated with its fractures [87]. Therefore, there is a tendency to predict this bone strength as well as improve its interaction with orthopaedics implants. Li and Aspden [74] even report the relationships between the osteoarthritic and osteoporotic bones, a typical finding in a group of older patients.

Six studies provided the DE relationship for vertebrae [68, 71, 88-91], mostly the lumbar.

Two studies report the DE relationship for flat bones, one for pelvic bone [92] and one for scapula [93].

Twenty-three relationships are dedicated to the trabecular bone, three to the cortical. This disproportion is partially caused by the more convenient preparation of blocks of either trabecular or cortical specimens, partially it reflects a need to describe higher variability and mechanical importance of the trabecular tissue in epiphyses of long bones and bodies of vertebrae.

Tab. 1: Density-elasticity relationship in various studies and bone types

Study	Site	E (Gpa)	n
Anderson et al. (1992)	Proximal tibia	$E = 3.890\rho_{dry}^{2.0}$	31
Austman (2009)	Ulna	$E = 8346\rho_{app}^{1.50}$	8
Carter and Hayes (1977)	Pooled	$E = 3.79\varepsilon^{0.06}\rho_{app}^{3}$	124
Ciarelli et al. (2000)	Proximal femur	$E = 7.541(BV/TV) - 0.637$	32
Cong (2011)	Proximal femur	$E = 8050\rho_{ash}^{1.16}$	22
Dalstra et al. (1993)	Pelvis	$E = 2.0173\rho_{app}^{2.46}$	57
Duchemin et al. (2007)	Femur	$E = 10.095\rho_{HA}$	13
Eberle (2013)	Femur	$E = 12.486\rho_{qCT}^{1.16}$	17
Goulet et al. (1994)	Pooled	$E = 6.310(BV/TV)^{2.10}$	104
Gupta (2004)	Scapula $\rho \leq 0.35$ $0.35 \leq \rho \leq 1.8$	 $E = 1049.45\rho^2$ $E = 3000 \cdot \rho^3$	1
Hodgskinson and Currey (1992)	Pooled	$E = 3.98\rho_{dry}^{1.78}$	57
Kaneko et al. (2004)	Distal femur	$E = 10.88\rho_{ash}^{1.61}$	49
Keaveny et al. (1997)	Lumbar spine	$E = 1.540\rho_{app} - 0.058$	9
Keller (1994)	Spine Femur Pooled	$E = 1.89\rho_{ash}^{1.92}$ $E = 10.5\rho_{ash}^{2.29}$ $E = 10.5\rho_{ash}^{2.57}$	199 297 496
Keyak et al. (1994)	Proximal tibia	$E = 33.9\rho_{ash}^{2.20}$	36
Keyak et al. (1998)	Femur $0.6 < \rho$ $0.27 < \rho \leq 0.6$ $\rho \leq 0.27$	 $E = 10200\rho_{ash}^{2.01}$ $E = 5307 \cdot \rho_{ash} + 469$ $E = 33900\rho_{ash}^{2.20}$	18
Knowles (2019)	Glenoid cavity	$E = 32790\rho_{qct}^{2.307}$	14
Kopperdahl (2002)	Vertebrae	$E_{zz} = -34.7 + 3.230\rho_{HA}$ $E_{xx} = E_{yy} = 0.333$	45
Kopperdahl and Keaveny (1998)	Vertebra	$E = 2.1\rho_{app} - 0.08$	44
Li and Aspden (1997)	Femoral head	$E = 1.573\rho_{app} - 0.0094$	49
Linde et al. (1992)	Proximal tibia	$E = 4.778\rho_{app}^{1.99}$	31
Lotz et al. (1990)	Femoral neck	$E = 1.310\rho_{app}^{1.40}$	49
Lotz et al. (1991)	Femoral metaphysis	$E = -13.43 + 14.261\rho_{app}$	123
Morgan et al. (2003)	Vertebrae Proximal tibia Greater trochanter Femoral neck Pooled	$E = 4.730\rho_{app}^{1.56}$ $E = 15.520\rho_{app}^{1.93}$ $E = 15.010\rho_{app}^{2.18}$ $E = 6.850\rho_{app}^{1.49}$ $E = 8.920\rho_{app}^{1.56}$	61 31 23 27 142
Op Den Buijs (2011)	Proximal femur	$E = 29800\rho_{ash}^{1.56}$	22
Ouyang et al. (1997)	Vertebra	$E = 2.382\varepsilon^{0.07}\rho_{app}^{1.88}$	36
Rho et al. (1995)	Proximal tibia Tibial shaft	$E = 6.570\rho_{app}^{1.37}$ $E = 13.000\rho_{app} - 3891$	18 18
Snyder and Schneider (1991)	Tibial diaphysis	$E = 3.891\rho_{app}^{2.39}$	45

.

Methodological differences

Different set-ups have been developed to test the mechanical properties of a bone. Each reported technique has its advantages and limitations, and these methods are further improved over time. The majority of studies use the small blocks of bone to define the elastic modulus of chosen bone by testing its compressing parameters. The most used testing method, reported in fourteen articles, was the platen technique, where the block of tissue is placed between two plates and compressed. Some authors pointed at the experimental problems using the platen technique caused by machine compliance [82], structural end-effects [88] and frictional end effects [82, 94], mostly leading to an underestimation of elastic modulus. Furthermore, different mechanical properties can be found on the specimen's sides, where the trabeculae are cut. Either on sides pointing to the anvils of the material testing machine [88, 95] or on its sidewalls [96] where the trabeculae lose their load-bearing capacity. Ün et al. [97] stated that a layer of 0.2 – 0.6 mm is not taken into account by measurement due to interruption of connectivity of the peripheral trabecular bone.

As a possible solution, a microCT based finite element (microFE) method was employed [98-100]. The principle is to directly convert the 3D voxels of micro-computed tomography images [101] into hexahedral elements, representing the specimen's inner structure. The most significant advantage is getting a non-destructive method respecting the trabecular continuum in the desired direction, it is site-specific and potentially patient-specific. One study developed a DE-relationship using microFE [93]. The limitation of this method is that the bone specimens are not mechanically tested, so effective tissue modulus could not be derived. Three studies used a macroscopic approach and experimentally validated a DE relationship on the whole bones [77, 79, 86]. Intact cadaveric bones were mechanically tested in axial compression and strains to determine local displacements and bone stiffness. Combined with calibrated quantitative computed tomography (QCT) data presenting the bone density, it may provide the loading response for some physiological conditions. However, these values are primarily dictated by the mechanical response of the cortical bone therefore the contribution of trabecular bone is here minimal [102].

Site specificity of DE relationship

Even if we try to minimize all the side-effects of mechanical testing, there is no general application of the given density-elasticity relationship as the bone can adapt to considerable mechanical stress coming from various directions. Many authors just assumed the site-specificity of this relationship [68, 70, 75, 103], until Morgan et al. [71] characterized this site-dependence between elastic modulus and apparent density for human trabecular bone. Different modules were obtained for the same apparent density in the vertebra, tibia, and femur. Morgan found that proximal tibia had a higher modulus than the vertebra and neck of the femur. Greater trochanter had higher modulus than vertebra while these differences could be as large as almost 50 per cent, indicating that there is no universal DE-relationship for on-axis loading. Furthermore, while the trabecular bone is deformed when loaded in compression, increased stress leads to a remodelling process allowing the bone to adapt while the degree of its materialization (mineral heterogeneity) is also changed. The effect of this mineral heterogeneity on the apparent modulus of trabecular bone is yet fully known yet.

Most suitable DE-relationship

DE relationship proposed by Keyak et al. [104] seemed most promising. The study included specimens with a wide density range, describing the properties of cortical, trabecular and even transition areas. This relation is widely used in related literature, therefore, I decided to choose just a slightly modified version capable of improving the results from transition threshold values, as presented and validated in [102, 105, 106]:

$$E_{cort} = 10200 \cdot \rho_{ash}^{2.01} \text{ (MPa)}, \quad \rho_{ash} \geq 0.486 \text{ (g/cm}^3\text{)}$$

$$E_{trab} = 2398 \text{ (MPa)}, \quad 0.3 < \rho_{ash} < 0.486 \text{ (g/cm}^3\text{)}$$

$$E_{trab} = 33900 \cdot \rho_{ash}^{2.2} \text{ (MPa)}, \quad \rho_{ash} \leq 0.3 \text{ (g/cm}^3\text{)}$$

Where $E_{cort/trab}$ is the Young's modulus of cortical/trabecular bone and ρ_{ash} is an ash density (ash mass divided by bulk sample volume).

Material and methods

Original data

Every study depends on a sufficient amount of quality input data. The anonymized retrospective CT data were randomly taken from routine examinations in the Faculty Hospital in Hradec Králové under ethical approval 202010P08 and 202102IO2P. The files were stored in DICOM (Digital Imaging and communications in Medicine) format, CT resolution of the dataset was 0.8x0.8x0.8 mm (Siemens Definition AS+, Siemens Definition 128, both Siemens AG, Erlangen, Germany; 120–130 kV using CareDose, reconstruction kernel 80–90, bone algorithm). The inclusion criteria were as follows: abdominal CT scans, bones without any trauma, and an age range of 20 years or older. The younger persons were excluded due to unfinished ossification (see Fig. 7). The pelvic bone is well suited for our study because of its multifaceted morphology. Moreover, being the most sexually dimorphic skeletal element in the human body, it could further serve as a model for sex identification.

As the data set was continuously updated, the exact number of involved patients will be specified in the following chapters.

In the final part of this thesis, the applicability and utilisation of the proposed method are being discussed. For this purpose, one human femur was randomly chosen from the historical osteological collection (property of Anatomy Department, Medical Faculty in Hradec Králové) and CT scanned in the same settings as the clinical CTs. As all the bones from anatomy collection are former ossuary deposits, no ethical approval was required for this study.

Segmentation and shape registration

The segmentation process runs in free open-source software MITK-GEM (The Medical Imaging Interaction Toolkit), which is widely used to generate superficial meshes from bones [107, 108]. The process is presented in Fig. 15. It comprises the image cropping (selection of either left or right pelvic bone), semiautomatic segmentation (to distinguish bone from soft tissues) and finally the surface mesh generation (to allow further use of finite element method). The algorithm may sometimes fail to find the exact borders between the bones (sacral bone & pelvic bones, pelvic bones & the femur) fused via osteophytes. Therefore, in some cases, I had to correct the errors in the segmentation manually.

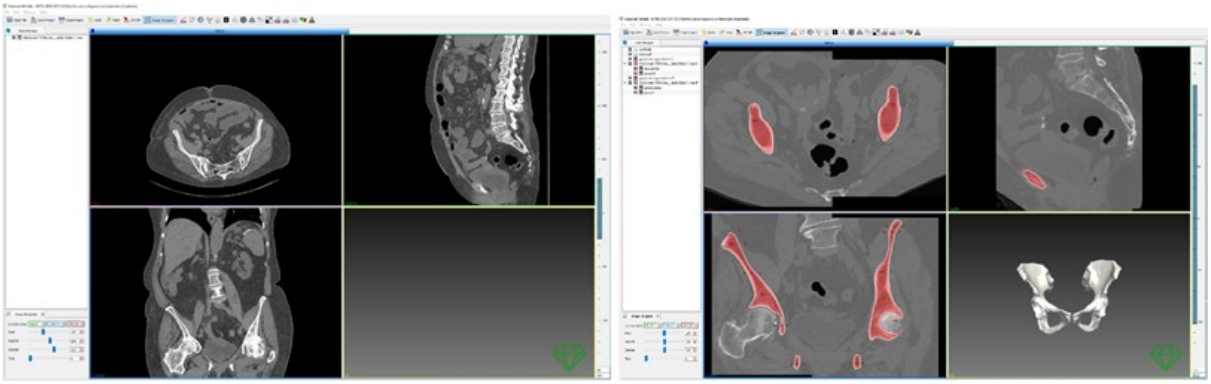

Fig. 15: Process of bone segmentation and surface mask generation.

Shape registration is the following step because each sample (bone) has different size and shape. However, bone samples are anatomically and topologically equivalent. This implies the existence of a point correspondence between two shapes under some suitable class of bijective maps and similarity metrics. The purpose of image registration is to geometrically align the so called moving image I to the so called fixed image J by a suitable class of maps (see Fig. 16). These maps transform each voxel x in the moving image I (x) to the corresponding voxel y in the fixed image J (y) by minimising a cost function that expresses the differences between I (x) and J (y). These transformations were computed by a well–known diffeomorphism method SYN in library ANTs with a modified intensity-based criterion called the "demons-like metric" [109]. The algorithm worked in the four-step resolution [100, 100, 50, 30] (the numbers in parentheses represent maximum optimisation iterations). A suitable template bone must be created in such a way that it minimises the anatomical discrepancies between the template bone and any sample it is morphed into. The template bone shape was iteratively estimated according to [109]. Once the template bone was obtained, all the samples in the dataset were morphed into the template bone shape. Each morphed bone sample was visually inspected for the presence of any errors. Both the original CTs, which hold information about the bone density, and segmented models, describing the bone shape served as a basis for follow-up studies.

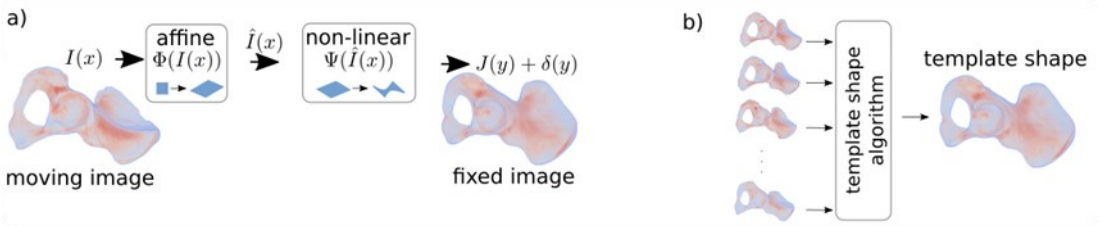

Fig. 16: a) An illustration of the steps of the registration algorithm: the affine transform globally translates, rotates, scales and shears the moving image; the non–linear transform deforms (voxel-wise) the moving image in order to align the moving image with the fixed image. b) The fixed image is a template shape that is estimated from the dataset.

Sub-steps/follow up studies

Several sub-steps had to be done to develop a model describing the biomechanical properties of the pelvic bones. Firstly, due to the relatively large data set, a new algorithm capable of automatically defining bone diameters and bone shape was written and tested (section Registration algorithm). Next, the mathematical model was developed, showing the possibilities of modal analysis to acquire the structure's smallest stiffnesses (section Modal analysis). This work was followed by investigating population-wise spatial and temporal differences in bone mineral density (section Density distribution). As a fulfilment of this thesis aims could be considered the application of previous results to the patients' CT scans, leading to a complex method of pelvic bone characterisation (section Characteristic stiffness).

Below, each part's main ideas, methods, and results are described separately.

Registration algorithm - automatic measurements

This part of the work sets a computational background for the shape recognition of all the pelvic bones in a dataset. An automated segmentation technique was developed and tested on models derived from clinical CT scans to pair the internal properties of a single bone (stiffness, BMD) with the external properties (bone morphology).

In recent years, we have been seeing rapid progress in the use of imaging techniques in forensic anthropology and biomechanics. Many studies have proven their compatibility with previous research on dry bone [44, 45] and found that CT scans are a promising source of reference data in contemporary forensic investigations [46, 48, 110]. It has been demonstrated that the accuracy of defining anthropological landmarks both manually and by use of CT scans has led to similar results between them [46, 111-114]. Therefore, the many methods that determine the sex of an individual, as well as the physical or biomechanical properties of a population that are already established and proven for skeletal material, could also be adopted for clinical CT data.

Regardless of the bony specimen origin, processing requires time and skill. The idea was to reduce the time involved by adopting the technique of shape morphing for the mass analysis of anthropometric data. We adopted a non-linear registration algorithm that automatically computes the landmark positions from the pre-defined ones. The registration algorithm based on diffeomorphic mapping has been successfully used in brain analyses [115] but rarely in the bone analysis [116, 117].

Material and methods

The sample population was equally balanced in sex (100 males, 100 females), with the average age being 64 ± 13.5 years. This chapter uses transformations described in Shape registration section to map anatomical landmarks from template shape onto a sample shape.

Anthropological Measures

The template bone was set by a group of anthropometric reference landmarks B1, B2, ..., B19 with the associated distances M1, M2, ..., M10 (see Tab. 2 and Fig. 17), by utilizing ParaView software [118]. We adopted the landmarks defined by Murail and Bruzek [119], both for their acceptance in the published literature [120] as well as for their sex–specificity. One additional landmark B20 was added to test the accuracy of the algorithm on the concave surfaces (the bottom of the acetabular fossa).

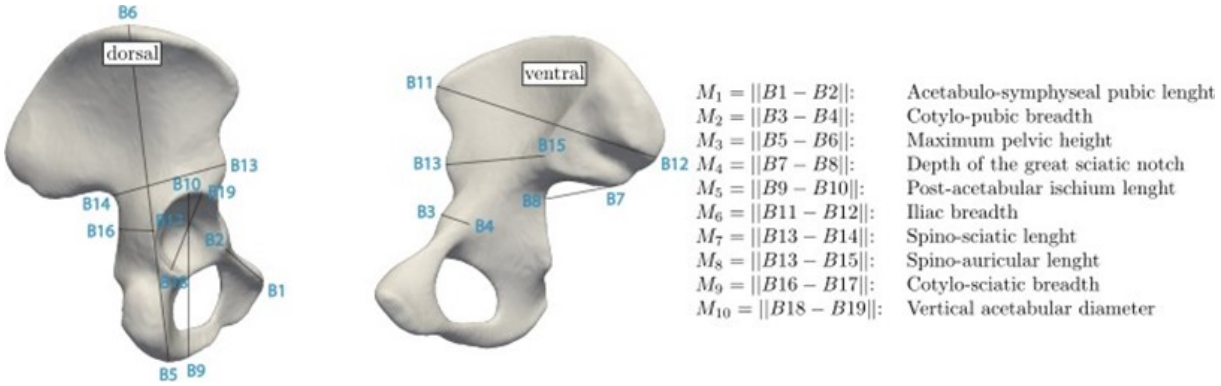

Fig. 17: The estimated shape of the template bone with the reference landmarks B and distances M.

Tab. 2: Definitions of the reference landmarks B.

B1	Symphysion; the most superior and medial point on the pubic symphysis
B2	Anterior border of the acetabular rim at the level of the lunate surface
B3	The most lateral point on the acetabular rim
B4	A point on the medial margin of the pubic bone; at the level of B4
B5	The most inferior point of the os coxae
B6	The most superior point of the os coxae
B7	The posterior inferior iliac spine
B8	A point on the anterior margin of the great sciatic notch
B9	The most anterior and inferior point on the ischial tuberosity
B10	The furthest point on the acetabular margin from B9
B11	Anterior superior iliac spine
B12	Posterior superior iliac spine
B13	Anterior inferior iliac spine
B14	The deepest point in the greater sciatic notch
B15	The contact point of the arcuate line and the auricular surface
B16	The midpoint of the anterior portion of the greater sciatic notch
B17	A point on the lateral border of the acetabulum; at the level of B16
B18	The most inferior point on the acetabular rim in the longitudinal axis of the ischium
B19	The most superior point on the acetabular rim on the longitudinal axis of the ischium
B20	Deepest point of the acetabular fossa

A Comparison of Manually and Automatically Seeded Landmarks

To evaluate the accuracy of automatic seeding algorithm, an operator manually seeded defined landmarks on 50 bones randomly selected from the dataset.

Intra–observer Error

I checked the consistency of manual seeding by analysing the intra–observer error in distances M. Fifty pelvic bones were remeasured twice (test1 and test2) by a moderately experienced operator with a two-week time window. The intra–observer technical error of measurement (TEM) and the percentages expressed relative rTEM were calculated. The resulting TEM index is a variable in anthropology that is used to express the margin of error and the quality of measurement. The mutual dependency of all tests is further expressed as the reliability coefficient R, that describes variance, which is free of measurement errors [121-123]:

$$\mathrm{TEM} = \sqrt{\frac{\sum_{j=1}^{n} d_j^2}{2n}}$$

$$\mathrm{rTEM} = \frac{\mathrm{TEM}}{\bar{m}} 100$$

$$\mathrm{R} = \frac{\mathrm{TEM}^2}{\sigma}$$

where n is the number of pelvis samples, $\bar{m}$ is the average distance value M, over the n samples, σ is the standard deviation over the n samples and d_j is the difference of M on the jth sample that is computed from the two measurements.

The Distance Between Automatically and Manually Seeded Landmarks B

To analyse the differences between both automatically and manually seeded landmarks, the Euclidean distance was computed

$$\Delta i = ||x_i - \hat{x}_i||$$

where x_i and $\hat{x}_i$ are the coordinates of the ith landmark B, that were obtained manually and automatically, respectively (see Fig. 18). We analysed the distances on the samples from subsection Intra–observer Error. The statistical difference between landmarks B, measured at both repetitions was measured by the Mann Whitney test with a probability level of 95 %.

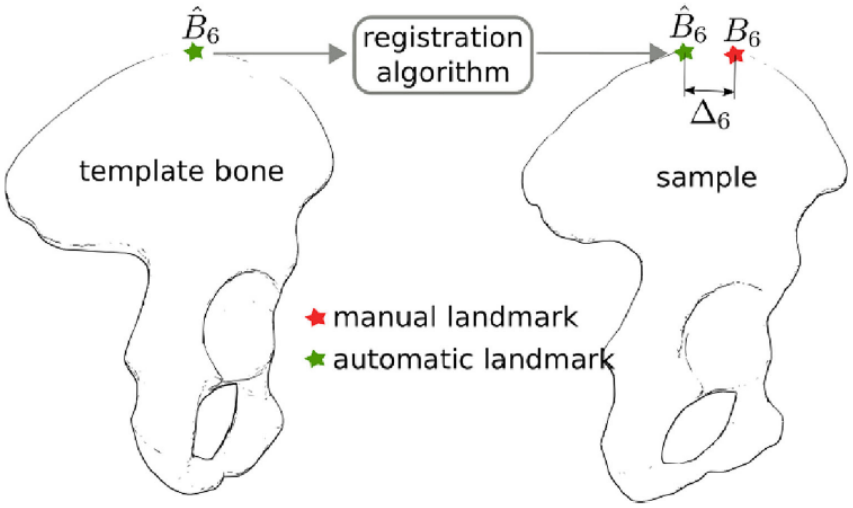

Fig. 18: An example of measurement of distance between manually and automatically seeded landmark B6.

The differences Between Automatically and Manually Computed Distances M

Relative differences between automatically and manually computed distances M, were analysed from samples of subsection Intra–observer Error, see Fig. 19. The ith relative distance difference δi was computed as $100(\mathrm{M_i} - \widehat{\mathrm{M}}_\mathrm{i}) \,/\, \widehat{\mathrm{M}}_\mathrm{i}$. The statistical difference between distances M, measured at both repetitions was measured by the Mann Whitney test with a probability level of 95 %.

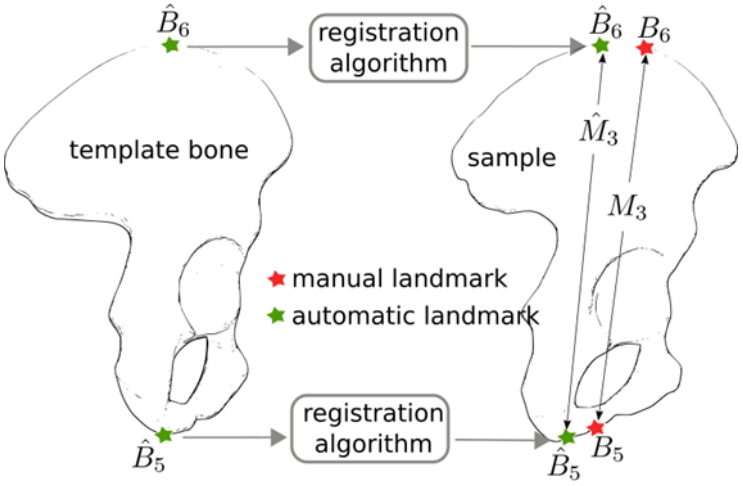

Fig. 19: An example of the distance M3 computed from the manually seeded landmarks B5 and B6 and the distance $\widehat{M}3$ computed from automatically seeded landmarks $\hat{B}5$ and $\hat{B}6$.

The Analysis of Clouds: The Back–Mapped Landmarks

The manually defined landmarks on the samples from subsection Intra–observer Error were mapped onto the bone template. The mapped landmarks form clouds around the reference landmarks. These landmark clouds have a certain shape, size and centroid (mean coordinates), which are used to analyse the accuracy of registration algorithms, see Fig. 20. The centroids and confidence ellipsoids (eigenvalues of the covariance matrix) were estimated for the landmark clouds by the Quadratic Discriminant Classification Method (QDCM) [124]. By using the QDCM, one can estimate the probability that a given reference landmark belongs to the corresponding landmark cloud. The QDCM was trained by samples from subsection Intra–observer Error. The stratified KFold strategy with 3 folds and a train/test splitting at 70%/30%, was chosen in order to obtain the best accuracy [124]. The mean resultant train/test accuracy metrics were 92% 6.1%/90% 8.3%. Besides, we computed the distance Δ, between the centroids and the reference landmarks.

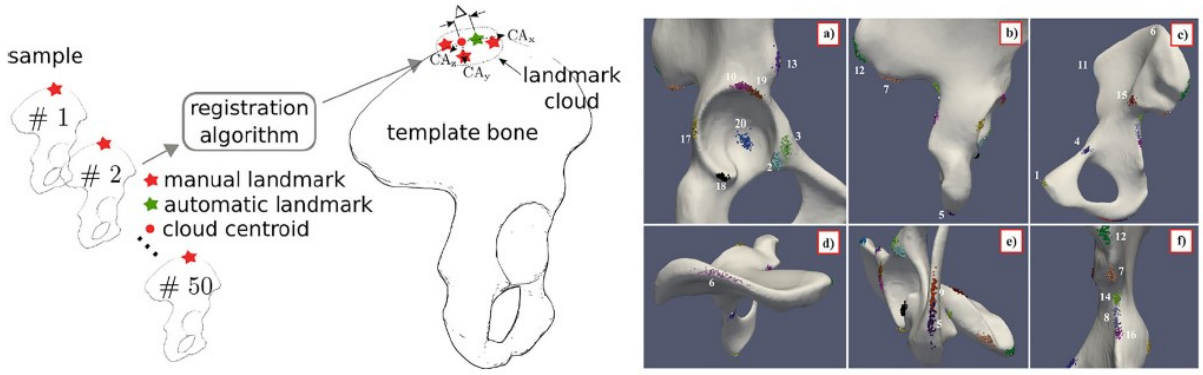

Fig. 20: Use of registration algorithm for the mapping of manually seeded landmarks onto the bone template. The set [CAx CAy CAz] represents eigenvalues of a 95 % confidence ellipsoid. Individually coloured clouds are shown on various aspects of the pelvic bone [a), b), c), d), e), f)]. The numbers correspond to the landmark numbers in Fig. 17.

Modal properties

This part of the work aimed to set a theoretical base for further research, i.e., to introduce several computational examples, as well as an optimisation algorithm that searches for the smallest stiffness of structures. The core is to find the locations of force that can maximize the strain energy or compliance of a given structure in consideration of the statics equilibrium equation. The problem was cast into a maximization problem, the optimization was gradient-based, and verification of results was investigated via the spectral decomposition method.

Firstly, the relation between modal and static stiffness was derived from truncated spectral decomposition. Consequently, the hypothesis was formulated that the smallest static stiffness and its direction can be found from truncated spectral decomposition. Further, the theory was demonstrated by analysing a beam stiffness under two types of boundary conditions. An optimisation algorithm based on strain energy maximisation was developed to find the smallest stiffness as an alternative to spectral analysis. Both approaches were tested and compared on examples of regular and complex shape structures.

This section is essential for further computational data processing; however, as the author contributed minimally to this part, just the basic information is presented here. Detailed computations and results can be found in [19].

Mineral density distribution

To increase the population specificity of the smallest stiffnesses, the last co-research aims to find any difference in spatial or temporal (age) distribution of bone mineral density and bone mineral content. Even though these changes are generally anticipated, they have never been fully quantified and described.

The structural and intrinsic properties of bone are inhomogeneous and vary across the multiple spatial and temporal scales and populations. Structural inhomogeneities are related to bone fragility and toughness [125-128]. The bone mineral density (BMD) is widely used to study bone properties. Even BMD is remarkably inhomogeneous [125, 129], connected to bone elasticity and fracture risk [105, 130, 131].

The spatial variation of BMD was previously analysed through variograms [132, 133], where the authors attempted to enhance the fracture risk prediction ability related to BMD. Other studies demonstrated significant correlations of variogram parameters with trabecular bone morphological measures and bone strength [134]. On the opposite, the relation of vertebrae strength and variogram parameters was not significantly correlated in [135].

Firstly, a shape registration algorithm was used to geometrically align CTs (see Shape Registration). After an internal calibration of each CT, the BMD was projected into the FE space, and spatial characteristics were computed to obtain age/sex/BMD dependence. All steps are presented in Fig. 21.

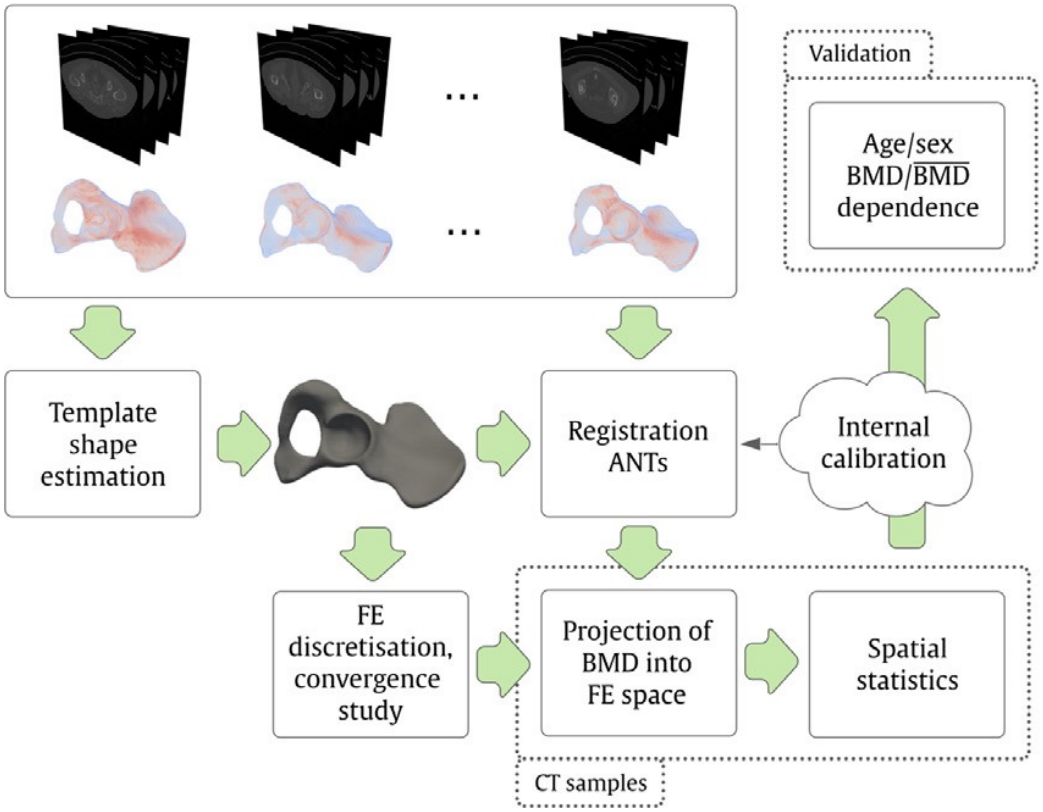

Fig. 21: Bone mineral density. A flowchart of the study.

Materials and Methods

The anonymized retrospective CT data of 97 females and 88 males were randomly taken from routine examinations in the Faculty Hospital in Hradec Králové. The sample population age per sex is in the range of 22–88 years, divided into ten bins, where each bin contains more than five samples. The CT scans were calibrated internally, resulting in BMD [136]. The HU values of air, bone tissue, fat, blood and muscle were considered for internal calibration, as shown in Fig. 22. Only the right-hand side pelvic bone was considered because no significant difference was explored between the left and right sides.

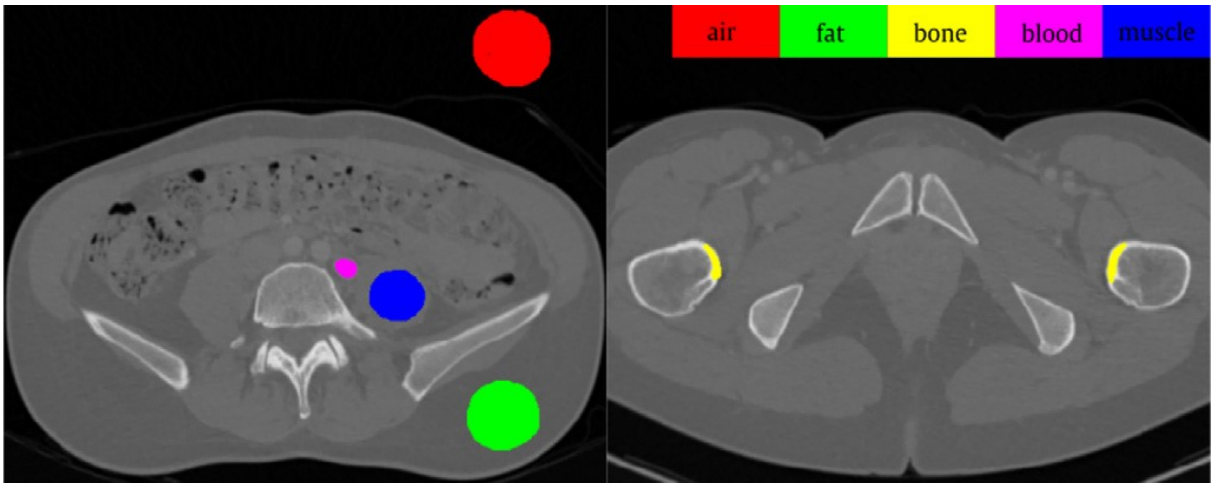

Fig. 22. Example of CT slice where HU values of the considered tissues were selected for internal calibration. ROI content (mm^2): air: 1312; fat: 1109; bone: 160; blood: 92; muscle: 618. Mean HU (standard deviation): air: -1002 (7); fat: -90 (12); bone: 1233 (236); blood: 217 (16); muscle: 60 (12).

The template geometry described by the implicit HU field was transformed into a triangulated surface by marching cube algorithm [137]. The resultant triangular mesh was used to build the volume tetrahedral mesh (fTetWild) [138]. The computer analysis of BMD in the original CT data space is inefficient. Therefore, the BMD is projected into a suitable space with fewer degrees of freedom. In fact, this projection is an approximation of the BMD by piecewise (dis)continuous functions using the least-squares method. The morphed fields from the dataset were projected onto a discontinuous FE space constructed on template mesh. Then, all samples in the dataset shared the same geometry domain and finite element space [18].

The average bone mineral density ($\overline{\mathrm{BMD}}$) is an integral value, defined as

$$\overline{\mathrm{BMD}} = \int_{\Omega} \rho \, \mathrm{d}\Omega$$

and describes the spatial average of the BMD. This value allows us to compare the density distribution regardless of the structure shape and size.

Characteristic stiffness

In this chapter, the newly formulated mechanical metrics (see Modal properties) are tested for their sex classification capability and compared to the pelvic bone's common anthropometric measures and natural frequencies. Further, the smallest static stiffness of the pelvis with respect to the applied boundary conditions is analysed. The new metric can be considered as a modal stiffness, which allows to reconstruct the static stiffness of a bone. Through the study, modal stiffness, smallest static stiffness and natural frequency are called eigenmetric.

Bone stiffness is generally location and direction dependent. It requires a precise and often complex experimental protocol for measuring [6, 10, 139, 140] or computational approaches such as finite element (FE) models [9, 141, 142]. The key idea is to apply spectral decomposition of a stiffness matrix (usually obtained from a FE model). The resultant eigenpairs composed of eigenvalues and associated eigenvectors contain unique information about the modal as well as static stiffness. These pairs have the following properties:

A) rotation/translation invariant,

B) naturally considering the structural/intrinsic bone properties (i.e., bone shape, internal structure, bone material, bone elasticity, bone density),

C) under certain conditions provide the minimal bone stiffness for given boundary conditions together with associated deformation shape,

D) does not necessarily require boundary conditions defined.

A) This property allows to compare arbitrarily rotated bone geometries, and it has furthermore been demonstrated in shape analysis [143, 144]. B) The stiffness is constructed often by FE method, where the geometry and material properties are discretized together and represented by a big sparse matrix. C) The stiffness matrix should be symmetric (positive definite) and constant to obtain minimum static stiffnesses and corresponding eigenvectors. D) If no kinematic boundary conditions are provided, the spectrum of eigenvalues close to zero contains the eigenvalues corresponding to rigid movement of the body (it means the three translational and three rotational moves of a body in 3D), followed by regular deformable eigenvalues.

Materials and methods

The heterogeneous sample population CT data obtained from anonymised routine CT scans (mean age 64 13.5, gender balanced 100 females/males) consisting of 200 left/right pelvic bones. The masks from CT segmentation were converted to an STL (stereolithography format) representation (VTK library [137]) and, in consequence, volume finite element meshes were automatically built with library TetWild [138], see Fig. 23. First, the CT values were transformed to an effective density in order to compute total mass of the bones ρeff = bCT, where the scaling coefficient is b = 658 g/cm^3 [145]. The CT scans were calibrated internally to estimate Young's modulus, resulting in hydroxyapatite content in bone [136]. The density–Young's modulus in [MPa] relationship

$$E(\rho_{ash}) = \begin{cases} 10200\rho_{ash}^{2.01}, & \rho_{ash} \geq 0.486 \\ 2389, & 0.486 > \rho_{ash} \geq 0.3 \\ 33900\rho_{ash}^{2.2}, & \rho_{ash} \leq 0.3 \end{cases}$$

was used where $\rho_{ash} = 0.877\rho HA + 0.08$ gcm^3 [68, 84, 105]. The Poisson's ratio ν is defined as a constant 0.3 [145] over the whole bone domain.

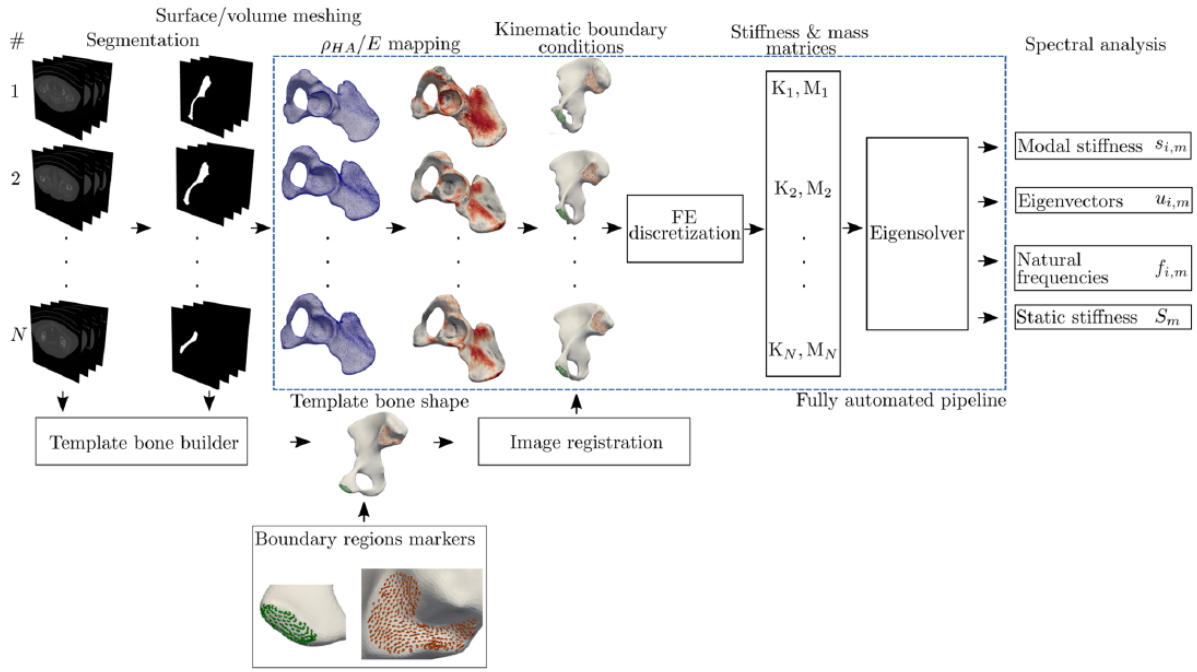

Fig. 23: A pipeline of building the FE model based on the CT data. The boundary points(green/orange) are used to apply the kinematic boundary conditions.

Two sets of boundary conditions were built. The first model, FEMP-I described the fixed boundary conditions, see Fig. 23. The fixed boundary conditions were inspired by previous works [146] and mimicked the physiological conditions up to some extent. The second model considers no kinematic and no force boundary conditions, called FEMP-II. Based on the geometry, material and boundary conditions defined, the stiffness and mass matrices K, M are constructed with the help of finite element method in a usual sense:

$$\mathrm{K} = \bigcup_{e \in \Omega} \int_{\Omega_e} \nabla \mathrm{u}_e : \mathrm{C}(E, \nu)_e : \nabla \delta \mathrm{u}_e \, \mathrm{d}\Omega_e,$$

$$\mathrm{M} = \bigcup_{e \in \Omega} \int_{\Omega_e} \rho_e \mathrm{u}_e \cdot \delta \mathrm{u}_e \, \mathrm{d}\Omega_e$$

The operator V is a symmetric gradient of displacement u. The displacement u and its variation δu are approximated with an arbitrary linear piece-wise continuous functions (ie., in Fenics notation: P1 Lagrange finite element [147]), while C_e represents the tensor of material coefficients inferred from density-elasticity relationship and approximated on the discontinuous finite element space of zero order (ie., in Fenics notation DG0). The stiffness matrix was discretized on tetrahedral mesh domain Ω representing the bone geometry. The characteristic element size is 1 mm, which corresponds to 800 000–1 100 000 elements. The element size is estimated at auxiliary convergence study on five eigenvalues, which should change up to 5% between two mesh resolutions in L2 norm. Once the element particular quantities are constructed, the global stiffness matrix K is assembled (assembling operator ∪). The details of presented FE discretizations of stiffness matrix can be found for example in [147]. The homogeneous fixed boundary conditions are injected into stiffness matrix K on an algebraic level by proper zeroing rows and columns (see the manual for Fenics library [147]). Once the stiffness matrix is built up, the following generalized eigenvalue problem can be formulated:

$$\mathrm{K}_m \mathrm{u}_{i,m} = \lambda_{i,m} \mathrm{M}_m \mathrm{u}_{i,m}, \; i = 1, \ldots, n, \; m = 1, \ldots, N$$

where $\lambda_{i,m}$ and vector $u_{i,m}$ are i'th eigen value and eigen vector associated with sample m, respectively. In order to compute those eigen pairs, LOBPCG solver from SLEPc library was used to find 10 smallest real eigenpairs [148]. The overall computational framework is written within problem solving environment library Fenics 2018.1 [147].

Eigenmetrics definition

The norm of the eigenvector ||ui|| of a m'th sample is defined as a pointwise norm:

$$||u_{i,m}|| = \sqrt{\text{diag}(u_{i,m}^{rs}(u_{i,m}^{rs})^T)}$$

where eigenvector $u_{i,m}^{rs}$ is reshaped to have a new dimension, which contains pointwise three components x, y, z of a vector in 3D. To localize the point where the stiffness of structure is potentially lowest one, it is possible to find a maximum of above norm of eigenvector and corresponding index k of point. This corresponds with looking for maximum of compliance:

$$k = \arg\max(||u_{i,m}||)$$

Once we have determined the index k we can compute i'th modal stiffness of m'th sample as

$$s_{i,m} = \frac{\lambda_{i,m}}{(||u_{i,m}||[k])^2}$$

The static stiffness at point with index k is computed in virtue of modal superposition described in [19] and can be expressed as:

$$\frac{1}{S_m} \approx \sum_{i=1}^{\hat{n}} \frac{(||u_{i,m}||[k])^2}{\lambda_{i,m}}$$

where $\hat{n}$ is the number of eigen pairs included. Static stiffness can also be understood as the ratio of force and deformation. Within ten eigenpairs, approximation error is 4%, which is acceptable in terms of speed and accuracy of truncated spectral decomposition. The natural undamped frequency is defined as usual:

$$f_{i,m} = \frac{\sqrt{\lambda_{i,m}}}{2\pi}$$

The proposed definitions of modal stiffness s_i as well static stiffness S were based on the theoretical and computational study [19].

Anthropometric analysis of pelvic bones

The shape of the pelvic bones was parametrized by a series of points called B1, B2, ..., B19 and associated distances M1, M2, ..., M10, see chapter – Registration algorithm. These points and distances has been adopted from DSP2 tool (Diagnose Sexuelle Probabiliste [119]). DSP2 is capable of sexing the bone specimens by computing the probability of being male or female using the combination of sex sensitive variables (measurements). Chosen points and distances do not only describe the shape of bone, additionally they provide a set of sex-specific data. Given the inter-individual variability of human pelvic bone, one measurement only does not suffice for reliable gender classification, nevertheless they could provide strong base for further anthropometric analysis.

Automatised construction of boundary conditions and anthropometric points

To decrease the operator error in construction of large number of FE models, the automatized generation of fiducial points as well as boundary condition elements, the deformable registration was employed, see Materials and methods – Shape registration. The correlation between automatically and manually computed anthropometric distances is shown in Tab. 3. The highest correlation was achieved for the first operator and the distance M3, while the lowest correlation was achieved for the distance M4 measured by first operator. Moreover, the sex classification trained by automatically computed anthropometric distances performs slightly better in comparing to manually computed distances (ACU/AUC 0.87 0.1/0.96 0.1 with all distances included at once versus ACU/AUC 0.85 0.1/0.93 0.1 with all distances included). The smallest correlation was obtained for fifth modal stiffness s5 in case of first operator, see Tab. 4. The sex prediction performance was achieved a similar for both manual and automatic approaches with all modal stiffnesses included at once (ACU/AUC 0.91 0.2/0.94 0.2). To determine the accuracy of the automatic boundary marking, in the Tab.4 the correlation metrics are computed.

Tab. 3: Correlation metrics between automatically and manually computed anthropometric distances.

	operator I: Pearson's.coef		operator I: CI(95%)		operator II: Pearson's.coef		operator II: CI(95%)	
distance	rep. #1	rep. #2	rep. #1	rep. #2	rep. #1	rep. #2	rep. #1	rep. #2
M_1	0.94	0.94	[0.91, 0.97]	[0.90, 0.97]	0.92	0.98	[0.91, 0.95]	[0.94, 0.99]
M_2	0.94	0.94	[0.91, 0.97]	[0.90, 0.97]	0.90	0.95	[0.88, 0.93]	[0.97, 0.99]
M_3	0.98	0.98	[0.97, 0.99]	[0.97, 0.99]	0.95	0.93	[0.93, 0.99]	[0.91, 0.98]
M_4	**0.77**	0.80	[0.63, 0.87]	[0.67, 0.88]	0.81	0.81	[0.79, 0.84]	[0.80, 0.85]
M_5	0.84	0.99	[0.75, 0.91]	[0.99, 1.00]	0.83	0.91	[0.74, 0.91]	[0.85, 0.96]
M_6	0.95	0.93	[0.92, 0.97]	[0.89, 0.96]	0.95	0.93	[0.92, 0.97]	[0.89, 0.96]
M_7	0.96	0.97	[0.94, 0.98]	[0.96, 0.99]	0.91	0.95	[0.89, 0.94]	[0.93, 0.98]
M_8	0.84	0.77	[0.73, 0.91]	[0.64, 0.87]	0.87	0.82	[0.79, 0.92]	[0.75, 0.89]
M_9	0.97	0.97	[0.96, 0.99]	[0.96, 0.99]	0.95	0.96	[0.92, 0.99]	[0.92, 0.99]
M_{10}	0.96	0.97	[0.94, 0.98]	[0.95, 0.98]	0.93	0.95	[0.92, 0.98]	[0.93, 0.98]

Tab. 4: Correlation metrics between modal stiffness computed on model

	operator I: Pearson's.coef		operator I: CI(95%)		operator II: Pearson's.coef		operator II: CI(95%)	
modal stiffness #	rep. #1	rep. #2	rep. #1	rep. #2	rep. #1	rep. #2	rep. #1	rep. #2
s_1	0.91	0.93	[0.82, 0.96]	[0.89, 0.98]	0.90	0.91	[0.82, 0.94]	[0.87, 0.98]
s_2	0.90	0.93	[0.85, 0.93]	[0.90, 0.97]	0.87	0.90	[0.81, 0.91]	[0.85, 0.94]
s_3	0.96	0.99	[0.90, 0.99]	[0.93, 0.99]	0.95	0.91	[0.90, 0.99]	[0.87, 0.97]
s_4	0.91	0.94	[0.84, 0.96]	[0.90, 0.98]	0.88	0.89	[0.81, 0.92]	[0.84, 0.93]
s_5	**0.73**	0.81	[0.66, 0.84]	[0.75, 0.89]	0.83	0.79	[0.76, 0.83]	[0.72, 0.84]
s_6	0.84	0.95	[0.80, 0.91]	[0.91, 0.98]	0.90	0.91	[0.85, 0.94]	[0.87, 0.95]
s_7	0.91	0.94	[0.85, 0.96]	[0.90, 0.98]	0.89	0.91	[0.84, 0.94]	[0.86, 0.96]
s_8	0.87	0.93	[0.79, 0.91]	[0.88, 0.87]	0.83	0.87	[0.77, 0.89]	[0.79, 0.92]
s_9	0.92	0.97	[0.89, 0.96]	[0.89, 0.99]	0.85	0.91	[0.80, 0.89]	[0.83, 0.98]
s_{10}	0.91	0.94	[0.86, 0.98]	[0.87, 0.98]	0.88	0.93	[0.81, 0.91]	[0.89, 0.98]

Statistical evaluation

Ensemble random forest method was used to binary classify SEX and SIDE variables. The relation between continuous anthropometric variables and eigenmetrics was analysed with Spearman's correlation on a significance level 95%. The classification is evaluated with sensitivity/specificity/area under curve (AUC) metrics summarized in receiver operation characteristic (ROC) based on 5-fold cross-validation procedure [124]. The Pearson's correlation was used to measure the degree of correspondence of automatized and manually measured anthropometric distances M. In order to achieve a reliability of manual measuring of distances, two operators with two repetitions computed the anthropometric distances of 50 samples, hence four correlation values are reported. The same reliability test was used to analyse manual and automatic computing of boundary conditions markers.

Results

Registration algorithm - automatic measurements

Observer agreement

TEM values were in the range of 0.60 for M9 and 1.55 for M4, see Tab. 5. The values of rTEM were mostly less than 2%, except for M2 and M4, which were 2.27 and 3.51, respectively and according to [149] are considered as being imprecise. The coefficient of reliability R was between 0.94 and 0.99 and is defined as being high for all measurements. The TEM and rTEM were found to be relatively low [121].

Tab. 5: The technical and relative technical errors of manual measurements. The minimum and maximum values are in bold.

	M_1	M_2	M_3	M_4	M_5	M_6	M_7	M_8	M_9	M_{10}
TEM (mm)	0.79	0.98	1.16	**1.55**	0.82	1.05	1.12	1.35	**0.60**	1.02
rTEM (%)	1.07	2.27	0.53	**3.51**	0.72	**0.64**	1.44	1.70	1.59	1.77
R	0.98	0.98	**0.99**	**0.94**	0.99	0.98	0.97	0.95	0.98	0.95

The distance between the automatically and manually seeded landmarks B

The largest average distance of 15.91 mm was found for landmark B6, while the smallest distance of 2.04 mm was found for landmark B18 in test set 2, see Fig. 24. There were no statistically significant differences between the repetitions of test1 and test2. The lowest value of p was 0.05 for landmark B14, while the highest value of 0.49 was found for landmark B19.

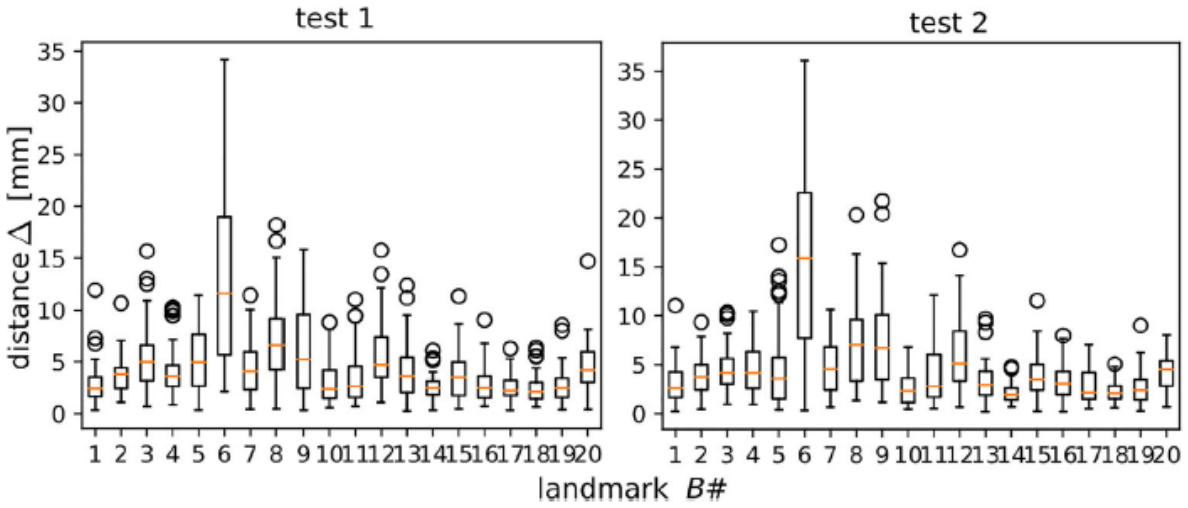

Fig. 24: A boxplot showing the distance between the automatically and manually seeded landmarks for both repetitions.

The differences between the automatically and manually computed distances M

The largest average relative difference of -4.20% was found for distance M4 in test set 2, see Fig. 25. The average lowest relative difference of 0.01% was found for distance M10 in test set 1, see Fig. 25. There were no statistically significant differences between the repetitions of test1 and test2. The lowest value of p was 0.06 for the distance M9, while the highest value of 0.49 was found for distance M2.

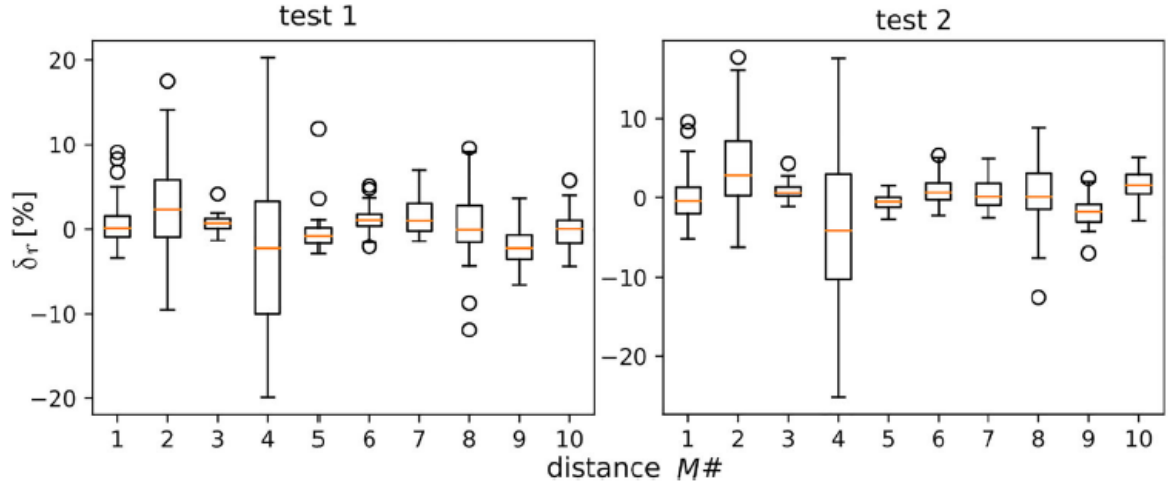

Fig. 25: A boxplot showing the relative difference between automatically and manually seeded landmarks for both repetitions.

Analysis of clouds: Back–projected landmarks

The longest distance of 10 mm was found between centroid B6 and reference landmark B6, while the shortest distance of 0.66 mm, was found between centroid B19 and reference point B19. The distances between the centroids and the reference landmarks are in Tab.6. The probability that the reference landmark falls into a given landmark cloud was high (more than 99 %) for almost all landmarks. An exception was reference landmark B9, which fell into the landmark clouds of B5/B9 with a probability of 58.5%/41.5%, see Tab. 6. In addition, the highest length of confidence for axis x, was measured for point B12 with a value of 3.62 mm, while the lowest value, 0.677 mm was found for B16. The highest length of confidence for axis y, was found for landmark B9, with a value of 13.596 mm and the lowest was for landmark B18, with a value of 1.679 mm. The highest length of confidence for axis z, was found for point B12, with a value of 34.978 mm, while the lowest was for landmark B18, with a value of 3.978 mm.

Tab. 6: A comparison of the reference landmarks and centroids that are formed by a cloud of projected landmarks that were manually defined on a template bone; Δ[mm]) is the distance between the reference landmarks and centroids; [CAx CAy CAz] with the principal of a 95% confidence axes of an individual cloud. The minimum and maximum values are in bold.

B#	Δ	CA_x	CA_y	CA_z	*B#*	Δ	CA_x	CA_y	CA_z
B_1	0.78	1.84	2.97	5.20	B_{11}	1.20	1.40	2.58	7.11
B_2	1.98	2.89	5.11	11.81	B_{12}	2.12	**3.62**	8.83	**34.97**
B_3	4.26	0.90	3.82	7.22	B_{13}	1.63	2.68	6.24	16.38
B_4	2.01	0.80	3.52	5.79	B_{14}	0.79	2.70	3.99	16.36
B_5	0.94	1.16	2.52	11.68	B_{15}	1.19	0.69	4.62	7.58
B_6	**10.00**	1.46	3.56	24.58	B_{16}	2.03	**0.67**	2.26	4.05
B_7	2.80	1.03	2.81	9.33	B_{17}	1.27	0.79	2.02	4.82
B_8	6.92	1.14	2.64	10.34	B_{18}	1.41	0.90	**1.67**	**3.97**
B_9	5.09	1.36	**13.59**	16.32	B_{19}	**0.66**	1.05	2.06	6.84
B_{10}	1.15	1.88	2.63	10.48	B_{20}	2.50	1.03	3.79	6.02

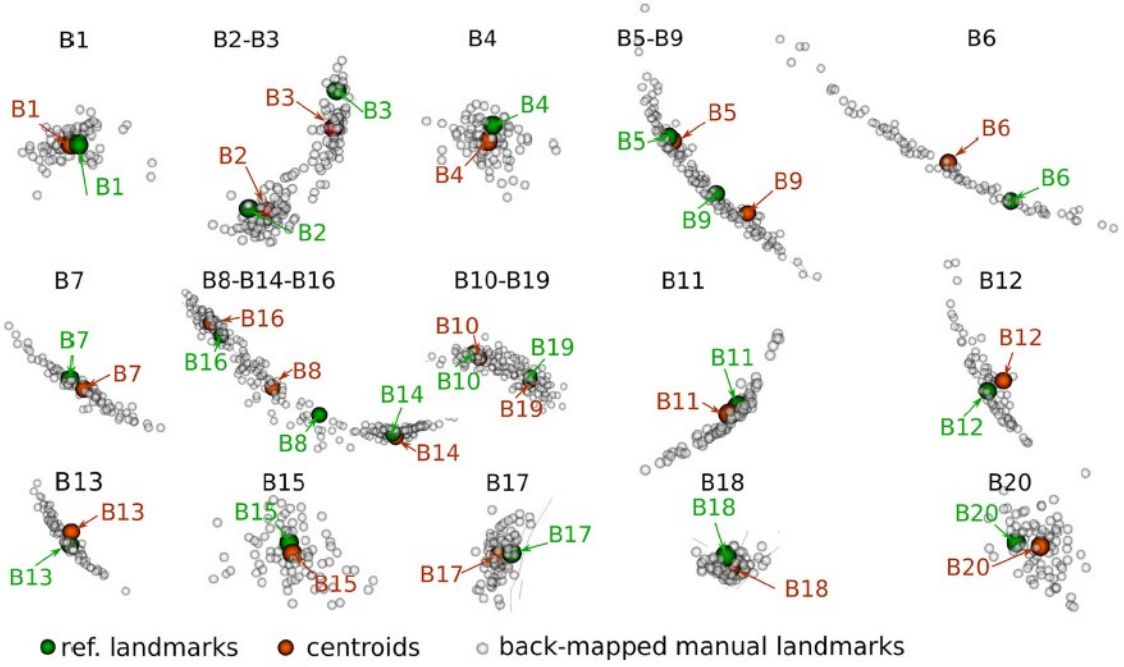

Fig. 26: Clouds of manually seeded landmarks mapped onto the template bone.

Mineral density distribution

The mean and standard deviation functions of BMD varied spatially significantly and differed for cortical and trabecular regions and for both females and males, i.e., BMD random fields were non-stationary in space.

Data analysis for females yielded the highest sample mean value of 1.246 (arcuate line, upper third), while the lowest was 0.106 (above the greater sciatic notch). The highest value of sample standard deviation (std) was 0.191 (top of the acetabular margin), while the lowest was 0.015 (deep to the auricular surface). The normality is considered to be acceptable on a significance level p 0.05, which was fulfilled for 59% of bone volume. The skewness range is 1.893 (midpart of anterior margin of the greater sciatic notch) to 7.502 (posterior part of the iliac wing). The negative values corresponding to left-skewed distributions occupy 23% of volume, while the right-skewed distributions occupy 77% of volume.

The data analysis for males yields the lowest mean value of 0.119 (deep to the auricular surface), while the highest was 1.135 (uppermost part of arcuate line). The lowest value of std was 0.016 (in between the iliac wing and iliac tuberosity), while the highest was 0.218 (top of the acetabular margin). BMD distributions can be considered being normal for 54% of volume,

while the rest contained non-normally distributed data. The skewness range is from 1.895 (inferior to ischial spine) to 6.177 (deep to the auricular surface). The left skewed distributions occupy 17% of volume, while the rest of the volume was occupied by right skewed distributions. The spatial descriptive statistics is shown in Fig. 27.

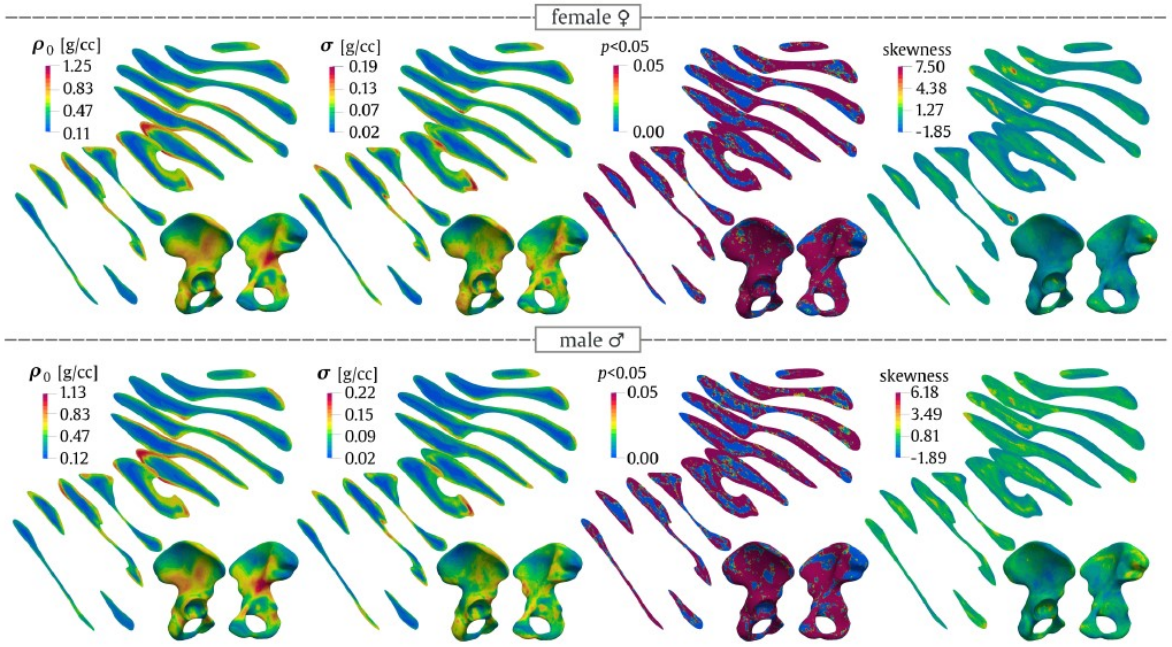

Fig. 27: Spatial statistics for BMD composing of three statistical moments for both females and males.

Age dependence of BMD/$\overline{\text{BMD}}$

The BMD slope for female varied in range from 5.163 (dorsally to the arcuate line) to 3.269 (above the greater sciatic notch) and from 5.470 (superior-posterior part of acetabular margin) to 3.625 (anterior third of iliac crest) [mg/cc/year] for females and males. The BMD is intermediately correlated with age (R^2 0.51) and (R^2 0.49) for female and male respectively. The age correlation was significant at 73% and 56% of volume on a significance level p 0.05 for female and male respectively, see Fig. 28. In 71%/61% of volume, decreased with age for both female and male. The difference in age rate estimated from CT and realizations is 5.57% and 4.71% for female and male respectively. The difference in standard error was 47% and 55% for female and male. The difference in R^2 is 21% and 50% for female and male; see Tab. 7.

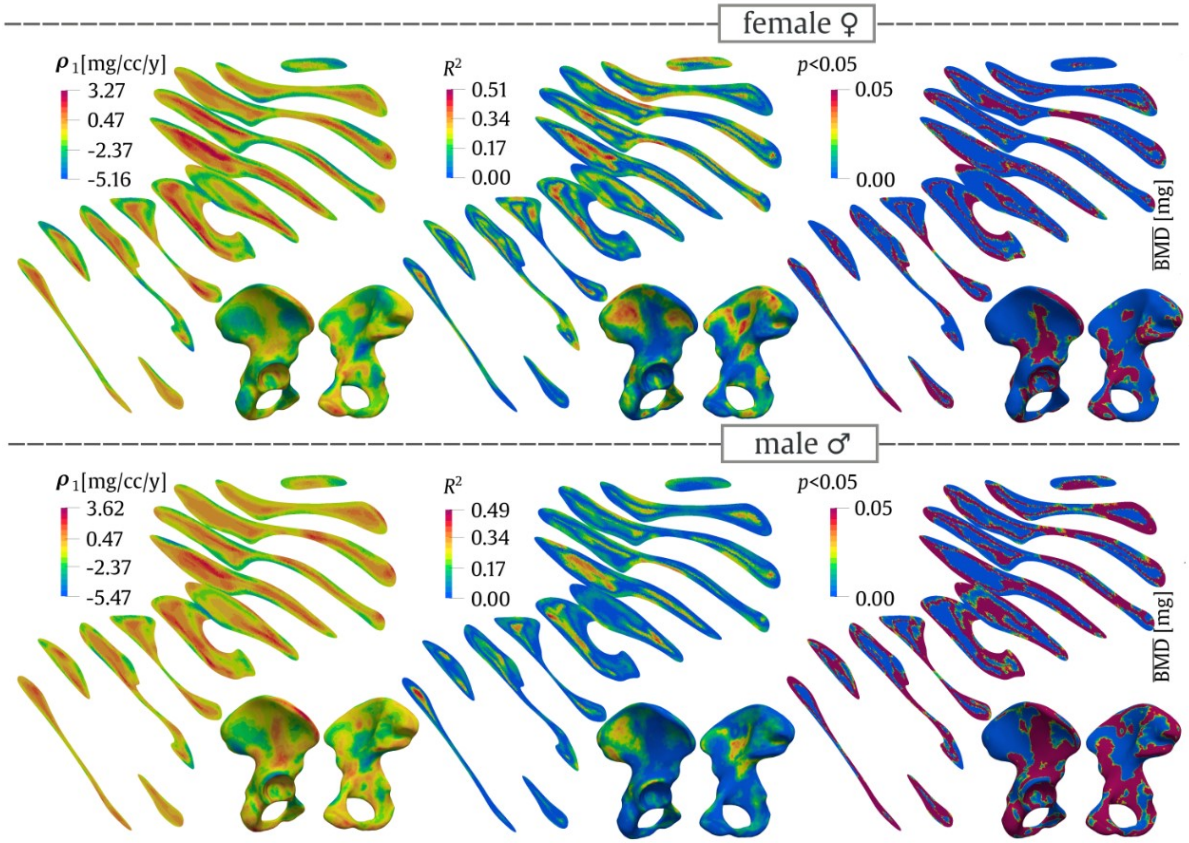

Fig. 28: Spatio-temporal evolution of BMD (ρ) and $\overline{BMD}$.

Tab. 7: An age dependence of estimated by linear regression on CT samples.

	females	males
$\overline{\text{BMD}}$ rate [mg/year]	−0.2369	−0.1168
standard error	0.060	0.075
R^2	0.140	0.028

Characteristic stiffness

Modal stiffness and eigenvectors description

The first eigenvector for model FEMP-I might represent a torsion deformation mode with maximal value located in proximity to the pubic tubercle and minimal value below the termination of the anterior gluteal line, see Fig. 29. The second eigenvector contains two significant deformation zones and is rather of bending character. Its maximum is located at the iliac crest and minimum at the central part of gluteal surface. The third eigenvector is of a rather complex bending deformation, with tree localizations at different regions of the iliac wing and ischiopubic ramus. The minimum and maximum values are localized close to the anterior superior iliac spine and the dorsal portion of the acetabular margin, respectively. The rest higher order eigenvectors quickly become much more complex and there are no significant deformation modes interpretable in terms of bending, torsion nor tension. For model FEMP-II, the maximum value for the first eigenvector is located at the anterior portion of the iliac crest. The maximum value for the second eigenvector is projected to ischial tuberosity and the maximum for the third mode represents anterior superior iliac spine. Minimal values of all foregoing modes are the points of fixation, i.e., the symphyseal and auricular surfaces of the pelvic bone. The smallest static stiffness was found with the first modal stiffness and is different for female and male. For female, the mean static stiffness is 170N/mm with standard deviation 48 N/mm for model FEMP-I and mean 97 N/mm with standard deviation 35 N/mm for model FEMP-II. For male the mean values are 267/206 N/mm with standard deviation 64/59 N/mm for FEMP-I and FEMP-II respective.

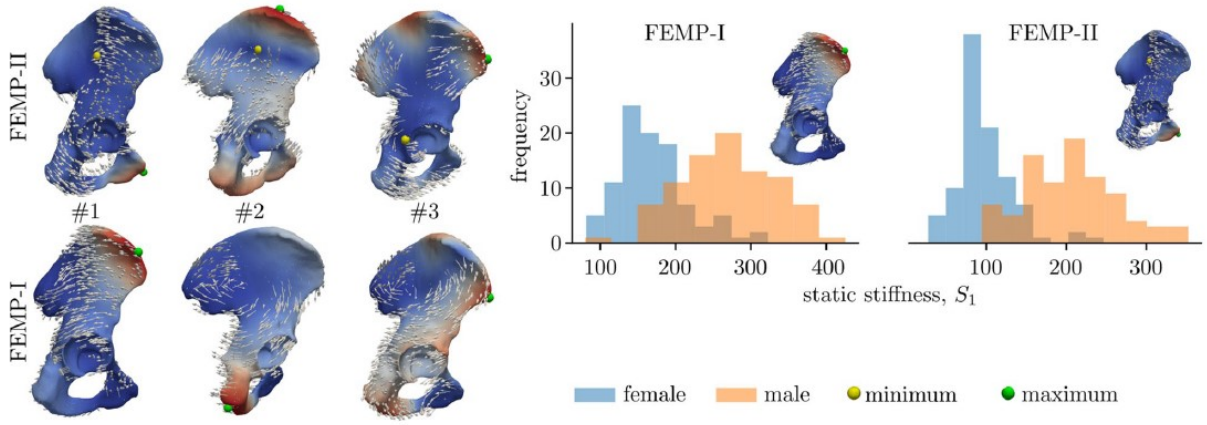

Fig. 29: The description of eigenvectors associated with three modal stiffnesses. The arrows represent the deformation fields. The scalar fields represent the magnitudes of modal vector fields. Minimum markers are not shown for fixed model FEMP-I, given the minima are localized at fixed boundary locations shown in Fig. 23. The histograms show the static stiffness [N/mm], based on the first modal stiffness and considered as the smallest static stiffness.

Comparison of stiffness metrics with anthropometric measures

Fixed boundary conditions model FEMP-I

The sex/side classifications with modal stiffness in case of fixed model FEMP- I are shown in Fig. 30. Only the first modal stiffness allows to classify sex with an accuracy 85%, while none of modal stiffnesses has the potential to classify the side. The other predefined metrics' classification ability such static stiffness S and natural frequency f are given in Tab. 8. The best sex classification accuracy of static stiffness metric S as well as natural frequency f is reached for first eigenpair. The best accuracy 0.62 for side classification was reached by static stiffness metric S for the first eigenpair. In Fig. 31 a relation between anthropometric distances and modal stiffnesses are shown. Only moderate correlations were observed for both sexes with the maximal positive value 0.49 with (CI95% [0.26, 0.67] and $p^\star = 0.0004$) for a pair 7-M9 for male.

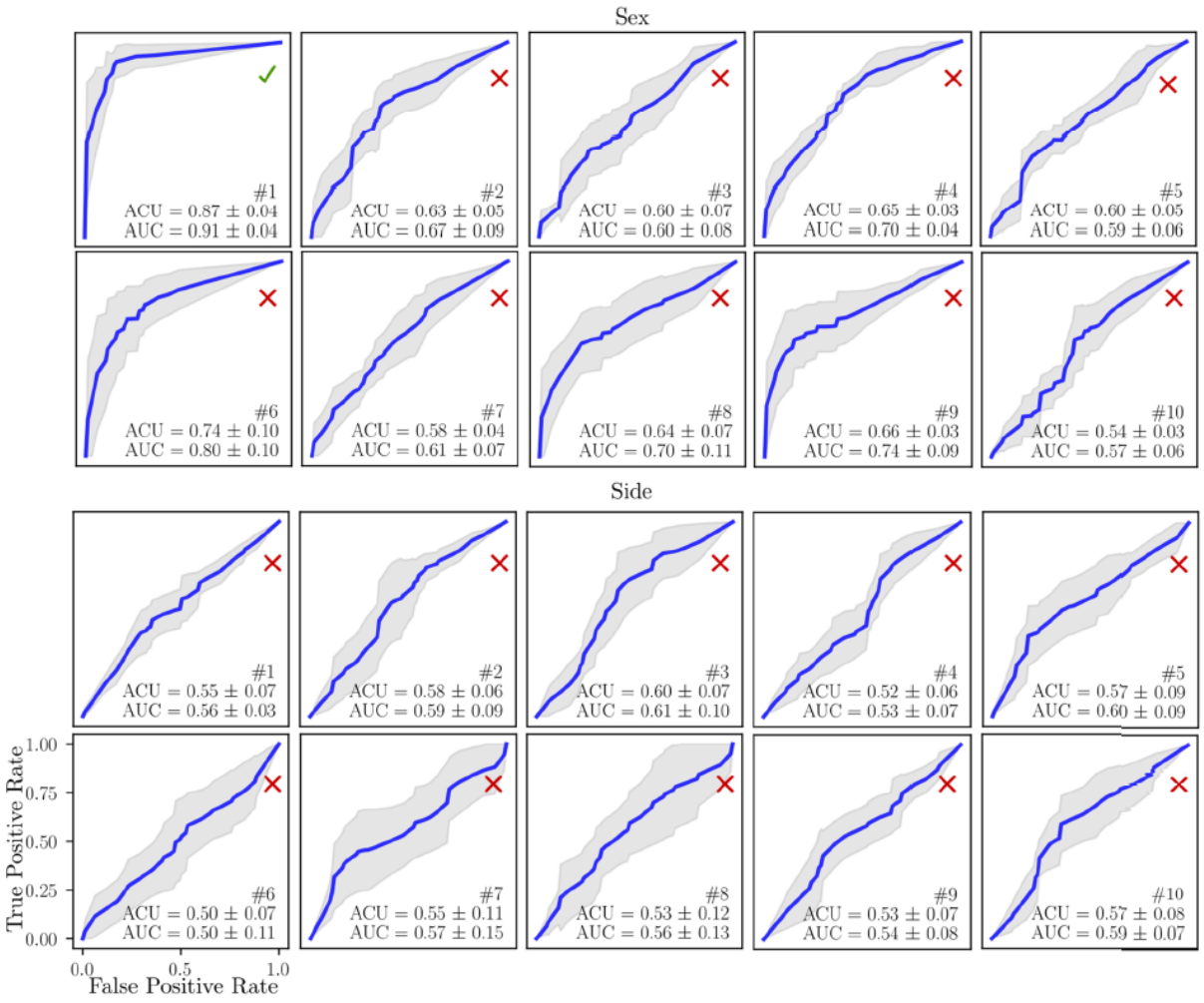

Fig. 30: The sex and side classification ability of ten modal stiffnesses s for model FEMP-I. The blue curves indicate mean values ROC, grey fill the standard deviation. The mean ACU and AUC with standard deviation is computed within cross-validation technique.

Tab. 8: SEX and SIDE classification accuracy ACU/AUC of different metrics for model FEMP-I. The CI95% are not shown due to readability, but generally are in range 0.05–0.17

Metric/eigen number #	1	2	3	4	5	6	7	8	9	10
Sex										
S	0.82/0.85	0.60/0.53	0.68/0.66	0.67/0.67	0.62/0.55	0.78/0.79	0.70/0.71	0.75/0.69	0.72/0.73	0.66/0.55
f	0.63/0.58	0.63/0.59	0.60/0.59	0.53/0.54	0.53/0.52	0.55/0.51	0.60/0.58	0.54/0.51	0.60/0.58	0.57/0.54
Side										
S	0.62/0.53	0.58/0.55	0.60/0.54	0.53/0.52	0.49/0.51	0.48/0.52	0.51/0.51	0.52/0.51	0.52/0.53	0.50/0.51
f	0.53/0.52	0.58/0.55	0.55/0.53	0.61/0.59	0.52/0.51	0.55/0.51	0.52/0.51	0.53/0.52	0.59/0.55	0.61/0.58

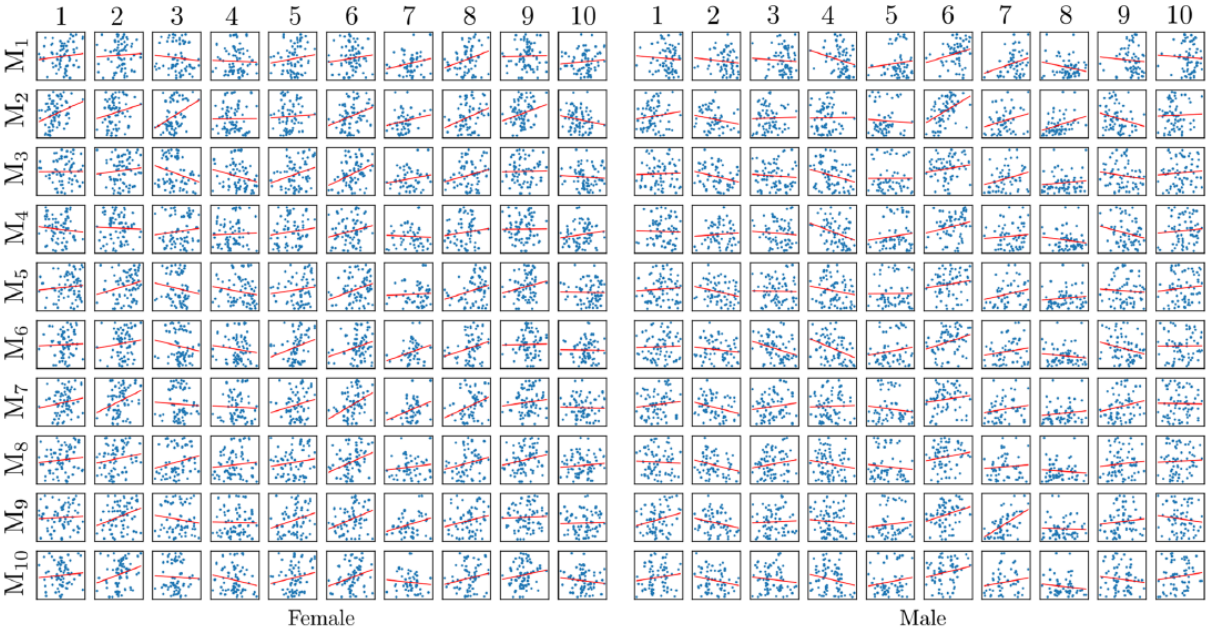

Fig. 31: Relation of anthropometric distances and modal stiffnesses computed within model FEMP-I. Blue points represent raw data, while the red curve is regression line fitted.

Free boundary conditions configuration FEMP-II

Sex/side classification accuracy of FEMP-II model is shown in Fig. 32. The modal stiffnesses s_1, s_5, s_8 were able to reach a classification accuracy higher than 85%, while none of the modes can classify side. The static stiffness S_1 is also able to predict sex with accuracy higher than 85% according to Tab. 9. A correlation between modal stiffness and anthropometric distances for model FEMP-II is shown in Fig. 33. The highest correlation of value 0.55 with CI95% [0.35, 0.70] and ($p\star = 0.00001$) was found for a pair 1-M_2 for male.

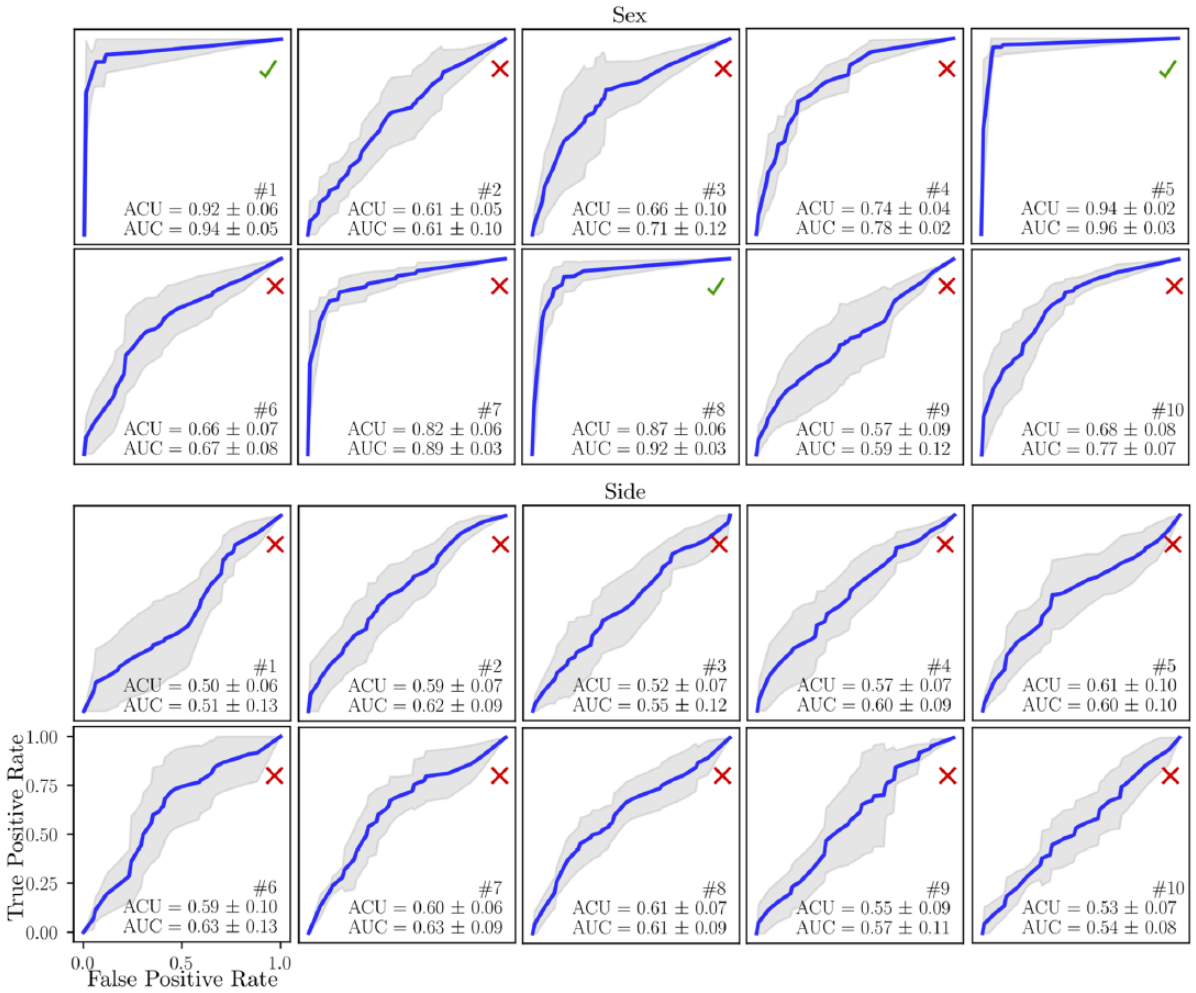

Fig. 32: The sex and side classification ability of ten modal stiffnesses for model FEMP-II. The blue curve indicates the mean ROC, while grey fill the standard deviation. The red dashed line represents a middle discrimination threshold. The mean ACU and AUC with a standard deviation is computed within cross-validation technique.

Tab. 9: SEX and SIDE classification accuracy ACU/AUC of different metrics for model FEMP-II. The CI95% are not shown due to readability but generally are in the range 0.03–0.15

Metric/eigenpair #	1	2	3	4	5	6	7	8	9	10
Sex										
S	0.88/0.89	0.65/0.63	0.64/0.65	0.78/0.79	0.75/0.74	0.84/0.81	0.66/0.67	0.84/0.84	0.62/0.65	0.66/0.55
f	0.83/0.84	0.59/0.61	0.59/0.54	0.62/0.57	0.62/0.54	0.60/0.63	0.52/0.59	0.62/0.61	0.55/0.52	0.60/0.52
Side										
S	0.59/0.61	0.57/0.55	0.52/0.59	0.55/0.54	0.55/0.61	0.59/0.55	0.50/0.55	0.51/0.54	0.44/0.52	0.55/0.58
f	0.55/0.61	0.58/0.57	0.58/0.62	0.59/0.56	0.62/0.54	0.59/0.61	0.59/0.53	0.53/0.54	0.50/0.53	0.56/0.55

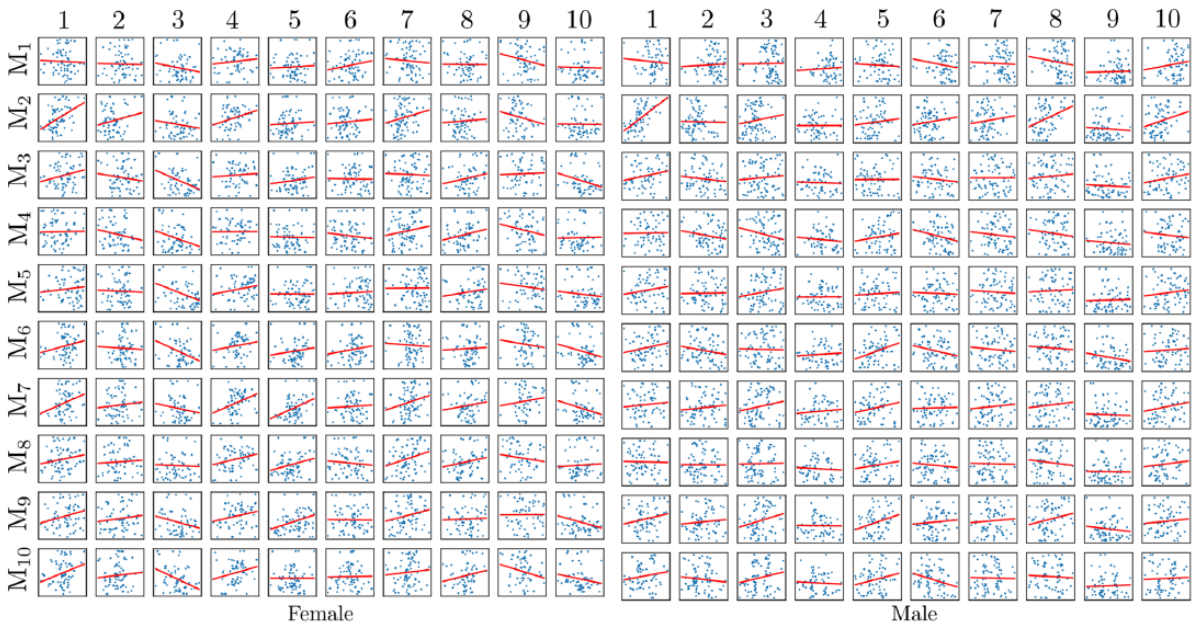

Fig. 33: Relation of anthropometric distances and modal stiffnesses computed within model FEMP-II. Blue points represent raw data, while the red curve is regression line fitted.

Classification accuracy of anthropometric distances

The sex/side classification ability of anthropometric measures M is shown in Tab. 11. The measures M2, M5 and M10 reached classification accuracy at least 85%.

Tab. 11: SEX and SIDE classification accuracy ACU/AUC of anthropometric measures M. The CI95% are not shown to improve readability but generally range within 0.03–0.18

#	M_1	M_2	M_3	M_4	M_5	M_6	M_7	M_8	M_9	M_{10}
Sex	0.59/0.55	0.85/0.84	0.82/0.83	0.70/0.65	0.93/0.92	0.60/0.55	0.79/0.78	0.63/0.65	0.71/0.72	**0.85**/0.91
Side	0.54/0.61	0.64/0.52	0.57/0.55	0.44/0.51	0.59/0.57	0.56/0.59	0.39/0.51	0.58/0.55	0.58/0.54	0.54/0.55

Discussion

Registration algorithm

According to the results, the automatic measurement method seemed to be accurate and usable for further computation. Most of the average distances between the manually and automatically seeded landmarks were below 5 mm. Average distances above 5 mm were found for B6, B8 and B9. Landmarks B6 is defined from the distance M3 (see the definition in Fig. 17), which means it is not directly dependent on bone geometry. Therefore, it can be located almost anywhere in the middle third of the iliac crest. The landmark B8 should lie on a site, where the axis, inserted to the posterior inferior iliac spine, is just perpendicular to the anterior border of the greater sciatic notch (Fig. 17). In this case, the operator's result was superior to that of the computer's result. This can be interpreted as an algorithm employing a similarity metric, which does not take into account any additional geometrical constraints.

The accuracy of automatic landmark seeding depends on the proper seeding of reference landmarks on template bone by an operator. Moreover, the identification of fine anatomical features on template bone can be more difficult because they can be partially smoothed out due to the method used for template bone construction [109]. This situation is typical for landmark B9, which relies on the location of the anteroinferior termination of the ischial tuberosity.

In presented study, the TEM, rTEM and R values were relatively low and the mean differences between the automatic and manually measured distances were within millimetres which is comparable to similar publications [45, 110, 150, 151].

The algorithm calculates a continuous spatial transformation, which means that any point on a bone sample has a unique counterpart on the template bone. In other words, we can potentially define landmarks anywhere on the bone [152]. This transformation makes it possible to interpret the difference in shapes in the deformation metric, which is considered as being intuitive and natural. This capability of the registration algorithm allows for shape analysis, which is usually performed by using the Principal Component Analysis (PCA) [153-155]. Unlike the PCA, the algorithm does not require a correlation matrix, which can be large and dense (in the case of CT data).

In our study, the algorithm took 10 minutes per sample (compiled on a Linux Ubuntu 18.04 LTS platform, GCC 7.4.0, Intel i7 (8 cores) CPU 2.10GHz, 16Gb RAM). This could be seen as

a relatively long time, but the pipeline of registration is fully automated and stable, which is very convenient for the end–users. Once the registration step is done, the computing of landmark locations and distances over the whole dataset takes only a few seconds.

Mineral density distribution

The understanding of bone density is of paramount importance to biomechanics in relation to the understanding of bone mechanobiology, and it should be properly incorporated into computational models.

We assume that spatial fluctuation of BMD reflects the response of bones to external loading, which causes the bone to deform in a complex manner (bending + torsion + tension/compression). The load from the trunk is directed through the sacroiliac (SI) joint to the acetabulum and the femoral head while standing or through the ischial tuberosity while sitting. Simultaneously, more than thirty muscles and several ligaments are attached to the pelvis, loading the bone with their tension in various directions.

Increased BMD in the greater sciatic notch area, the upper part of the arcuate line, and the body of ischium seems to correspond well to weight-bearing load. The relatively low standard deviation in this area could indicate that the weight-bearing load can be considered as a common base load in the population. Even though the force generated by related muscles can be significant, just slight density elevations following the margins of large muscles' attachments (iliacus, gluteus medius) or isolated peaks for muscles with smaller insertion sites such as the rectus femoris were found. However, an interesting similarity was observed between the high standard deviations and the sites of possible apophyseal avulsions. This could indicate an increased individual localized stress induced by inserted muscles or ligament insertions (anterior superior iliac spine – rectus femoris; anterior superior iliac spine – sartorius; ischial tuberosity – hamstrings; iliac crest – abdominal wall muscles; ischial spine – sacrospinous ligament and coccygeus muscle). The increased standard deviation at these sites could reflect variations in physical activity and other unknown effects. Other sites with increased standard deviation, i.e., the superior acetabulum and anterior margin of the auricular surface, are typical of osteophytes.

Most publications provide information about a gradual reduction in bone mineral density with increasing age [156, 157]. However, it remains unclear whether this is a uniform process for all

skeletal sites or whether there might be some region dependence [156-158]. Moreover, due to the variable surface-volume ratio and related bone turnover, local differences between cortical and cancellous bone should be expected [159-161]. The age changes in cortical BMD can be described by cortical thinning, higher porosity, pore diameter and osteon density [150, 162, 163]. Cancellous bone is affected by trabecular loss. In males, this is mostly in the form of trabecular thinning, while in females, trabecular disconnection occurs [36, 164-166]. There is, however, little known about the spatial and age distribution of BMD in human innominate bone, as the majority of studies focus on long bone, vertebral or hip examinations.

The presented results showed general age-dependent cortical BMD decline and, surprisingly, local mild trabecular BMD elevation. The reason is unclear, but it could be connected to higher trabecular mineralization patterns, which correlate with age, as documented in [167]. We found that female BMD is more sensitive to age. The BMD decreases with age in more than 68%/58% of the volume of bone for females/males. The BMD decreases faster for females (51% faster than for males).

Characteristic stiffness

The mechanical properties of bone are given by the geometry and the intrinsic structure together with material properties. This mix of unique bone properties is highly individual and hence its precise capturing seems a paramount of current in silico biomedical engineering. This study provides a unique signature that captures all mentioned bone properties within a set of so-called eigenpairs. Those eigenpairs are derived from a truncated spectral decomposition of bone stiffness and mass, represented by algebraic matrices produced by a finite element discretization. Using all eigenpairs computed, one could get the full information on bone stiffness (as the stiffness matrix is fully recovered). Practically, only a few eigenpairs are required to capture most of the information about stiffness.

In this study, ten modal stiffnesses close to zero were presenting 94% of the bone static stiffness. The smallest eigenvalue corresponded to the smallest natural frequency f. Nevertheless, modal stiffnesses do not necessarily follow the same order as natural frequencies since they are rescaled with respect to the power of the eigenvectors amplitude. Interestingly, the modal stiffness corresponding to a first eigenvalue was always the smallest one in our analyses presented here. The corresponding eigenvector maximum magnitude can point to a location and direction of the smallest static stiffness, which can be considered as the most interesting and

important. And last, deeper analysis is required to analyse nor explore relations between modal stiffness/smallest static stiffness and important mechanical properties such bone strength, density and anisotropy.

Interpretation of eigenvectors with respect to static stiffness

The smallest static stiffness can be approximated by modal stiffness if there exist a load and kinematic boundary conditions that produce a deformation of bone, which is similar to an eigenvector. This relation was already demonstrated in [19] and in [168]. This relation can also be explained by a so-called modal reduction technique. The quantities of interest are projected on to a reduced space spanned by a few eigen vectors to decrease computational complexity while maintaining the model as accurate as possible.

Stiffness - sex prediction

Eigen metrics predict sex, although they are only weakly correlated with gold-standard anthropometric measures. This fact corresponded to an origin of eigen metrics, which can be seen as spectral components of bone shape information. In fact, the eigen metrics include the topological and intrinsic characteristics of bone apart from geometry information, which cannot be simply captured by the gold-standard method. Further, we include a side classification as a complementary test to validate tested metrics. As it was expected, no significant side difference was observed from classification tests with tested metrics. The sex classification accuracy of defined metrics compared to gold-standard seems considerable for individual modes and depends on the boundary conditions defined. Nevertheless, including computed modes simultaneously into the classification algorithm, the final accuracy is excellent (ACC/ACU 98.1%/97.1% 0.01%). Moreover, the sex classification accuracy of gold-standard anthropometric points was also comparably high (ACC/ACU 93.3%/92.1% ± 0.01%).

Boundary conditions affect metrics sensitivity

We demonstrated that natural frequencies, modal and static stiffness can be computed for a configuration without boundary conditions defined (FEMP-II). This presents a serious advantage, given the proper modelling of often complicated anatomical boundary conditions is difficult and introduces additional uncertainty into the model. Moreover, our results showed that our metrics computed on the model FEMP- II have better description and classification accuracy than a constrained model FEMP-I. In a sex classification, the FEMP-II metrics contain four sensitive eigen pairs (Fig. 32), while FEMP-I metrics only one (Fig. 30). Moreover, FEMP-II model can be well-validated by an experimental modal analysis with good results [169]. Apart

from these advantages, the drawback of FEMP-II model is the difficulty in interpreting the static stiffness as it is no well posed static problem. One interpretation could be in an analogy with an alternative model with suitable boundary conditions defined that produces a deformation corresponding to free conditions eigen vector.

Relation to modal analysis

The static stiffness is related to modal stiffness in following way. The static stiffness is computed as an inverse sum of modal compliances. The modal dynamics of bone were analysed to assess the natural frequencies and associated vibration modes in line with previous experiments [170, 171] and as a reliable experimental protocol to calibrate computational models [169, 172]. We also computed the natural frequencies as a metric and compared it with eigen stiffness metrics. Further, our computed natural frequencies are consistent with those in literature [169, 170].

Study limitations

We are aware of some study limitations. Contrary to dry bone measurements, thin bone projections and bony plates could be lost in the CT data due to an insufficient resolution and must be carefully reconstructed to obtain the same bone topology across the entire dataset. Furthermore, any articular surfaces that may be affected by enthesophytes, which is common in the elderly, may reduce the accuracy of automatic landmark placement [47]. A lack of more observers in the Registration algorithm section should raise some caution regarding the interpretation of the intraobserver errors. However, a similar setup of the TEM method is proposed in [151, 173, 174].

The multi-scale nature of bone could not be considered in detail in the present study. The routine CT data that may not have sufficient resolution to capture trabecular architecture or the cortical bone shell properly. This issue complicates the estimation of local variations and anisotropy of the trabecular network as well as the composite structure of the cortical shell. Clinical routine CT is known to distort cortical density and thickness [175, 176], thereby exceeding a 100%-error in the sub millimetre structure of cortical bone. The effect of insufficient CT resolution may be seen in the central part of the iliac wing, where the thickness of the trabecular bone layers is minimized and prone to partial volume effects. In some cases, even a fenestration may be present at this location [177]. It is not obvious how the statistical moments and correlation

structure are affected, and a careful analysis should be performed with the help of cortical thickness and the density estimation algorithm introduced in [178], dedicated for clinical CT. The CT data were calibrated internally, without a phantom, using surrounding tissues [136]. Recent studies have shown that internal calibration can be a full alternative to the gold phantom standard [136, 179, 180]. However, various factors that influence internal calibration remain up for debate and caution is in order with regard to achieving accuracy and robustness. Fortunately, the correlation structure of the mineral density is invariant with respect to any linear calibration. However, the mean and variance of the mineral density can be biased by insufficient calibration. In an extreme case, the calibration curve can be considered a source of uncertainty in the mineral density model.

The boundary conditions in this study roughly mimic physiological conditions and their precise definition (potentially including the ligaments and other soft tissues) must be included to extend the usability of our proposed metrics.

We have obtained that the smallest modal stiffness corresponds to the smallest static stiffness. Nevertheless, this observation is rather heuristic as we could not provide a suitable proof that the first eigen vector always points to a smallest stiffness. On the other hand, this limitation does not decrease a potential of proposed metric for studying bone mechanics, because the smallest stiffness can be still found by careful analysing of stiffness spectra or optimization based approach proposed in [19].

Method interpretation and validation

With the development of the registration algorithm and defying the original bone stiffness metric, the work's intended aim was achieved. However, the full explanation of its advantages and further applicability surpasses the limits of this thesis. The following text should be considered as an inserted “study in the study” to present and discuss the method’s potential.

Pelvic bone – method interpretation

This thesis defined the modes, in which the pelvic bone presents the smallest stiffnesses. As we consider the results correct and verified, the interpretation remains complicated. The biggest question is whether the common physiological loads can explain the smallest stiffness modes on the bone.

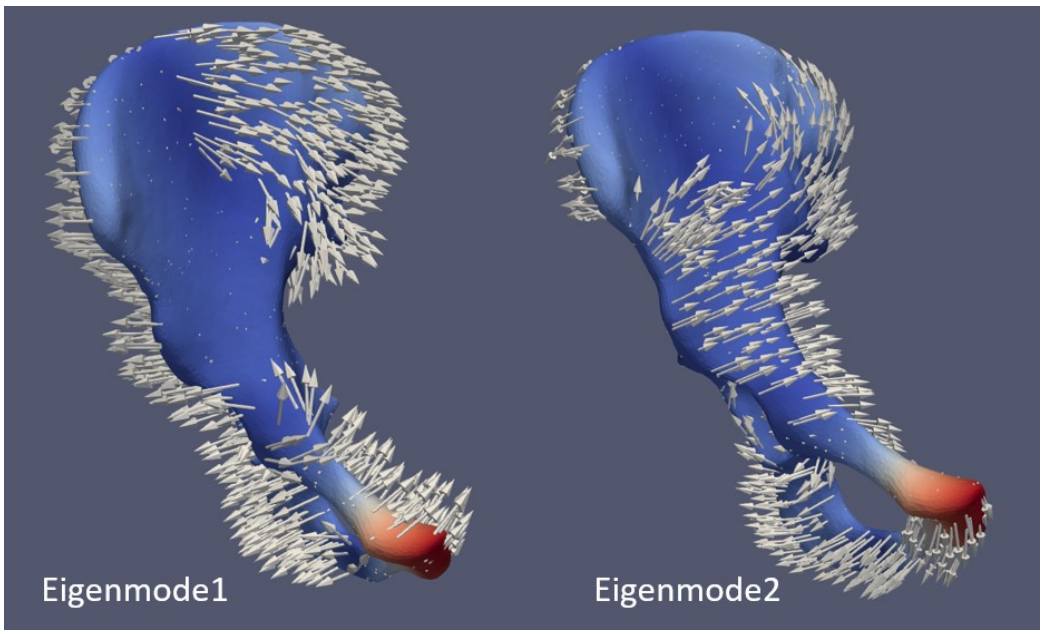

Fig. 32: The eigenvectors associated with the first two modal stiffnesses. The arrows represent the deformation fields, while the scalar fields represent the magnitudes of modal vector fields.

Figure 32 shows the first two modal stiffnesses of the FEMP-II model. According to our computations, these are the modes of absolutely smallest stiffness (largest compliance) when no boundary conditions are applied. Colours represent the displacement and its value; the arrows represent the direction. In other words, if we load the bone in the direction of the pictured glyphs, the pelvic bone will behave according to the model situation. The commentary could

be as follows: Here (mode1), the bone is least stiff in the torsion. In real conditions, dorsolateral part of iliac wing and the area of auricular surface could be pushed forward by the gravity through the tension of the iliolumbar and sacroiliac ligaments. The anterolateral part of iliac wing shifts dorsally. The explanation could be the pressure of abdominal organs and forces caused by the gluteal muscles. The acetabular margin and symphyseal area deformations are probably related to load transmission to the femur and the other half of the pelvic girdle. The sciatic tuberosity's lateral inclination can result from hamstring forces and/or sitting. Eigenmode2 picture presents the mode of second smallest stiffness; it contains two significant deformation zones and is rather of bending character, with evident differences at the pubic bone and mediodorsal part of iliac wing. The third (not pictured) eigenmode is even more complicated and of rather complex bending deformation.

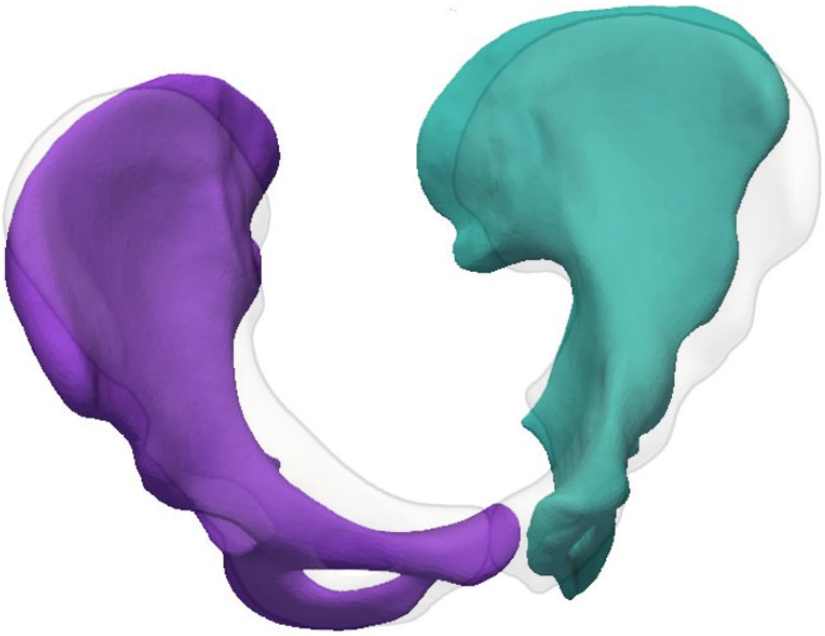

Fig. 33: Deformation of the pelvic bone model in first (purple) and second (green) modal stiffness.

The FEM method is capable of a structure mechanical load, which allows the visual representation of structural displacements under a specific load of chosen mode. In other words, the overall shape of pelvic bone is changed according to the previously computed first and second mode. Interestingly, the eigenmode1 and eigenmode2 correspond to each other (Fig.

33), where different torsion of one complete the second. Could there be a connection to specific load modes in unequal stress distribution on the pelvic bones – i.e., can it explain the side load variability, for example during the gait cycle? Look likely, but up to now we cannot provide the evidence.

At this point, this interpretation has obviously many flaws, not counting just a brief survey of ligament fixations and muscle impact. Firstly, as the solitary bone is described, we lose its connection to the pelvic girdle – which will definitely work as a unit. Secondly, the loads and pressures are not stationary. The body position, movement pattern, and personal habits in general strongly influence bone behaviour. And thirdly, contrary to our assumption, the stiffness modes should not necessarily follow the physiological patterns.

However, our proposed method is transferable to other objects and once tested on irregular pelvic bones, it could be applied to all bones in a human body, regardless of their complexity/simplicity. For the reasons discussed above, we tried to validate the connection between smallest stiffness modes and physiologically based loads on a bone simpler in geometrical terms – the femur.

Femur – method validation

It is well-known that long bones are the least stiff in pressure, which is reflected in bending mode. However, the direction and magnitude of this deflection depend on the direction and magnitude of the applied force, which is set artificially. The general shape of the femur should counter the main incoming forces with respect to the weight/function ratio. In our opinion, a slightly curved femoral shaft contributes significantly to the material savings, as part of the pressure is transformed into bending. Therefore, stiffness could be a good indicator of bone function. The idea was to simulate the difference in bending modes in the main parts of the gait cycle (stance phase I +II) and compare it with the smallest stiffness distribution acquired by our method. In theory, the modes capable of maximum energy storage (smallest stiffnesses) should correspond to the main loading modes.

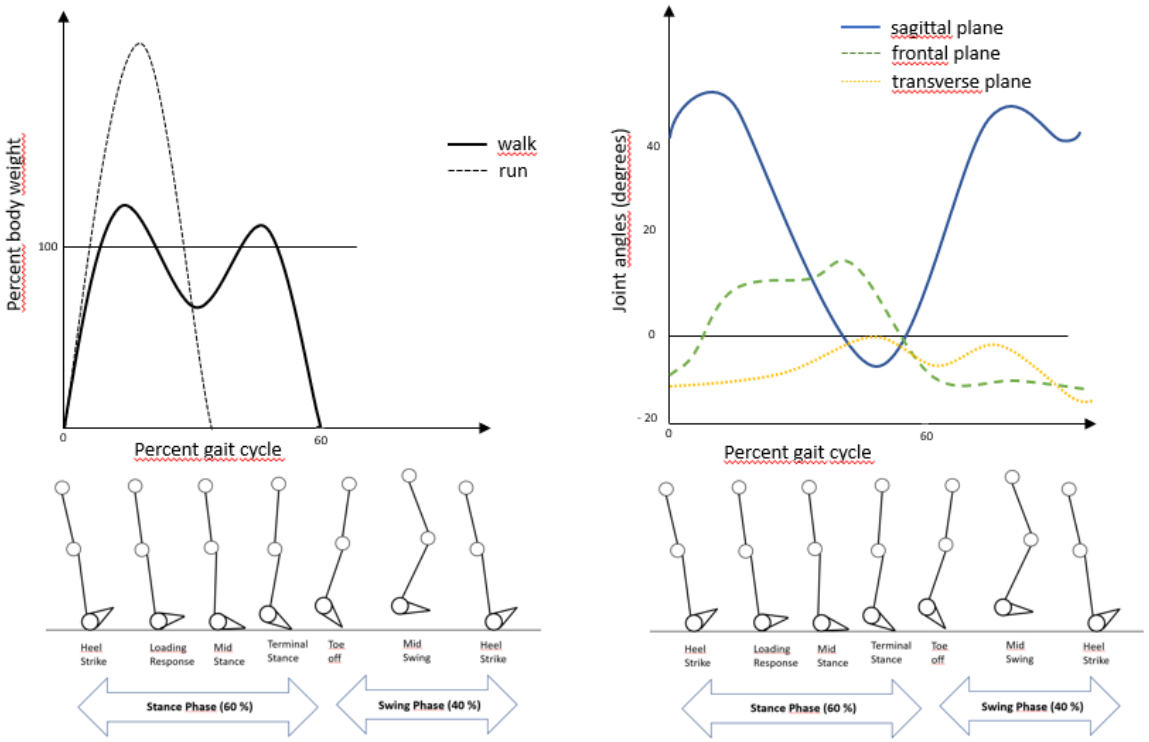

Fig. 34: Distribution of the body weight (A) and hip joint angle value (B) during the separate phases of gait cycle. Adopted from Sangeux et al. [181].

The femur geometry was obtained from a CT scan with a semi-automatic segmentation algorithm (MITK-GEM), based on a defined Hounsfield (HU) field and subsequent manual correction. The bone morphology and mineral content were incorporated into the 3D model. According to the methods described previously, the two smallest stiffnesses were acquired using the spectral decomposition of the stiffness matrix. Structural displacements (warping) were simulated with the ParaView application [118].

The same virtual model was transferred to the FebioStudio Software Suite [182], which is a finite element application commonly used in biomechanical research. Young's modulus E=10 GPa and the Poisson's ratio is 0.3 here define the linear material model of bone. Two simulations of the gait cycle were performed, early midstance and terminal stance. According to [183], there should be an absolutely largest hip join load in these two phases. For early midstance, the load was applied to the anterolateral surface of femoral head and the boundary was set to the posterior surface of medial condyle. The anatomical position of femur was set up as a mild flexion and slight external rotation (Fig. 34). The main force comes from the body weight and

points towards the midfoot. For terminal stance phase, the load was applied to the posteromedial surface of the femoral head. The bone was virtually fixed in the anterior third of lateral condyle, in its mild extension and internal rotation. The load is directed from the femoral head latero-dorso-caudally, again towards the imaginary floor contact point.

Preliminary results

For eigenmode1, the main stress distribution is presented on the lateral side of the femoral shaft and medially to linea aspera. I have found similar stress distribution in a model of midstance. The stress distribution for eigenmode2 is visually very similar to the model of terminal stance, with the highest values on the medial surface of the femoral shaft and laterally to the linea aspera (Fig. 35).

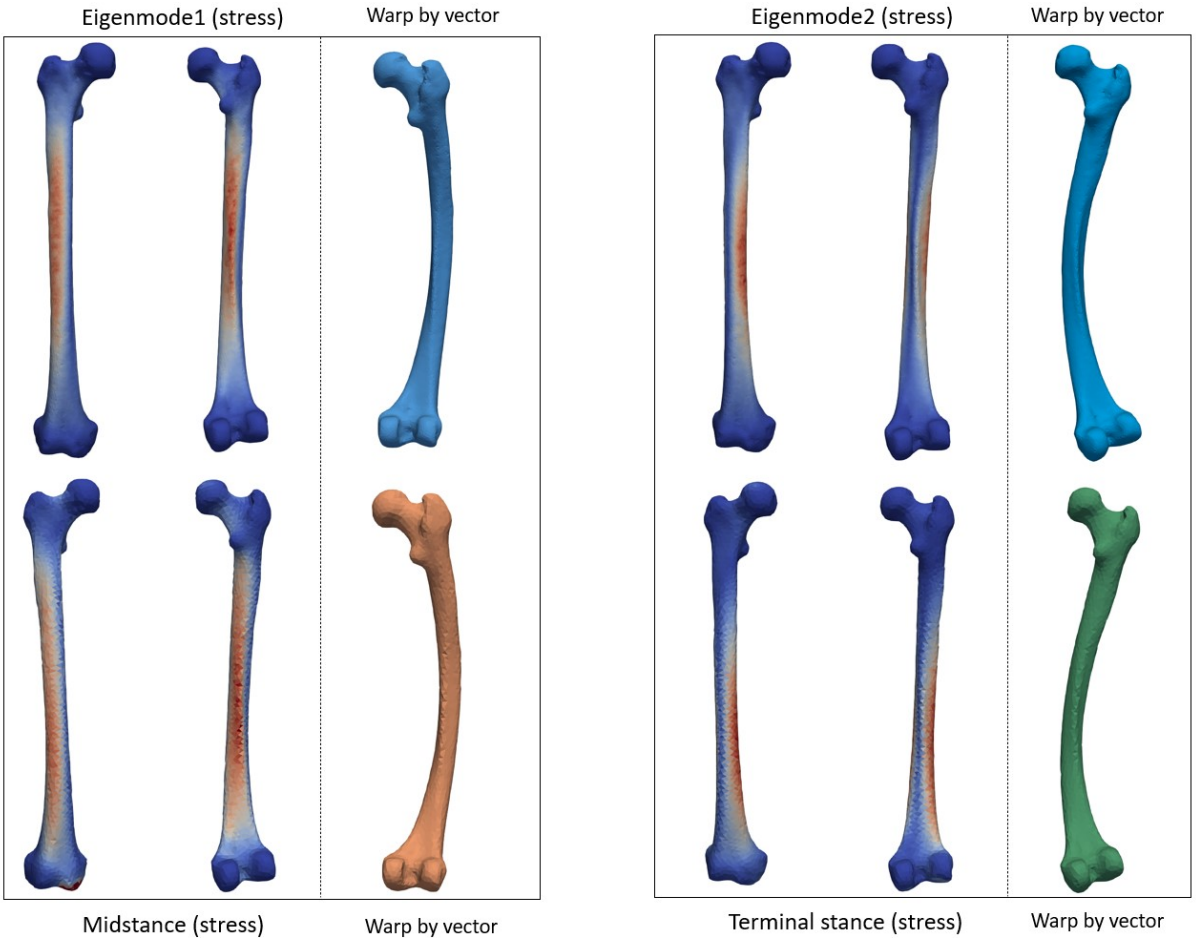

Fig. 35: Stress distribution in eigenmode1 and eigenmode2 n with associated deformation modes. The warped models do not represent real bone response under pre-defined load; they visually express displacement amplification according to the vector size and direction.

Both eigenmodes warped by a vector were compared to simulated model deformation in selected gait cycle phases. The results were similar to stress distribution analysis. Eigenmode1 corresponded well to the midstance and eigenmode2 to the terminal stance phase.

Contrary to the pelvic bone geometry, human femur is relatively simple. It behaves like a tubular structure, transferring the body forces towards the ground and works as a lever for muscles of locomotion. As the bone does not change much during human evolution, I assumed that the shape itself (not the internal structure) could be interpreted by the bipedalism requirements, more than resistance to various sudden impacts or individual habitual loading. We compared the outcome of spectral analysis to the behaviour of the bone in two phases of the gait cycle. The results were similar, both for the stress distribution and displacement.

The precise analysis is a topic for further studies. However, a close connection between stress distribution in the computed eigenmodes and single stance phases of the gait cycle was observed. The spectral analysis results depend purely on geometrical and material properties, not the force direction and value. The ability to „pair“ structure's smallest stiffnesses to the physiological loading could be a promising step in the understanding of mechanical behaviour of bones in different anatomical and physiological conditions.

Final thoughts

The following statements are not directly implied by previous research as they were not tested yet. However, our work gave rise to some interesting hypotheses, which will be discussed here and validated in the next studies.

1. The spatial modulus of elasticity (closely related to HU and BMD) could possibly reflect the areas where the bone counters the largest stress. This increase could result from a functional requirement and a stress-based slower metabolic activity of the bone cells, where the cell's metabolism is compromised by incoming pressure. Ideally, the bone should not be forced to bending modes at these specific sites of higher mineralization, where, due to lack of elasticity, it is more prone to fractures. Finding the connection between these sites, main modal stiffnesses and ab/normal physiological loading may localize any potential "critical point". This knowledge could contribute significantly to prosthesis design, accelerate post-operative rehabilitations, and even explain some typical fracture sites.

2. According to our previous work, the overall shape of the bone changes is the main component of bone stiffness estimation, completed by the mineral content. One can hypothesize that a balanced shape-density relationship working well for younger people will be strongly affected by different mineralization in elderly/osteoporotic patients. As the bone shape changes only minimally with age, contrary to the mineral content, the altered material properties could make the bone more prone to fractures. Especially at the sites, which were formerly flexible enough to absorb the load. It is possible to map these patterns and even simulate the density changes in-silico.
3. Each bone has its own specific function, and its material and structural properties are directly connected to this purpose. By mapping the so-called lowest stiffnesses, one can estimate what functional requirements were placed on the bone (load-bearing x non-load-bearing x cover bone), which can be helpful in a functional description of extinct species remains.
4. The characteristic stiffnesses are sexually dimorphic. This statement could be used for sex estimation in either historical findings or forensic cases.

Conclusions

The study utilized the potential of the diffeomorphic shape registration in the automatization of landmark seeding, making data–gathering and its evaluation easier in further process. I created and tested a set of virtual human pelvic bones and defined anatomical landmarks, which were seeded by a proposed registration algorithm. The registration algorithm makes it possible to achieve a high degree of automation with the potential to reduce operator errors in the seeding of anthropological landmarks. This represents a promising step forward in an effective definition of the anthropological measures of the human skeleton and helped us immensely to pair the internal properties of a single bone (stiffness, BMD) with the external properties (bone morphology).

Understanding distribution and uncertainties in bone density is of paramount importance to biomechanics in relation to bone mechanobiology, and it should be appropriately incorporated into computational models. We defined the temporal and spatial distribution of the bone mineral density in the individual pelvic bones as well as its population variability. Observed differences indicate that the temporospatial density field is not constant, and further modelling is incomplete without this information.

Structural stiffness plays an important role in bone morphology. The stiffness analysis requires precise experiments and computational models that can be difficult or time–consuming to procure. A new metric for the quantitative and qualitative evaluation of bone stiffness is introduced. It is based on the spectral decomposition of stiffness matrix computed with finite element method. The here proposed metric is defined as an amplitude rescaled eigenvalues of stiffness matrix. The metric contains unique information on the principal stiffness of bone and reflects both bone shape and material properties. The metric was compared with anthropometrical measures and was tested for sex sensitivity on pelvis bone, showing promising results.

Finally, the smallest stiffness of pelvis was computed under a certain loading condition and analysed with respect to sex and direction. The metric again complements anthropometrical measures with similar accuracy to anthropological gold-standard methods. Further, it provides unique information about the smallest bone stiffness independent from the loading configuration. This specific property can be easily computed by state-of-the-art subject specified finite element algorithms and applied on every skeletal element in human body.

Bibliography

1. Wallach, S., et al., *The bone "quality" problem*. 1992, Springer.
2. Bouxsein, M.L., *Bone quality: where do we go from here?* Osteoporosis international, 2003. **14**(5): p. 118-127.
3. Chesnut 3rd, C. and C. Rosen, *Perspective: Reconsidering the effects of antiresorptive therapies in reducing osteoporotic fracture.* Journal of Bone and Mineral Research, 2001. **16**(12): p. 2163-2172.
4. Watts, N.B., *Bone quality: getting closer to a definition.* Journal of Bone and Mineral Research, 2002. **17**(7): p. 1148-1150.
5. Cole, J.H. and M.C. van der Meulen, *Whole bone mechanics and bone quality.* Clinical Orthopaedics and Related Research®, 2011. **469**(8): p. 2139-2149.
6. Laing, A.C. and S.N. Robinovitch, *Characterizing the effective stiffness of the pelvis during sideways falls on the hip.* Journal of biomechanics, 2010. **43**(10): p. 1898-1904.
7. Ward, J., et al., *Stiffness and strength of bone in osteoporotic patients treated with varying durations of oral bisphosphonates.* Osteoporosis International, 2016. **27**(9): p. 2681-2688.
8. Zhu, T.Y., et al., *Value of measuring bone microarchitecture in fracture discrimination in older women with recent hip fracture: a case-control study with HR-pQCT.* Scientific reports, 2016. **6**(1): p. 1-7.
9. Rezaei, A., et al., *Are DXA/aBMD and QCT/FEA stiffness and strength estimates sensitive to sex and age?* Annals of biomedical engineering, 2017. **45**(12): p. 2847-2856.
10. Patton, D.M., et al., *The relationship between whole bone stiffness and strength is age and sex dependent.* Journal of biomechanics, 2019. **83**: p. 125-133.
11. Levine, I.C., S. Bhan, and A.C. Laing, *The effects of body mass index and sex on impact force and effective pelvic stiffness during simulated lateral falls.* Clinical biomechanics, 2013. **28**(9-10): p. 1026-1033.
12. Stauber, M., et al., *Importance of individual rods and plates in the assessment of bone quality and their contribution to bone stiffness.* Journal of Bone and Mineral Research, 2006. **21**(4): p. 586-595.
13. Fyhrie, D.P. and D. Vashishth, *Bone stiffness predicts strength similarly for human vertebral cancellous bone in compression and for cortical bone in tension.* Bone, 2000. **26**(2): p. 169-173.
14. Baumgart, F., *Stiffness-an unknown world of mechanical science?* Injury-International Journal for the Care of the Injured, 2000. **31**(2): p. 14-23.
15. Viceconti, M. and P. Hunter, *The virtual physiological human: ten years after.* Annual review of biomedical engineering, 2016. **18**: p. 103-123.
16. Viceconti, M., A. Henney, and E. Morley-Fletcher, *In silico clinical trials: how computer simulation will transform the biomedical industry.* International Journal of Clinical Trials, 2016. **3**(2): p. 37-46.
17. Kuchar, M., et al., *Shape morphing technique can accurately predict pelvic bone landmarks.* International Journal of Legal Medicine, 2021. **135**(4): p. 1617-1626.
18. Henyš, P., et al., *Bone mineral density modeling via random field: normality, stationarity, sex and age dependence.* Computer Methods and Programs in Biomedicine, 2021: p. 106353.
19. Henyš, P., et al., *Localising the smallest stiffness and its direction of a homogeneous structure by spectral and optimisation approaches.* Engineering Structures, 2021. **232**: p. 111842.
20. Henyš, P., et al., *Mechanical metric for skeletal biomechanics derived from spectral analysis of stiffness matrix.* Scientific Reports, 2021. **11**.
21. Malizos, K.N. and L.K. Papatheodorou, *The healing potential of the periosteum: molecular aspects.* Injury, 2005. **36**(3): p. S13-S19.

22. Cristy, M., *Active bone marrow distribution as a function of age in humans.* Physics in Medicine & Biology, 1981. **26**(3): p. 389.
23. Simkin, P.A., *Marrow fat may distribute the energy of impact loading throughout subchondral bone.* Rheumatology, 2018. **57**(3): p. 414-418.
24. Burr, D.B. and M.R. Allen, *Basic and applied bone biology*. 2019: Academic Press.
25. Dauber, W., S. Kramer, and G. Spitzer, *Pocket atlas of human anatomy: founded by Heinz Feneis*. 2007: Thieme.
26. Carter, D.R. and W.C. Hayes, *Compact bone fatigue damage: a microscopic examination.* Clinical orthopaedics and related research, 1977(127): p. 265-274.
27. Nordin, M. and V.H. Frankel, *Basic biomechanics of the musculoskeletal system*. 2001: Lippincott Williams & Wilkins.
28. Wolff, J., *The law of bone remodelling*. 2012: Springer Science & Business Media.
29. Currey, J.D., *Tensile yield in compact bone is determined by strain, post-yield behaviour by mineral content.* Journal of biomechanics, 2004. **37**(4): p. 549-556.
30. Schlecht, S.H., E.M. Bigelow, and K.J. Jepsen, *Mapping the natural variation in whole bone stiffness and strength across skeletal sites.* Bone, 2014. **67**: p. 15-22.
31. Currey, J.D. and R.M. Alexander, *The thickness of the walls of tubular bones.* Journal of Zoology, 1985. **206**(4): p. 453-468.
32. Turner, C.H., *Bone strength: current concepts.* Annals of the New York Academy of Sciences, 2006. **1068**(1): p. 429-446.
33. Voide, R., G.H. van Lenthe, and R. Müller, *Bone morphometry strongly predicts cortical bone stiffness and strength, but not toughness, in inbred mouse models of high and low bone mass.* Journal of Bone and Mineral Research, 2008. **23**(8): p. 1194-1203.
34. Murach, M.M., et al., *Rib geometry explains variation in dynamic structural response: potential implications for frontal impact fracture risk.* Annals of biomedical engineering, 2017. **45**(9): p. 2159-2173.
35. Schlecht, S.H. and K.J. Jepsen, *Functional integration of skeletal traits: an intraskeletal assessment of bone size, mineralization, and volume covariance.* Bone, 2013. **56**(1): p. 127-138.
36. Jepsen, K.J., *Functional interactions among morphologic and tissue quality traits define bone quality.* Clinical Orthopaedics and Related Research®, 2011. **469**(8): p. 2150-2159.
37. Platzer, W., *Color Atlas of Human Anatomy, Vol. 1. Locomotor System. 5. painos*. 2004, Stuttgart: Georg Thieme Verlag.
38. Dalstra, M., R. Huiskes, and L. van Erning, *Development and validation of a three-dimensional finite element model of the pelvic bone.* 1995.
39. Bergmann, G., et al., *Hip contact forces and gait patterns from routine activities.* Journal of biomechanics, 2001. **34**(7): p. 859-871.
40. van Dijke, G.A.H., et al., *A biomechanical model on muscle forces in the transfer of spinal load to the pelvis and legs.* Journal of biomechanics, 1999. **32**(9): p. 927-933.
41. Phillips, A., et al., *Finite element modelling of the pelvis: inclusion of muscular and ligamentous boundary conditions.* Medical engineering & physics, 2007. **29**(7): p. 739-748.
42. Booij, R., et al., *Technological developments of X-ray computed tomography over half a century: User's influence on protocol optimization.* European Journal of Radiology, 2020: p. 109261.
43. Kalender, W.A., *X-ray computed tomography.* Physics in Medicine & Biology, 2006. **51**(13): p. R29.
44. Chapman, T., et al., *Sex determination using the Probabilistic Sex Diagnosis (DSP: Diagnose Sexuelle Probabiliste) tool in a virtual environment.* Forensic science international, 2014. **234**: p. 189. e1-189. e8.
45. Mestekova, S., et al., *A test of the DSP sexing method on CT images from a modern French sample.* Journal of forensic sciences, 2015. **60**(5): p. 1295-1299.

46. Stull, K.E., et al., *Accuracy and reliability of measurements obtained from computed tomography 3D volume rendered images.* Forensic science international, 2014. **238**: p. 133-140.
47. Colman, K.L., et al., *The geometrical precision of virtual bone models derived from clinical computed tomography data for forensic anthropology.* International journal of legal medicine, 2017. **131**(4): p. 1155-1163.
48. Colman, K.L., et al., *Virtual forensic anthropology: the accuracy of osteometric analysis of 3D bone models derived from clinical computed tomography (CT) scans.* Forensic science international, 2019. **304**: p. 109963.
49. Bloem, J.L. and I.I. Reidsma, *Bone and soft tissue tumors of hip and pelvis.* European journal of radiology, 2012. **81**(12): p. 3793-3801.
50. Miles, A. and S. Gheduzzi, *Basic biomechanics and biomaterials.* Surgery (Oxford), 2012. **30**(2): p. 86-91.
51. Caeiro, J., P. González, and D. Guede, *Biomechanics and bone (& II): Trials in different hierarchical levels of bone and alternative tools for the determination of bone strength.* Rev Osteoporos Metab Miner, 2013. **5**(2): p. 99-108.
52. Hart, N.H., et al., *Mechanical basis of bone strength: influence of bone material, bone structure and muscle action.* Journal of musculoskeletal & neuronal interactions, 2017. **17**(3): p. 114.
53. Hartsuijker, C. and J.W. Welleman, *Engineering Mechanics: Volume 2: Stresses, Strains, Displacements*. Vol. 2. 2007: Springer Science & Business Media.
54. Cowin, S.C., *Bone mechanics handbook*. 2001: CRC press.
55. Wu, D., et al., *Young's modulus of trabecular bone at the tissue level: A review.* Acta biomaterialia, 2018. **78**: p. 1-12.
56. Jee, W., *Integrated bone tissue physiology: anatomy and physiology.* Bone mechanics handbook, 2001.
57. Guo, X.E., *Mechanical properties of cortical bone and cancellous bone tissue.* Bone mechanics handbook, 2001. **10**: p. 1-23.
58. Gong, J., J. Arnold, and S. Cohn, *Composition of trabecular and cortical bone.* The Anatomical Record, 1964. **149**(3): p. 325-331.
59. An, Y.H. and R.A. Draughn, *Mechanical testing of bone and the bone-implant interface*. 1999: CRC press.
60. Brekelmans, W., H. Poort, and T. Slooff, *A new method to analyse the mechanical behaviour of skeletal parts.* Acta Orthopaedica Scandinavica, 1972. **43**(5): p. 301-317.
61. Szabó, B. and I. Babuška, *Finite element analysis*. 1991: John Wiley & Sons.
62. Van Staden, R., H. Guan, and Y.-C. Loo, *Application of the finite element method in dental implant research.* Computer methods in biomechanics and biomedical engineering, 2006. **9**(4): p. 257-270.
63. Gao, J., W. Xu, and Z. Ding, *3D finite element mesh generation of complicated tooth model based on CT slices.* Computer methods and programs in biomedicine, 2006. **82**(2): p. 97-105.
64. Auzias, G., et al. *Disco: A coherent diffeomorphic framework for brain registration under exhaustive sulcal constraints*. in *International Conference on Medical Image Computing and Computer-Assisted Intervention*. 2009. Springer.
65. Martin, R.B. and N.A. Sharkey, *Mechanical effects of postmortem changes, preservation, and allograft bone treatments.* Bone Mechanics Handbook, Second Edition, 2001: p. 20-1-20-24.
66. Cammarata, M., et al. *Mechanical behavior of human bones with different saturation levels*. in *Conference: 2nd International Electronic Conference on Materials*. 2016.
67. Helgason, B., et al., *Mathematical relationships between bone density and mechanical properties: a literature review.* Clinical biomechanics, 2008. **23**(2): p. 135-146.
68. Keller, T.S., *Predicting the compressive mechanical behavior of bone.* Journal of biomechanics, 1994. **27**(9): p. 1159-1168.

69. Hodgskinson, R. and J. Currey, *Young's modulus, density and material properties in cancellous bone over a large density range.* Journal of Materials Science: Materials in Medicine, 1992. **3**(5): p. 377-381.
70. Goulet, R.W., et al., *The relationship between the structural and orthogonal compressive properties of trabecular bone.* Journal of biomechanics, 1994. **27**(4): p. 375-389.
71. Morgan, E.F., H.H. Bayraktar, and T.M. Keaveny, *Trabecular bone modulus–density relationships depend on anatomic site.* Journal of biomechanics, 2003. **36**(7): p. 897-904.
72. Lotz, J.C., T.N. Gerhart, and W.C. Hayes, *Mechanical properties of metaphyseal bone in the proximal femur.* Journal of biomechanics, 1991. **24**(5): p. 317-329.
73. Lotz, J.C., T.N. Gerhart, and W.C. Hayes, *Mechanical properties of trabecular bone from the proximal femur: a quantitative CT study.* Journal of computer assisted tomography, 1990. **14**(1): p. 107-114.
74. Li, B. and R.M. Aspden, *Composition and mechanical properties of cancellous bone from the femoral head of patients with osteoporosis or osteoarthritis.* Journal of bone and mineral research, 1997. **12**(4): p. 641-651.
75. Ciarelli, T., et al., *Variations in three-dimensional cancellous bone architecture of the proximal femur in female hip fractures and in controls.* Journal of Bone and Mineral Research, 2000. **15**(1): p. 32-40.
76. Kaneko, T.S., et al., *Mechanical properties, density and quantitative CT scan data of trabecular bone with and without metastases.* Journal of biomechanics, 2004. **37**(4): p. 523-530.
77. Cong, A., J.O. Den Buijs, and D. Dragomir-Daescu, *In situ parameter identification of optimal density–elastic modulus relationships in subject-specific finite element models of the proximal femur.* Medical engineering & physics, 2011. **33**(2): p. 164-173.
78. Den Buijs, J.O. and D. Dragomir-Daescu, *Validated finite element models of the proximal femur using two-dimensional projected geometry and bone density.* Computer methods and programs in biomedicine, 2011. **104**(2): p. 168-174.
79. Eberle, S., M. Göttlinger, and P. Augat, *Individual density–elasticity relationships improve accuracy of subject-specific finite element models of human femurs.* Journal of biomechanics, 2013. **46**(13): p. 2152-2157.
80. Duchemin, L., et al., *Prediction of mechanical properties of cortical bone by quantitative computed tomography.* Medical engineering & physics, 2008. **30**(3): p. 321-328.
81. Snyder, S.M. and E. Schneider, *Estimation of mechanical properties of cortical bone by computed tomography.* Journal of Orthopaedic Research, 1991. **9**(3): p. 422-431.
82. Linde, F., I. Hvid, and F. Madsen, *The effect of specimen geometry on the mechanical behaviour of trabecular bone specimens.* Journal of biomechanics, 1992. **25**(4): p. 359-368.
83. Anderson, M.J., J. Keyak, and H. Skinner, *Compressive mechanical properties of human cancellous bone after gamma irradiation.* JBJS, 1992. **74**(5): p. 747-752.
84. Keyak, J., I. Lee, and H. Skinner, *Correlations between orthogonal mechanical properties and density of trabecular bone: use of different densitometric measures.* Journal of biomedical materials research, 1994. **28**(11): p. 1329-1336.
85. Rho, J.-Y., M. Hobatho, and R. Ashman, *Relations of mechanical properties to density and CT numbers in human bone.* Medical engineering & physics, 1995. **17**(5): p. 347-355.
86. Austman, R., et al., *Development of a customized density—modulus relationship for use in subject-specific finite element models of the ulna.* Proceedings of the Institution of Mechanical Engineers, Part H: Journal of Engineering in Medicine, 2009. **223**(6): p. 787-794.
87. Šmejkal, K., et al., *Impaired healing after surgery for femoral fractures.* Acta chirurgiae orthopaedicae et traumatologiae Cechoslovaca, 2015. **82**(5): p. 358-363.
88. Keaveny, T.M., et al., *Systematic and random errors in compression testing of trabecular bone.* Journal of orthopaedic research, 1997. **15**(1): p. 101-110.
89. Ouyang, J., et al., *Biomechanical characteristics of human trabecular bone.* Clinical Biomechanics, 1997. **12**(7-8): p. 522-524.

90. Kopperdahl, D.L. and T.M. Keaveny, *Yield strain behavior of trabecular bone.* Journal of biomechanics, 1998. **31**(7): p. 601-608.
91. Kopperdahl, D.L., E.F. Morgan, and T.M. Keaveny, *Quantitative computed tomography estimates of the mechanical properties of human vertebral trabecular bone.* Journal of orthopaedic research, 2002. **20**(4): p. 801-805.
92. Dalstra, M., et al., *Mechanical and textural properties of pelvic trabecular bone.* Journal of biomechanics, 1993. **26**(4-5): p. 523-535.
93. Knowles, N.K., et al., *Development of a validated glenoid trabecular density-modulus relationship.* Journal of the mechanical behavior of biomedical materials, 2019. **90**: p. 140-145.
94. Keaveny, T.M., et al., *Theoretical analysis of the experimental artifact in trabecular bone compressive modulus.* Journal of Biomechanics, 1993. **26**(4-5): p. 599-607.
95. Keaveny, T.M., et al., *Differences between the tensile and compressive strengths of bovine tibial trabecular bone depend on modulus.* Journal of biomechanics, 1994. **27**(9): p. 1137-1146.
96. Zhu, M., T. Keller, and D. Spengler, *Effects of specimen load-bearing and free surface layers on the compressive mechanical properties of cellular materials.* Journal of biomechanics, 1994. **27**(1): p. 57-66.
97. Ün, K., G. Bevill, and T.M. Keaveny, *The effects of side-artifacts on the elastic modulus of trabecular bone.* Journal of biomechanics, 2006. **39**(11): p. 1955-1963.
98. Chen, Y., et al., *Micro-CT based finite element models of cancellous bone predict accurately displacement once the boundary condition is well replicated: a validation study.* Journal of the mechanical behavior of biomedical materials, 2017. **65**: p. 644-651.
99. Renders, G., et al., *Mineral heterogeneity affects predictions of intratrabecular stress and strain.* Journal of biomechanics, 2011. **44**(3): p. 402-407.
100. Van Ruijven, L., L. Mulder, and T. Van Eijden, *Variations in mineralization affect the stress and strain distributions in cortical and trabecular bone.* Journal of biomechanics, 2007. **40**(6): p. 1211-1218.
101. Feldkamp, L.A., et al., *The direct examination of three-dimensional bone architecture in vitro by computed tomography.* Journal of bone and mineral research, 1989. **4**(1): p. 3-11.
102. Dahan, G., et al., *Verified and validated finite element analyses of humeri.* Journal of Biomechanics, 2016. **49**(7): p. 1094-1102.
103. Majumdar, S., et al., *High-resolution magnetic resonance imaging: three-dimensional trabecular bone architecture and biomechanical properties.* Bone, 1998. **22**(5): p. 445-454.
104. Keyak, J.H., et al., *Prediction of femoral fracture load using automated finite element modeling.* Journal of biomechanics, 1997. **31**(2): p. 125-133.
105. Dahan, G., et al., *Finite element analyses for predicting anatomical neck fractures in the proximal humerus.* Clinical Biomechanics, 2019. **68**: p. 114-121.
106. Yosibash, Z., et al., *Predicting the stiffness and strength of human femurs with real metastatic tumors.* Bone, 2014. **69**: p. 180-190.
107. Pauchard, Y., et al., *Interactive graph-cut segmentation for fast creation of finite element models from clinical ct data for hip fracture prediction.* Comput Methods Biomech Biomed Engin, 2016. **19**(16): p. 1693-1703.
108. Helgason, B., et al., *The influence of the modulus–density relationship and the material mapping method on the simulated mechanical response of the proximal femur in side-ways fall loading configuration.* Medical engineering & physics, 2016. **38**(7): p. 679-689.
109. Avants, B.B., et al., *A reproducible evaluation of ANTs similarity metric performance in brain image registration.* Neuroimage, 2011. **54**(3): p. 2033-44.
110. Colman, K.L., et al., *The accuracy of 3D virtual bone models of the pelvis for morphological sex estimation.* International journal of legal medicine, 2019. **133**(6): p. 1853-1860.

111. Franklin, D., et al., *Concordance of traditional osteometric and volume-rendered MSCT interlandmark cranial measurements.* International journal of legal medicine, 2013. **127**(2): p. 505-520.
112. Aldridge, K., et al., *Precision and error of three-dimensional phenotypic measures acquired from 3dMD photogrammetric images.* American journal of medical genetics Part A, 2005. **138**(3): p. 247-253.
113. Klales, A.R., S.D. Ousley, and J.M. Vollner, *A revised method of sexing the human innominate using Phenice's nonmetric traits and statistical methods.* American journal of physical anthropology, 2012. **149**(1): p. 104-114.
114. Walker, P.L., *Greater sciatic notch morphology: sex, age, and population differences.* American Journal of Physical Anthropology: The Official Publication of the American Association of Physical Anthropologists, 2005. **127**(4): p. 385-391.
115. Tustison, N.J., et al., *Large-scale evaluation of ANTs and FreeSurfer cortical thickness measurements.* Neuroimage, 2014. **99**: p. 166-179.
116. Dogdas, B., et al. *Characterization of bone abnormalities from micro-CT images for evaluating drug toxicity in developmental and reproductive toxicology (DART) studies*. in *2015 IEEE 12th International Symposium on Biomedical Imaging (ISBI)*. 2015. IEEE.
117. Ramme, A.J., et al., *Automated bone segmentation and surface evaluation of a small animal model of post-traumatic osteoarthritis.* Annals of biomedical engineering, 2017. **45**(5): p. 1227-1235.
118. Ahrens, J., B. Geveci, and C. Law, *Paraview: An end-user tool for large data visualization.* The visualization handbook, 2005. **717**(8).
119. Brůžek, J., et al., *Validation and reliability of the sex estimation of the human os coxae using freely available DSP2 software for bioarchaeology and forensic anthropology.* American journal of physical anthropology, 2017. **164**(2): p. 440-449.
120. Quatrehomme, G., et al., *Sex determination using the DSP (probabilistic sex diagnosis) method on the coxal bone: Efficiency of method according to number of available variables.* Forensic science international, 2017. **272**: p. 190-193.
121. Ulijaszek, S.J. and D.A. Kerr, *Anthropometric measurement error and the assessment of nutritional status.* British Journal of Nutrition, 1999. **82**(3): p. 165-177.
122. Goto, R. and N.M.-T. CG, *Precision of measurement as a component of human variation.* Journal of physiological anthropology, 2007. **26**(2): p. 253-256.
123. Carsley, S., et al., *Reliability of routinely collected anthropometric measurements in primary care.* BMC medical research methodology, 2019. **19**(1): p. 1-8.
124. Pedregosa, F., et al., *Scikit-learn: Machine learning in Python.* the Journal of machine Learning research, 2011. **12**: p. 2825-2830.
125. Busse, B., et al., *Increased calcium content and inhomogeneity of mineralization render bone toughness in osteoporosis: mineralization, morphology and biomechanics of human single trabeculae.* Bone, 2009. **45**(6): p. 1034-1043.
126. Tai, K., et al., *Nanoscale heterogeneity promotes energy dissipation in bone.* Nature materials, 2007. **6**(6): p. 454-462.
127. Davies, B., et al., *Hypothesis: Bones toughness arises from the suppression of elastic waves.* Scientific reports, 2014. **4**(1): p. 1-6.
128. Torres, A.M., et al., *Material heterogeneity in cancellous bone promotes deformation recovery after mechanical failure.* Proceedings of the National Academy of Sciences, 2016. **113**(11): p. 2892-2897.
129. Ruffoni, D., et al., *The bone mineralization density distribution as a fingerprint of the mineralization process.* Bone, 2007. **40**(5): p. 1308-1319.
130. Falcinelli, C., et al., *Multiple loading conditions analysis can improve the association between finite element bone strength estimates and proximal femur fractures: a preliminary study in elderly women.* Bone, 2014. **67**: p. 71-80.

131. Orwoll, E.S., et al., *Finite element analysis of the proximal femur and hip fracture risk in older men.* Journal of bone and mineral research, 2009. **24**(3): p. 475-483.
132. Dong, X.N., et al., *Random field assessment of nanoscopic inhomogeneity of bone.* Bone, 2010. **47**(6): p. 1080-1084.
133. Dong, X.N., et al., *Random field assessment of inhomogeneous bone mineral density from DXA scans can enhance the differentiation between postmenopausal women with and without hip fractures.* Journal of biomechanics, 2015. **48**(6): p. 1043-1051.
134. Dong, X.N., et al., *Stochastic predictors from the DXA scans of human lumbar vertebrae are correlated with the microarchitecture parameters of trabecular bone.* Journal of biomechanics, 2015. **48**(12): p. 2968-2975.
135. Maquer, G., et al., *The initial slope of the variogram, foundation of the trabecular bone score, is not or is poorly associated with vertebral strength.* Journal of bone and mineral research, 2016. **31**(2): p. 341-346.
136. Michalski, A.S., et al., *CT-based internal density calibration for opportunistic skeletal assessment using abdominal CT scans.* Medical Engineering & Physics, 2020. **78**: p. 55-63.
137. Schroeder, W. and B. Ken Martin, *VTK Toolkit 3rd Edition An Object-Oriented Approach To 3D Graphics*. 2003, Kitware.
138. Hu, Y., et al., *Tetrahedral meshing in the wild.* ACM Trans. Graph., 2018. **37**(4): p. 60:1-60:14.
139. Barak, M.M. and M.A. Black, *A novel use of 3D printing model demonstrates the effects of deteriorated trabecular bone structure on bone stiffness and strength.* Journal of the mechanical behavior of biomedical materials, 2018. **78**: p. 455-464.
140. Collins, C.J., et al., *Design of a surrogate for evaluation of methods to predict bone bending stiffness.* Journal of the mechanical behavior of biomedical materials, 2018. **88**: p. 346-351.
141. Liu, X.S., et al., *Bone density, geometry, microstructure, and stiffness: Relationships between peripheral and central skeletal sites assessed by DXA, HR-pQCT, and cQCT in premenopausal women.* Journal of bone and mineral research, 2010. **25**(10): p. 2229-2238.
142. Knowles, N.K., et al., *Morphological and Apparent-Level Stiffness Variations Between Normal and Osteoarthritic Bone in the Humeral Head.* Journal of Orthopaedic Research®, 2020. **38**(3): p. 503-509.
143. Reuter, M., et al., *Laplace–Beltrami eigenvalues and topological features of eigenfunctions for statistical shape analysis.* Computer-Aided Design, 2009. **41**(10): p. 739-755.
144. Chaudhari, A.J., et al., *Global point signature for shape analysis of carpal bones.* Physics in Medicine & Biology, 2014. **59**(4): p. 961.
145. Taylor, W., et al., *Determination of orthotropic bone elastic constants using FEA and modal analysis.* Journal of biomechanics, 2002. **35**(6): p. 767-773.
146. Watson, P.J., et al., *The effect of boundary constraints on finite element modelling of the human pelvis.* Medical engineering & physics, 2017. **43**: p. 48-57.
147. Logg, A., K.-A. Mardal, and G. Wells, *Automated solution of differential equations by the finite element method: The FEniCS book*. Vol. 84. 2012: Springer Science & Business Media.
148. Hernandez, V., J.E. Roman, and V. Vidal, *SLEPc: A scalable and flexible toolkit for the solution of eigenvalue problems.* ACM Transactions on Mathematical Software (TOMS), 2005. **31**(3): p. 351-362.
149. Weinberg, S.M., et al., *Intraobserver error associated with measurements of the hand.* American Journal of Human Biology: The Official Journal of the Human Biology Association, 2005. **17**(3): p. 368-371.
150. Kranioti, E.F., A. Bonicelli, and J.G. García-Donas, *Bone-mineral density: clinical significance, methods of quantification and forensic applications.* Research and Reports in Forensic Medical Science, 2019(9): p. 9-21.
151. Vacca, E. and G. Di Vella, *Metric characterization of the human coxal bone on a recent Italian sample and multivariate discriminant analysis to determine sex.* Forensic science international, 2012. **222**(1-3): p. 401. e1-401. e9.

152. Málková, M., et al., *An intuitive polygon morphing.* The Visual Computer, 2010. **26**(3): p. 205-215.
153. Savonnet, L., et al., *Pelvis and femur shape prediction using principal component analysis for body model on seat comfort assessment. Impact on the prediction of the used palpable anatomical landmarks as predictors.* PloS one, 2019. **14**(8): p. e0221201.
154. Kai, S., et al., *Automatic construction of an anatomical coordinate system for three-dimensional bone models of the lower extremities–pelvis, femur, and tibia.* Journal of biomechanics, 2014. **47**(5): p. 1229-1233.
155. Schumann, S., L.-P. Nolte, and G. Zheng, *Comparison of partial least squares regression and principal component regression for pelvic shape prediction.* Journal of biomechanics, 2013. **46**(1): p. 197-199.
156. Demontiero, O., C. Vidal, and G. Duque, *Aging and bone loss: new insights for the clinician.* Therapeutic advances in musculoskeletal disease, 2012. **4**(2): p. 61-76.
157. Khosla, S. and B.L. Riggs, *Pathophysiology of age-related bone loss and osteoporosis.* Endocrinology and Metabolism Clinics, 2005. **34**(4): p. 1015-1030.
158. Riggs, B.L., et al., *Population-based study of age and sex differences in bone volumetric density, size, geometry, and structure at different skeletal sites.* Journal of Bone and Mineral Research, 2004. **19**(12): p. 1945-1954.
159. Ott, S.M., *Cortical or trabecular bone: what's the difference?* American journal of nephrology, 2018. **47**(6): p. 373-376.
160. Wang, X., *Cortical bone mechanics and composition: effects of age and gender*, in *Skeletal Aging and Osteoporosis*. 2012, Springer. p. 53-85.
161. Seeman, E., *Structural basis of growth-related gain and age-related loss of bone strength proceedings of a satellite symposium held on the occasion of the EULAR Congress, Paris, France, June 13, 2008.* Rheumatology, 2008. **47**(suppl_4): p. iv2-iv8.
162. Jepsen, K.J. and N. Andarawis-Puri, *The amount of periosteal apposition required to maintain bone strength during aging depends on adult bone morphology and tissue-modulus degradation rate.* Journal of Bone and Mineral Research, 2012. **27**(9): p. 1916-1926.
163. Nicks, K.M., et al., *Relationship of age to bone microstructure independent of areal bone mineral density.* Journal of Bone and Mineral Research, 2012. **27**(3): p. 637-644.
164. Aaron, J.E., N.B. Makins, and K. Sagreiya, *The Microanatomy of Trabecular Bone Loss in Normal Aging Men and Women.* Clinical Orthopaedics and Related Research, 1987(215): p. 260-271.
165. Ding, M., et al., *Age-related variations in the microstructure of human tibial cancellous bone.* Journal of orthopaedic research, 2002. **20**(3): p. 615-621.
166. Chen, H., et al., *Age-related changes in trabecular and cortical bone microstructure.* International journal of endocrinology, 2013. **2013**.
167. Koehne, T., et al., *Trends in trabecular architecture and bone mineral density distribution in 152 individuals aged 30–90 years.* Bone, 2014. **66**: p. 31-38.
168. Wahyuni, E. and T.J.T. Ji, *Relationship between static stiffness and modal stiffness of structures.* IPTEK the Journal for Technology and Science, 2010. **21**(2).
169. Henyš, P. and L. Čapek, *Material model of pelvic bone based on modal analysis: a study on the composite bone.* Biomechanics and modeling in mechanobiology, 2017. **16**(1): p. 363-373.
170. Neugebauer, R., et al., *Experimental modal analysis on fresh-frozen human hemipelvic bones employing a 3D laser vibrometer for the purpose of modal parameter identification.* Journal of biomechanics, 2011. **44**(8): p. 1610-1613.
171. Conza, N., D. Rixen, and S. Plomp, *Vibration testing of a fresh-frozen human pelvis: the role of the pelvic ligaments.* Journal of biomechanics, 2007. **40**(7): p. 1599-1605.
172. Scholz, R., et al., *Validation of density–elasticity relationships for finite element modeling of human pelvic bone by modal analysis.* Journal of biomechanics, 2013. **46**(15): p. 2667-2673.

173. Karakas, H.M., A. Harma, and B. Alicioglu, *The subpubic angle in sex determination: anthropometric measurements and analyses on Anatolian Caucasians using multidetector computed tomography datasets.* Journal of Forensic and Legal Medicine, 2013. **20**(8): p. 1004-1009.
174. Kranioti, E.F., et al., *Sex estimation of os coxae using DSP2 software: A validation study of a Greek sample.* Forensic science international, 2019. **297**: p. 371. e1-371. e6.
175. Dougherty, G. and D. Newman, *Measurement of thickness and density of thin structures by computed tomography: a simulation study.* Medical physics, 1999. **26**(7): p. 1341-1348.
176. Prevrhal, S., et al., *Accuracy of CT-based thickness measurement of thin structures: modeling of limited spatial resolution in all three dimensions.* Medical physics, 2003. **30**(1): p. 1-8.
177. Hernigou, J., et al., *Anatomy of the ilium for bone marrow aspiration: map of sectors and implication for safe trocar placement.* International orthopaedics, 2014. **38**(12): p. 2585-2590.
178. Treece, G.M. and A.H. Gee, *Independent measurement of femoral cortical thickness and cortical bone density using clinical CT.* Medical image analysis, 2015. **20**(1): p. 249-264.
179. Lee, D.C., et al., *Phantomless calibration of CT scans for measurement of BMD and bone strength—inter-operator reanalysis precision.* Bone, 2017. **103**: p. 325-333.
180. Winsor, C., et al., *Evaluation of patient tissue selection methods for deriving equivalent density calibration for femoral bone quantitative CT analyses.* Bone, 2021. **143**.
181. Sangeux, M., *Biomechanics of the hip during gait*, in *The Pediatric and Adolescent Hip*. 2019, Springer. p. 53-71.
182. Maas, S.A., et al., *FEBio: finite elements for biomechanics.* Journal of biomechanical engineering, 2012. **134**(1).
183. Giarmatzis, G., et al., *Loading of hip measured by hip contact forces at different speeds of walking and running.* Journal of Bone and Mineral Research, 2015. **30**(8): p. 1431-1440.